University of Genoa

School of Mathematical, Physical and Natural Sciences

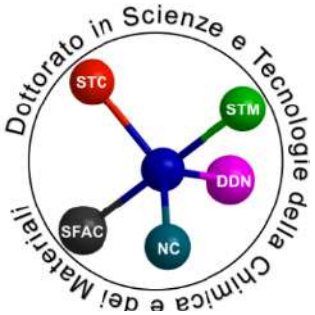

Doctor of Philosophy in Sciences and Technologies of Chemistry and Materials

Department of Chemistry and Industrial Chemistry

Electrospun Mixed Ionic-Electronic Conductors for Energy Applications

By

Caterina Sanna

Supervisor: Prof. Paola Costamagna

Co-supervisor: Prof. Alberto Servida

March 2023

Dedicata alla mia famiglia, soprattutto alla mia sorellina Margherita

Contents

Abstract

Intermediate temperature-solid oxide fuel cells (IT-SOFCs) are under development for operation in the temperature range of 600-800°C. This intermediate temperature negatively affects the electrode kinetics and thus the cell performance, making it essential for the improvement of the electrode materials and architectures. For this reason, high-performance electrolytes and electrodes are currently under development, often based on mixed ionic electronic conductors (MIECs). Due to their ability to carry simultaneously both electrons and oxygen ions, the application of MIECs as IT-SOFC electrodes is expected to extend the electrochemical reaction well inside the electrode thickness. On the other hand, one-dimensional materials like nanotubes, nanorods, and nanofibers have gained significance due to their high surface area and mechanical properties. Electrospinning is the method of choice for nanofiber preparation since, compared to other available methods, is cost-effective, simple, and reproducible.

In this work, the manufacture and characterization of nanofiber-based electrodes are investigated. The attention is focused on the preparation and characterization of cathodes for IT-SOFC application, but anodes are investigated as well. The electrode manufacturing process employed is the electrospinning technique. Several electrospun architectures are analyzed, such as co-electrospun and core-shell nanofibers electrodes. Several materials are investigated, the state-of-the-art $La_{0.6}Sr_{0.4}MnO_3$ (LSM) and $La_{0.6}Sr_{0.4}Co_{0.2}Fe_{0.8}O_{3-\delta}$ (LSCF), followed by Co-free perovskites such as $La_{0.6}Sr_{0.4}Cu_{0.1}Mn_{0.9}O_{3-\delta}$ (LSCuM_1), $La_{0.6}Sr_{0.4}Cu_{0.2}Mn_{0.8}O_{3-\delta}$ (LSCuM_2) and $La_{0.6}Sr_{0.4}Cu_{0.2}Fe_{0.8}O_{3-\delta}$ (LSCuF). The composite architectures prepared with $Ce_{0.9}Gd_{0.1}O_{1.95}$ (GDC) are manufactured as well. All the nanofibers are morphologically characterized through SEM and XRD. The electrochemical characterization is carried out through electrochemical impedance spectroscopy (EIS) measurements. The acquired experimental data are fitted through equivalent circuit (EC) modeling, which provides an interpretation of the electrochemical phenomena. Finally, the obtained results are critically compared with literature values.

1. Introduction

Solid Oxide Fuel Cells (SOFCs) are energy conversion systems that are characterized by high efficiency, low greenhouse gas emissions, and fuel flexibility. Thus, during the last decades, these devices have been widely investigated [1]. The SOFC directly converts the chemical energy of fuels into electrical energy through several electrochemical reactions. Fig. 1 shows the schematic representation of a SOFC, which consists in two porous electrodes, where the electrochemical reactions take place, separated by a dense electrolyte. The cathode site is generally fed with air or pure oxygen, leading to a reduction reaction that decomposes the oxygen molecules allowing the formation of oxygen ions (ORR, oxygen reduction reaction):

$$\frac{1}{2}O_2 + 2e^- \rightleftarrows O^{--} \tag{1}$$

Then the oxygen ions migrate through the dense electrolyte to the anode site, which is generally fed with hydrogen or light hydrocarbons. These fuels are oxidized leading to the release of reaction products, which in the case of hydrogen is only water:

$$H_2 + O^{--} \rightleftarrows H_2O + 2e^- \tag{2}$$

This reaction is called the hydrogen oxidation reaction (HOR), and the electrode is called the anode. The electrons produced during the reduction/oxidation reactions flow in an external electrical circuit, allowing the production of electrical energy. Considering hydrogen as an anode fuel, the overall reaction which takes place in the SOFC coincides with the combustion of hydrogen:

$$H_2 + \frac{1}{2}O_2 \rightleftarrows H_2O \tag{3}$$

The direct transformation of a portion of the overall reaction ΔG in electrical work, permit avoiding any thermodynamic cycle, and all the efficiency limitation related to the Carnot efficiency. For this reason, is possible to achieve an energy conversion with high efficiency

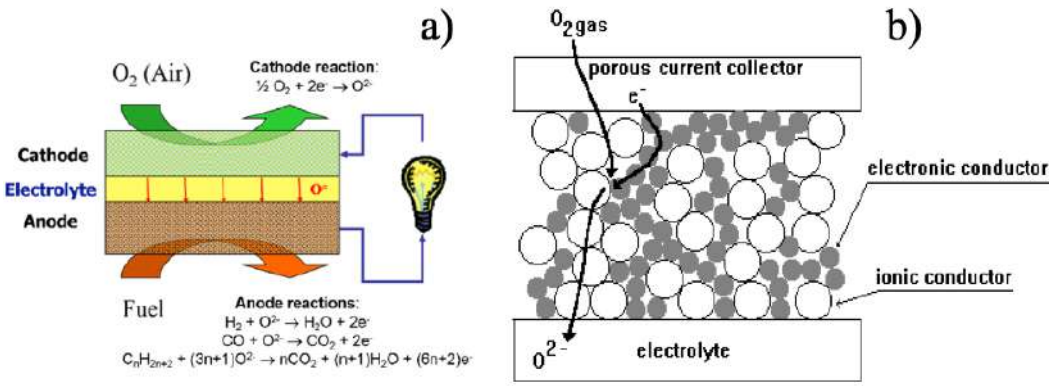

Fig. 1: SOFC (a) scheme of working principle [2]; (b) scheme of composite cathode [3].

One of the most important features of SOFCs is the presence of all solid-state components, both electrodes, and electrolyte, which allows the overcoming of the problem related to the liquid electrolytes such as corrosion and flooding. The electrolyte is required to be dense since it has to avoid any contact between the anode and cathode gasses. Indeed, any leakage of gas would result in a combustion reaction which may lead to safety issues. The state-of-the-art material for the SOFC electrolyte is the yttria-stabilized zirconia (YSZ, i.e. $(ZrO_2)_{1-x}(Y_2O_3)_x$, x=0.03-0.1). The YSZ follows the fluorite crystal structure, which is schematically reported in Fig. 2 (a). The high ion conduction properties of YSZ are given by the introduction of some Yttrium atoms, which has a lower valence compared to Zircon, inside the ZrO_2 fluorite. This substitution increases the number of oxygen vacancies which at high operating temperatures leads to a high ionic conductivity [4]. However, in order to achieve an ionic conductivity of 0.1 Scm^{-1} the operative temperature needs to be around 950°C-1000°C. Due to this electrolyte requirement, the operating temperature of the traditional SOFCs (also called High-Temperature SOFCs, HT-SOFCs) is in the temperature range between 900°C-1100°C. The high temperature required for the correct SOFC operation, unfortunately, leads to several problems, such as slow start-up, high components degradation, and sealings failure. To overcome this problem, several materials are investigated, finding the Ceria-based electrolyte a good candidate for intermediate temperature operations. In particular, gadolinium doped ceria (GDC, i.e. $Ce_{1-x}Gd_xO_{1-\delta}$) is widely employed in the temperature range between 500°C and 800°C, indeed the $Ce_{0.9}Gd_{0.1}O_{1.95}$ fluorite is able to achieve ionic conduction of 0.1 Scm^{-1} at around 880°C [5]. Thus, intermediate temperature solid oxide fuel cells (IT-SOFC) gained great attention for operation between 600°C and 800°C. Anyway, decreasing the operating temperature leads to a decrease in the cathode and anode electrochemical reaction kinetics, and therefore the overall electrochemical performance. For this reason, both electrode materials and electrode architectures are widely investigated to improve their electrochemical performances in the intermediate temperature range. Advanced materials and nanosized architectures are analyzed to find solutions able to provide high catalytic activity, a high level of conductivity, and a satisfactory porosity, to permit gas diffusion. Furthermore, intensive studies are carried out to improve the extension of the specific region in which the electrochemical reaction takes place, which is called the three-phase-boundary (TPB). The TPB is a region in which the gas phase, the electronic conductor, and the ionic conductor meet each other and represent the active reaction sites of the electrode. Thus, electrodes that contain both an electronic conductor material and an ionic conductor material, which normally has the same composition as the electrolyte one, are intensively investigated. This electrode architecture is called composite and nowadays is widely employed. Lastly, One-dimensional (1D) nanomaterials, like nanofibers (NFs), nanotubes (NTs), nanowires (NWs), and nanorods (NRs) are intensively studied as promising

electrode architectures with a high void degree, high internal surface, and potentially high TPB and ionic and electronic conductivity. The key electrode is the cathode since the ORR gives the main contribution to the SOFC internal energy losses.

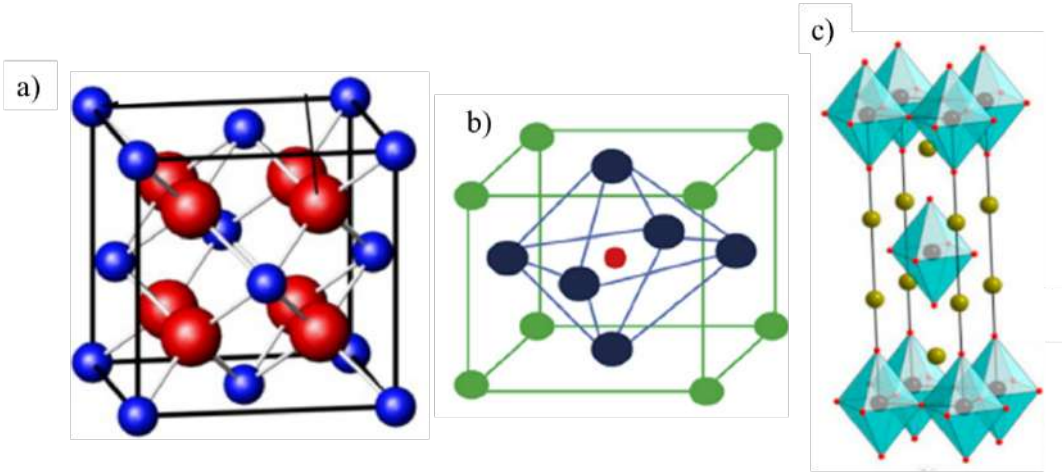

Fig. 2: Schematic structure of (a) fluorite; (b) cubic perovskite; and (c) Ruddlesden-Popper.

1.1 State-of-the-art electrode materials for application in SOFCs

The investigation of innovative geometrical features for enhancing the extension of the TPB inside the electrode is an important improvement for the electrochemical performance. On the other hand, it is also important the research new materials with high catalytic activity. Metal oxides such as perovskite have been intensively investigated in the last decades as promising materials for application as cathodes in SOFC. Thus, below, an overview of the state-of-the-art materials for cathode application in SOFC is carried out, with a short outline of anodes.

1.1.1 Cathode materials

During the last decades, the intensive research work carried out to improve the electrocatalytic performance of electrodes for application in IT-SOFC, lead to the investigation of several metal oxides. Among all, the perovskite oxides have raised much attention due to the interesting features related to ionic and electronic conductivity. The perovskite crystal structure is arranged following the general formula ABO_3, which is reported in Fig. 2. Anyway, thanks to their structure versatility, it is possible to perform substitution both in the A and B sites, affecting the oxygen stoichiometry, influencing the oxygen ion transport and oxygen surface exchange kinetics, as well as the electronic conductivity [6,7].

The state-of-the-art material for HT-SOFC is the $La_{1-x}Sr_xMnO_3$, which is an example of A-doped perovskite (A-doped $LaMnO_3$). The arrangement of the crystal structure depends on the amount of strontium in the perovskite: rhombohedral for $0 < x < 0.5$, tetragonal for $x = 0.5$, and cubic for $x >$

0.7. The substitution of some La^{3+} ions with some Sr^{2+} ions enhances both ionic and electronic conductivity. Indeed, since the Sr has a lower valence compared to La, an electric hole is formed at the B-site in order to maintain the electro-neutrality, leading to the oxidation of an Mn ion:

$$LaMnO_3 \xrightarrow{xSrO} La_{1-x}^{3+} Sr_x^{2+} Mn_{1-x}^{3+} Mn_x^{4+} \quad (4)$$

Thanks to the Sr doping the electrical conductivity of $LaMnO_3$ increases from 83 Scm^{-1} at 800°C to 320 Scm^{-1} at 800°C for the $La_{0.6}Sr_{0.4}MnO_3$ [8].

As far as the IT-SOFCs are concerned, the lanthanum strontium cobalt ferrite $La_{1-x}Sr_xCo_yFe_{1-y}O_{3-\delta}$ is considered the state-of-the-art material for cathode applications. It belongs to the ABO_3 perovskite family, but compared to the $La_{1-x}Sr_xMnO_3$, it is doped both in the A-site and in the B-site, replacing some Fe atoms with Co ones. For this reason, the LSCF achieves a high electronic conductivity and a modest ionic conductivity. This material class is called mixed ionic and electronic conductors (MIEC). The double conductivity is achieved due to the charge compensation, which occurs by the creation of both ionic and electronic defects, caused by the substitution of La^{+3} with Sr^{+2}. It is a combination of the valence change of the iron ions, as described in (5), and the formation of doubly ionized oxygen vacancies, as described in (6):

$$2SrO + 2La^{3+} + \frac{1}{2}O_2 + 2Fe^{3+} \xrightarrow{La(Fe,Co)O_3} La_2O_{3+} + 2Sr^{2+} + 2Fe^{4+} \quad (5)$$

$$2SrO + 2La^{3+} + O^{2-} \xrightarrow{La(Fe,Co)O_3} La_2O_{3+} + 2Sr^{2+} + V_O^{\bullet\bullet} \quad (6)$$

Where $V_O^{\bullet\bullet}$ represents the oxygen vacancy, following the Kröger-Vink notation. Furthermore, the Co ions have a smaller binding energy for oxygen compared to the Fe ions, which increases the electronic conductivity [18]. The amount of copper in the perovskite represents an important parameter since it strongly affects the electronic conductivity σ_e. For example, in the $La_{0.6}Sr_{0.4}Co_{0.8}Fe_{0.2}O_{3-\delta}$ the σ_e is 1000 S cm^{-1} at 800°C, whereas for $La_{0.6}Sr_{0.4}Co_{0.2}Fe_{0.8}O_{3-\delta}$ the σ_e is 280 S cm^{-1} at the same operating temperature. The ionic conductivity σ_i is affected by the Co amount as well: for $La_{0.6}Sr_{0.4}Co_{0.8}Fe_{0.2}O_{3-\delta}$ the σ_i is $2*10^{-2}$ S cm^{-1} at 800 °C while for $La_{0.6}Sr_{0.4}Co_{0.2}Fe_{0.8}O_{3-\delta}$ the σ_i is $1.2*10^{-2}$ S cm^{-1} in the same conditions. Anyway, high concentrations of Co in the LSCF lattice are not recommended as well. Indeed, it is reported in the literature that cobalt may lead to segregation, with consequent loss of conductivity and formation of Co_3O_4 [2].

In recent years, new materials called the Ruddlesden-Popper (RP) metal oxides are investigated for application in IT-SOFC. The RP crystal structure follows the general formula $A_{n+1}B_nO_3$, as reported in Fig. *2* (c), and they are characterized by a large oxygen-ion conductivity, coupled with good electronic conductivity. The structure of the RP oxides consists in n layers of perovskite which are stacked between an AO rock salt along the crystallographic c-axis. When n is equal to 1, the crystal

structure follows the formula A_2BO_4 and so a two-dimensional layered perovskite structure [9]. One example of RP metal oxides employed in IT-SOFC application is the La2NiO4, which has an electronic conductivity of 280 S cm^{-1} at 800°C, and an oxygen ion conductivity of 0.007 S cm^{-1} at 600 °C, better than that of $La_{0.6}Sr_{0.4}Co_{0.2}Fe_{0.8}O_{3-\delta}$ (0.003 S cm^{-1} at 600°C) [10].

1.1.2 Anode materials

As far as the anode is concerned, the state-of-the-art electrode is a composite structure, which is generally a cermet, formed by a mixture of electronic and ionic conductors. Generally, the material chosen for the ionic conduction is the same employed for the electrolyte, while the electronic conductors are chosen between several metal catalysts such as Ni, Co, Fe, Pt, Mn, and Ru [11]. Among all the electrocatalysts, Nickel is one of the most used for the hydrogen evolution reaction due to its high electrochemical activity and cheaper price compared to Cobalt and the other noble metals. Furthermore, Nickel is the state-of-the-art catalyst for the methane steam reforming reaction allowing a more flexible choice of feedstock. The hydrogen fed to the anode compartment is often produced from natural gas through the SMR reaction, then it can contain small quantities of unreacted methane. In this case, the presence of Ni in the anode catalyst is beneficial since it provides in situ conversion of this residual methane into hydrogen. The electronic conductivity of Ni is $138*10^4$ S cm^{-1} at 25°C, and $12*10^4$ S cm^{-1} at 1000 °C. Despite the advantages of Nickel, there are several drawbacks as well. Firstly, the melting temperature of Ni is quite low compared to other metals (1453 °C) reason why the use of this metal at high temperatures may lead to the formation of agglomeration and evaporation, and thus to a loss of electrode porosity. Furthermore, the coefficient of thermal expansion of Ni is different compared to the electrolyte values, causing a detachment and delamination during the change of operating temperatures. These problems related to the use of pure Ni as an anode are overcome by the employment of cermet composite electrodes, formed by mixing Ni and electrolyte powders. The cermet electrodes, as already discussed previously, allow an extension of the TPB improving the electrochemical performance. Thus, the state-of-the-art HT-SOFC anode is the Ni/YSZ cermet [4,11,12]. However even the cermet electrodes at intermediate temperatures lead to several agglomeration and detaching problems, thus the perovskite materials are intensively studied not only as cathodes but also for the anode side. Among the perovskites, La-substituted $SrTiO_3$ and Y-substituted $SrTiO_3$ show satisfactory electrical conductivity in reducing atmosphere and good dimensional and chemical stability upon redox cycling. However, the electrocatalytic performances of these materials are quite poor, thus the $SrTiO_3$ B-site is often doped as well, inserting some Mn or Ga atoms instead the Ti. The $La_4Sr_8Ti_{11}Mn_{1-x}Ga_xO_{38-\delta}$ perovskite reports electrical conductivity values in the range between 7.9 and 6.8 S cm^{-1} at 900 °C in reducing

conditions [13], whereas the $Y_{0.09}Sr_{0.91}TiO_3$ shows an electrical conductivity of 73.7 S cm^{-1} at 800 °C in forming gas (5 vol.% of hydrogen in argon) [14].

1.2 State-of-the-art SOFC electrodes architectures and manufacturing techniques

In the last decades, the powders-based electrodes turned out to be the state-of-the-art electrode architecture for application in IT-SOFC. Nowadays, innovative manufacturing techniques are investigated in order to obtain one-dimensional (1D) nanomaterials which are expected to significantly improve the electrochemical performance of the electrodes. Among all, the electrospinning technique is widely employed for the nanofibers production in IT-SOFC applications. In this chapter, an overview of the state-of-the-art and electrospun architectures is reported.

1.2.1 Powder electrodes

The developments of the powders preparation processes allowed the achievement of nanosized powders, with a highly active surface for electrochemical reactions in order to improve the TPB. Among all the manufacturing processes, the citrate route is widely used for the preparation of IT-SOFC electrodes. Indeed, citric acid can easily complex the number of metal ions, we have developed a new technique involving the pyrolytic decomposition of metal citrate to prepare superfine metal oxides. The entire procedure involves a liquid-phase reaction, complex formation, spontaneous combustion, and a final decomposition process [15,16].

As reported before, in order to extend the TPB inside the electrode bulk, composite electrodes are prepared as a mixture of ionic and electronic conducting particles. A schematic representation of the composite electrode architecture is reported in Fig. *1* (b), where the particles are schematized as spheres. Since the two materials are randomly mixed to form the electrode, the extension of the TPB occurs only if two requirements are satisfied. Firstly, there should be many contacts point between the electronic and the ionic conductor particles, which represent the electrochemical reaction active sites. Both the electrons and the ions have to reach the reaction active sites; thus, the second requirement consists of the presence of both an ionic and electronic conduction path, which is achieved by the connection between the particles of the same material. Indeed, the particles inside the composite electrode aggregate forming clusters, and the electronic and ionic conduction clusters must form continuous paths connecting the current collector, where the electrons are injected into the electrode, and the electrolyte, where the ions migrate to the other part of the cell. This is a typical percolation problem, and many theoretical and experimental studies have been developed [3,17–19], which demonstrate that for each type of particle (ionic or electronic conductors), there is a threshold,

called percolation threshold, at which cluster connectivity is triggered. Below the percolation threshold, there is no cluster connectivity, and the electrode is non-conductive. On the contrary, above the percolation threshold, clusters are formed, which easily span throughout the entire electrode and make it conductive. Another problem that may affect the conductivity inside the electrode is related to the bottleneck, which is naturally formed in the contact point between the particles of the same material and results in a decrease in conductivity. This issue is studied as well, demonstrating that reducing the particle diameters increases the electrochemical performance of the composite electrodes. Usually, in the composite electrodes represented in Fig. 1-(b), which are obtained by powder pressing, particle dimensions are in the range between 0.1 and 1 μm. The problems related to the percolations and bottlenecks, motivate the interest in nanofibers. Indeed, the electrospinning technique allows the manufacture of nanofibers with a small diameter which results in a highly active surface for the evolution of the electrochemical reactions and consequently the extension of the TPB. Generally, the electrospinning technique is able to manufacture nanofiber with 100 nm of diameter and an active surface of 16.7 m^2/g [20]. Furthermore, the nanofibers naturally form a continuous path without bottlenecks, guaranteeing the flow through the electrode of both electrons and ions. The preparation of nanofiber-based electrodes is investigated in parallel with the mixed ionic and electronic materials (MIEC). Indeed, the employment of a material able to conduct both electrons and ions may extend the TPB in each point of the nanofiber. Lastly, another interesting solution for improving the electrochemical performance of the electrospun nanofibers electrode is the infiltration technique. Indeed, the electrochemical performance of MIEC nanofiber-based electrodes is demonstrated to benefit largely from infiltrations, i.e. deposition of nanosized particles adhering onto the MIEC surface [21]. In Tab. 1 a comparison between the electrochemical performances of $La_{1-x}Sr_xCo_yFe_{1-y}O_{3-\delta}$ of powders and nanofiber-based electrodes is reported.

Composition and morphology	d [nm]	Rp [Ω cm2]	T [°C]	Ref.
$La_{0.8}Sr_{0.2}Co_{0.2}Fe_{0.8}O_{3-\delta}$ granular	800	12.5	650	[22]
$La_{0.6}Sr_{0.4}Co_{0.2}Fe_{0.8}O_{3-\delta}$ granular	800-900	4-10	590	[23]
$La_{0.8}Sr_{0.2}Co_{0.2}Fe_{0.8}O_{3-\delta}$ nanorods	200-300	14.1	650	[24]
$La_{0.8}Sr_{0.2}Co_{0.2}Fe_{0.8}O_{3-\delta}$ nanofibers	100	2.3	650	[25]
$La_{0.8}Sr_{0.2}Co_{0.2}Fe_{0.8}O_{3-\delta}$ nanotubes	200-300	1.6	650	[21]
$La_{0.6}Sr_{0.4}Co_{0.2}Fe_{0.8}O_{3-\delta}$ nanofibers	250.000	1.0	650	[26]

Tab. 1: Electrochemical performance of $La_{1-x}Sr_xCo_yFe_{1-y}O_{3-\delta}$ powders and nanofiber-based electrodes.

1.2.2 Typical nanofiber-based electrode structures

The electrospinning technique allows the preparation of several nanofiber-based electrode architectures, some of which are reported in Fig. 3. Fig. 3 (a) shows the morphological features of the nanorods structures [27]. As reported in chapter 1.2.1, the nanorods are obtained by disaggregating the heat-treated nanofibers tissue and the length of the final nanorods is generally between 0.5µm and 2µm. In Fig. 3-(b) the SEM image of unbroken nanofibers is reported [28,29]. The unbroken nanofibers have the advantage of creating a continuous path for both electrons and ions, allowing them to easily flow in the whole electrode thickness improving the charge conductivity. The typical diameters for this type of nanofibers are between 100nm and 500nm. Both nanorods and unbroken nanofibers can be used as backbones for the manufacture of a composite electrode through the infiltration technique.

Fig. 3-(c) shows an example of LSCF nanofibers that are infiltrated with GDC nanoparticles [24]. In order to properly perform the electron infiltration, the percolation problem has to be analyzed. Indeed, the amount of particles infiltrated in the electrodes is an important parameter since there is a percolation threshold, above which the infiltrations contribute to the charge transfer process through the electrode bulk, and this is expected to enhance the electrochemical performance.

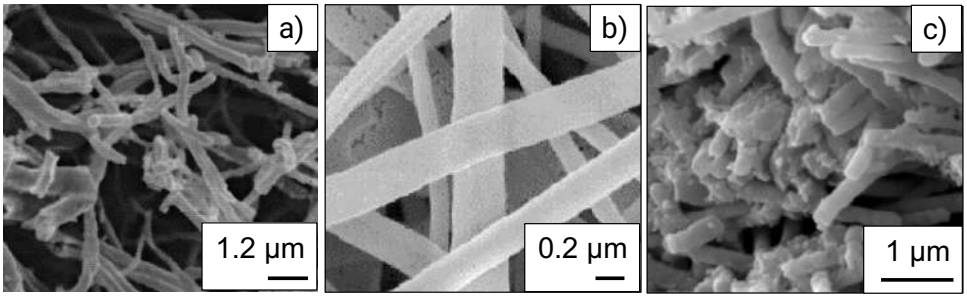

Fig. 3: a) LSCF nanorods [27], b) LSCF unbroken nanofibers [28,29]; c) LSCF nanorods infiltrated with GDC solution [24].

1.3 Experimental methods

In this chapter, the experimental methods used for electrode manufacture and characterization are described in detail.

1.3.1 Electrospinning technique

The electrospinning technique represents one of the main methods for the manufacture of nanofiber structures, which find very interesting applications as electrodes in SOFCs. The electrospun nanofibers are obtained by applying a potential difference between a precursor solution, which is ejected through the solution steel needle, and a metal collector, where the nanofibers tissue is

collected, as described in Fig. 4. Among all the nanofibers manufacturing processes, electrospinning has a low effective cost and allows the reproducibility of the results. Anyway, one of the most interesting features of electrospinning is the possibility of controlling the nanofiber diameter, which is achieved by varying the solution and process parameters. In the next chapters, the electrospinning process will be explained in detail.

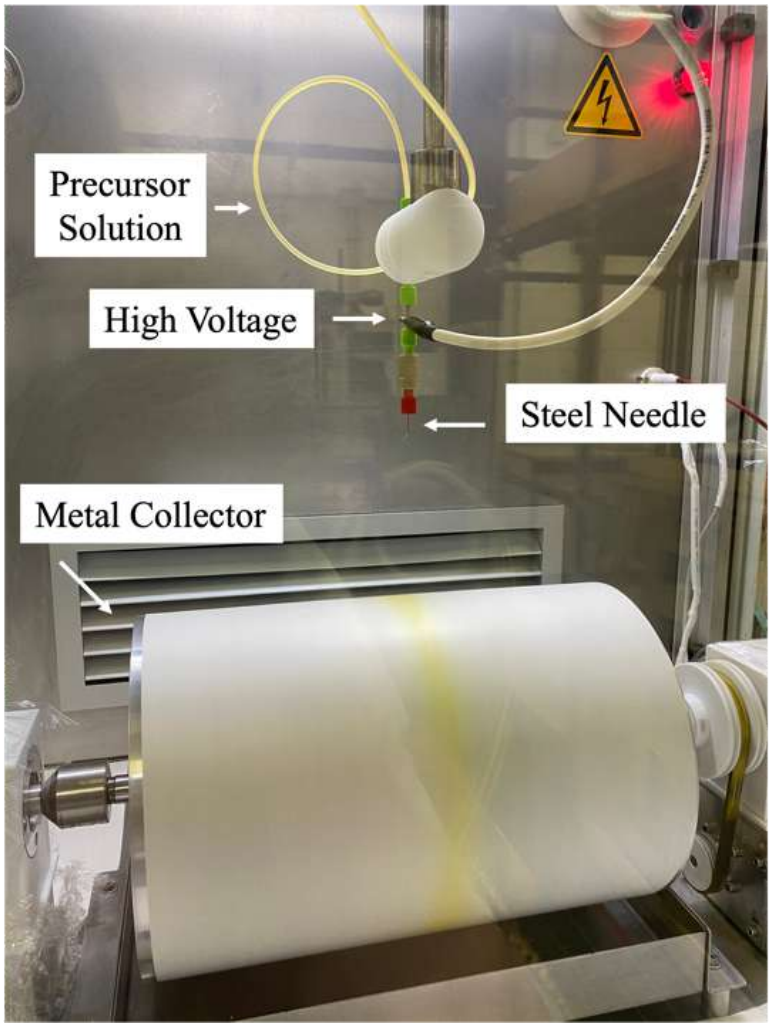

Fig. 4 Example of electrospinning set-up

1.3.1.1 Electrospun electrode preparation

The electrospun nanofibers manufacturing process involves three main steps: the preparation of the precursor solution, the electrospinning process, and the thermal treatment of the raw nanofiber tissue. Tab. 2 schematically summarizes the whole nanofibers manufacturing process. It starts with the preparation of a sol-gel solution which has to contain a solvent or a mixture of solvents, precursor metal salts, and a carrier polymer. The right choice of solvent is essential for the proper evolution of the electrospinning process since the solvent needs to evaporate between the ejection point of the

solution and the collection of the nanofibers. Furthermore, it has to be compatible with the dissolution of the metal salts and the polymer. The solvents which are more used worldwide are water, ethanol, and dimethylformamide (DMF). The metal salts are chosen according to their ability to dissolve in the chosen solvent. Generally, the salts involved in the precursor solution are nitrates, oxides, or hydroxides. Lastly, the carrier polymer needs to be added in order to give shape to the nanofibers. The amount of polymer added to the solution is an important parameter, since it affects the solution viscosity, determining the diameter and morphology of the nanofibers. The polymer generally chosen for SOFC application is polyvinylpyrrolidone (PVP) and polyethylene oxide (PEO).

The precursor solution is then loaded in a syringe equipped with a metal needle, ready for the electrospinning process. The electrospinning process is ruled by several parameters which have to be selected for each precursor solution. Among all, the more important parameters are the applied voltage, solution flow rate, distance between the syringe tip and collector, collector rotation speed, and relative humidity. These parameters are essential for the proper evolution of the electrospinning process and for the final nanofiber morphology. After the electrospinning process, the raw nanofibers have to be heat treated in order to achieve the desired crystal structure. The heating program needs to be controlled in the temperature range in which the polymer degradation takes place. Indeed, if the gas release is too fast it may damage the nanofiber morphology. Thus, it is important to carry out several previous analyses on the polymer, identify the degradation temperature range, and set a slower heating ramp when it takes place. The nanofibers tissue can be attached to the electrolyte as it is, obtaining an electrode made with unbroken and continuous nanofibers, or it can undergo a disaggregation process, generally carried out with the sonicator device, obtaining a nanorod-based electrode. Once the electrodes are attached to the electrolyte, a final heat treatment is carried out in order to improve the adhesion between the two components of the cell. For the characterization of single electrodes, a symmetrical button cell configuration is usually adopted, with identical electrodes on both sides, as represented in

Fig. 5. The size of the symmetrical cells depends on the device used for the measurements, but generally, the diameter range is between 1 cm to 4 cm.

1. Preparation of the electrospinning solution

- Dissolution of metal precursors in the solvent;
- Addition of polymer;
- Stirring

2. Electrospinning process

- Regulation of the electrospinning parameters;

3. Thermal treatment of the raw nanofibers electrodes

- Cutting of the nanofibers tissue in round shape;
- Thermal treatment of the electrodes with a low heating ramp in order to decompose the polymer and achieve the crystallinity

4. Symmetrical cell assembling

- Attachment of the electrodes on both sides of electrolytes;
- Final thermal treatment of the symmetrical cells.

Tab. 2: Procedure for preparation of symmetrical cells with electrospun electrodes [26].

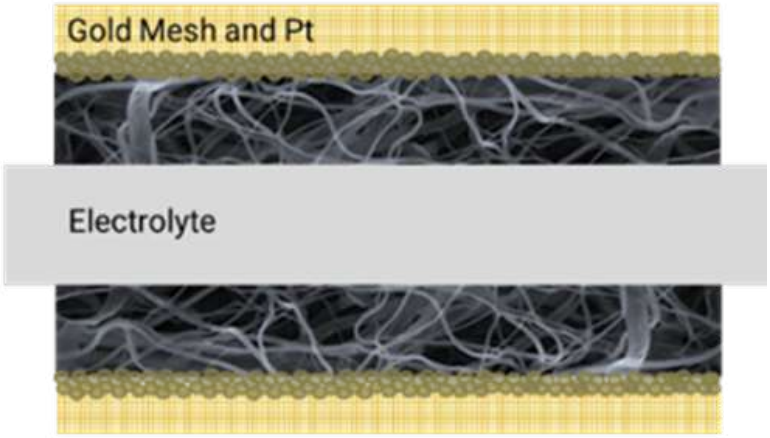

Fig. 5: Schematic representation of a symmetrical cell cross-section image.

1.3.2 Electrochemical Impedance Spectroscopy

Electrochemical Impedance Spectroscopy (EIS) represents a powerful tool for the electrode characterization of SOFCs. It is an application of the typical impedance measurement approach developed in electrical engineering Fig. 6 (a) and it is especially used for solid-state electrochemical cells such as SOFCs and solid oxide electrolysis cells (SOECs). The main charts involved in the interpretation of the EIS experimental data are the Nyquist and the Bode plots. The Nyquist plot reports the real part of impedance vs the imaginary part of the impedance and is essential to understand the overall polarization resistance (Rp) of the investigated cell, and thus their electrochemical performance. The Rp coincides with the segment individuated by the interceptions at high and low frequencies of the experimental data with the x-axis in the Nyquist plot. As far as the Bode plot is concerned, it represents the imaginary part of impedance vs the frequency. It is used to determine the maximum frequency of the arcs shown in the Nyquist plot, which is an essential parameter since the electrochemical phenomena are recognized by their maximum frequency.

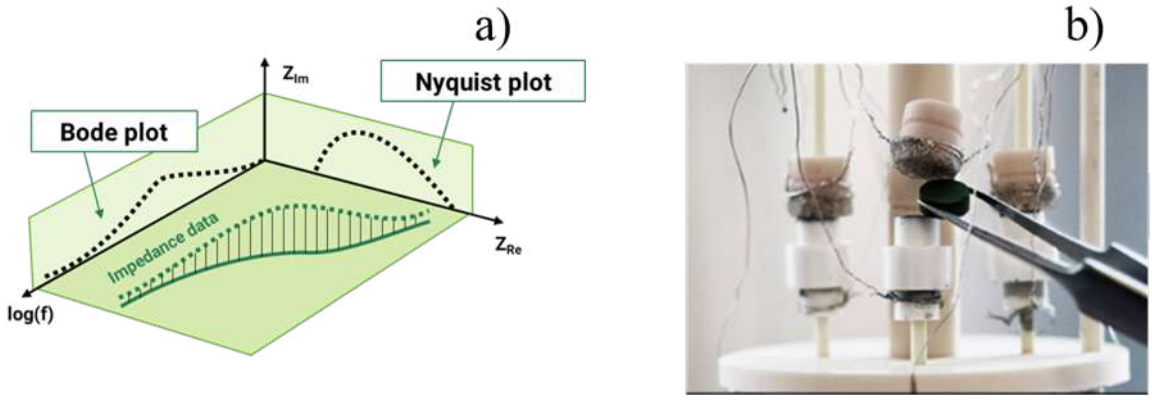

Fig. 6: EIS experimental technique: a) Bode and Nyquist visualization of impedance data; b) picture of the experimental test rig (courtesy of DTU Energy, Denmark).

The EIS characterization is normally carried out on symmetrical cells, which preparation is described in 1.2.1. After the symmetrical cell preparation process, the samples are mounted in a setup similar to the one shown in Fig. 6 (b). Each cell must be well fixed between the two current collectors, which typically are platinum or gold meshes to maximize the electrons flow inside the cell. The set-up is normally inserted in a furnace, which is sealed and connected to a gas supplier able to create the desired atmosphere. Lastly, the set-up is connected to impedance measurement equipment. Once the experimental data are acquired, they need to be interpreted in order to better understand the phenomena which take place inside the cell during the working condition. As far as metal oxide nanofiber-based SOFC electrodes are concerned, the type of modeling carried out in order to give an interpretation of the EIS experimental results is the so-called equivalent circuit (EC) modeling. This

modeling process consists in creating an equivalent electrical circuit, using physical elements equations, and fitting the experimental data through non-linear least squares (NLLS) algorithms [26].

1.3.2.1 Equivalent circuit (EC) modeling for nanofiber-based electrodes

The equivalent circuit models, as reported above, consist of electrical elements arranged in the specific circuit used to fit the EIS experimental data in order to understand the phenomena which take place inside the electrode under working conditions. The main circuit elements used in the EC modeling of metal oxide nanofiber-based electrodes for SOFCs are summarized in Tab. 3. Since the physical meaning of the equivalent circuit elements is known, it allows the possibility of acquiring essential information from the fitting parameters and thus qualitative and quantitative information from them. Several electrochemical processes are already described and analyzed in terms of their similarity to equivalent circuits [30,31].

Name	Chemical-physical phenomenon	Equation	Parameters
L	Inductance	$Z(\omega) = j\omega L$	L = inductance
R	Resistance	$Z(\omega) = R$	R = resistance
CPE	Double layer charge/discharge	$Z(\omega) = \frac{1}{Q(j\omega)^{\alpha}}$	Q = double layer capacitance*; α = fitting parameter
RQ	Electrochemical reaction through the electrochemical double layer*	$Z(\omega) = \frac{1}{R^{-1} + Q(j\omega)^{\alpha}}$	Q , α (same as above); R = resistance associated to charge transfer process
Gerischer (G)	Charge transport coupled to distributed electrochemical reaction	$Z(\omega) = \frac{1}{Y\sqrt{k + j\omega}}$	k = oxygen surface exchange coefficient; Y = structural parameters and solid phase oxygen diffusion coefficient
Finite-length-Warburg (FLW)	Gas phase diffusion	$Z(\omega) = \frac{\tanh(\sqrt{Bj\omega})}{\sqrt{Y_1 j\omega}}$	$B = \delta^2/D$ where δ = thickness of gas diffusion layer, and D = gas phase oxygen diffusion coefficient; Y_1 = phenomenological parameter

* The electrochemical double layer is the basic schematization of the electrochemical phenomena occurring at the TPB.

Tab. 3: Main impedance circuit elements used in the ECM of metal oxide nanofiber-based electrodes for SOFCs.

Generally, every EC contains an inductance L and a resistor R which are placed in series. The L element is used to simulate the inductance of the experimental apparatus, while the R element (also called Rs) takes into account all the ohmic resistances, which normally are referred to the electrolyte resistance. Then, the other elements which are added to the EC depend strongly on the properties of the investigated materials. One of the most used elements in EC modeling is the RQ, which consists of a resistance placed in parallel with a constant phase element. This element is used to simulate the electrochemical processes which take place at the interface between the electronic and the ionic conductor [31,32]. The charge transfer process, which is the oxygen reduction reaction (ORR) at the cathode side of the fuel cell, is simulated by the resistor, whereas for the electrode/electrolyte double

layer, the Q element is used. Composite electrodes based on LSM and GDC are generally modeled using circuits based on several RQ elements placed in series, such as L-Rs-RQ-RQ or L-Rs-RQ-RQ-RQ [33–35]. Another element that is widely used in EC models is the Gerisher element, which is used to simulate both charge transport and charge transfer reaction in the bulk of the electrode [36]. Mixed ionic and electronic conductors are generally well described with EC containing the G element [24,27,37,38]. Furthermore, at high temperatures the gas limitation phenomena start to give a considerable contribution, which results in an additional arc appearing at low frequencies, which is well fitted by the Finite-Length-Warburg (FLW) circuit element. From a quantitative point of view, the EC elements allow the precise determination of the polarization resistance Rp of the investigated electrode. The Rp coincides with the segment individuated by the interceptions at high and low frequencies of the experimental data in the Nyquist plot. As reported in Tab. 3, each element contributes to the overall polarization resistance, and with the EC modeling, it is possible to understand which are the limiting elements, and thus the limiting processes. There are several software which allow this type of modeling, such as Elchemea and Zview [39].

1.4 Electrodes manufacturing techniques adopted in this work

In this chapter, the electrode manufacturing process is reported in detail. Several electrospun nanofibers are prepared using different perovskites. The investigated electrodes are obtained using the electrospinning techniques, as described in chapter 1.3.1. For comparison, powder electrodes are obtained as well.

1.4.1 LSCF nanofibers and powders preparation

The perovskite stoichiometry follows the formula of $La_{0.6}Sr_{0.4}Co_{0.2}Fe_{0.8}O_{3-\delta}$ for both nanofibers and powders. As far as the nanofibers are concerned, the precursor metal salts used for the solution are $Sr(NO_3)_2$, $La(NO_3)_3 \bullet 6H_2O$, $Fe(NO_3)_3 \bullet 9H_2O$, $Co(NO_3)_2 \bullet 6H2O$ (all nitrates pure at 99.9% wt., and provided by Sigma-Aldrich). The carrier polymer is polyvinylpyrrolidone (PVP, Mw=1.3*106 g/mol, Sigma-Aldrich), which amount in the solution is 10% wt/wt. The solvent used for the dissolution of all the precursors is water. The LSCF nanofibers are electrospun (RT Advance, Linari Engineering, Pisa, Italy) on a rotating cylinder with the parameters reported in Tab. 4:

	Voltage [kV/cm]	Flow Rate [ml/h]	Rotational Speed [rpm]	Humidity [%]
LSCF	4	0.3	100	25

Tab. 4: Set of parameters used for the preparation of LSCF nanofibers.

The thermal treatment is set to 800°C with a ramp of 60°C/h, while between 350°C and 500°C the ramp is kept at 12°C/h.

The $La_{0.6}Sr_{0.4}Co_{0.2}Fe_{0.8}O_{3-\delta}$ granular powders are provided by Sigma-Aldrich, with a median particle diameter d50 = 0.9 µm ± 0.2 µm.

1.4.2 LSCF/GDC nanofibers and powders preparation

$La_{0.6}Sr_{0.4}Co_{0.2}Fe_{0.8}O_{3-\delta}$ (LSCF) / $Ce_{0.9}Gd_{0.1}O_{1.95}$ (GDC) co-electrospun nanofibers cathodes are obtained by simultaneous electrospinning of the two precursor solutions, and as described in chapter 1.2.2.1. The electrospinning apparatus is equipped with two spinnerets that are working in parallel, each of them fed with one solution. The solutions specification is reported in Tab. 5:

	Nitrates %wt/wt	PVP %wt/wt	Solvent %wt/wt
LSCF	28	10	62
GDC	8	9	83

Tab. 5: Specification of LSCF and GDC electrospinning solutions.

The solvent chosen for the LSCF is water, while for the GDC a mixture of 50%/50% wt/wt water/ethanol is used. The electrospinning parameters used for the preparation are reported in Tab. 6:

	Voltage [kV]	Flow Rate [ml/h]	Rotational Speed [rpm]	Humidity [%]
LSCF	3.3	0.3	150	25
GDC	3.3	1	150	25

Tab. 6: Set of the electrospinning parameters used to prepare the LSCF/GDC nanofibers.

1.4.3 LSM nanofibers and Powders preparation

The LSM nanofibers are obtained using the electrospinning technique, as described in chapter 1.2.2.1. The specification of the solution is reported in Tab. 7:

	Nitrates %wt/wt	PVP %wt/wt	Solvent %wt/wt
LSM	28	10	62

Tab. 7: Specification of LSM electrospinning solutions.

The solvent chosen for the LSM solution is a mixture of 60%/40% wt/wt water/ethanol. The electrospinning parameters used for the LSM nanofibers preparation are reported in Tab. 8:

	Voltage [kV]	Flow Rate [ml/h]	Rotational Speed [rpm]	Humidity [%]
LSM	3.3	0.3	[-] (Flat collector)	25

Tab. 8: Set of the electrospinning parameters used to prepare the LSM nanofibers.

For comparison, LSM powders prepared following the same stoichiometry, are characterized as well. The LSM powders are prepared through a self-combustion citrate-based procedure.

1.4.4 LSM, LSCuM_1, LSCuM_2 and LSCuF nanofibers preparation

Each electrode consisted of an inner ionic conductor nanofiber (core) covered by an electrocatalyst nanofiber (shell). The core is Gadolinium doped Ceria ($Ce_{0.9}Gd_{0.1}O_{1.95}$, GDC) in all cases. For the shell, different electrocatalysts were investigated: $La_{0.6}Sr_{0.4}MnO_3$ (LSM), $La_{0.6}Sr_{0.4}Cu_{0.1}Mn_{0.9}O_{3-\delta}$ (LSCuM_1), $La_{0.6}Sr_{0.4}Cu_{0.2}Mn_{0.8}O_{3-\delta}$ (LSCuM_2) and $La_{0.6}Sr_{0.4}Cu_{0.2}Fe_{0.8}O_{3-\delta}$ (LSCuF). The preparation process follows the steps reported in chapter 1.2.2.1. The two starting solutions are prepared following the instruction reported in chapter 1.3.1. The starting solutions contained the precursor metal salts, i.e. $La(NO_3)_3 \cdot 6H_2O$, $Sr(NO_3)_2$, $(CH_3COO)_2Mn \cdot 4H_2O$, $Cu(NO_3)_2 \cdot 3H_2O$, $Gd(NO_3)_3 \cdot 6H_2O$, and $Ce(NO_3)_3 \cdot 6H_2O$. For all the solutions, polyvinylpyrrolidone (PVP, Mw=1.3 10^6 g/mol), is added as carrier polymer, and N-N-Dimethylformamide (DMF) is selected as solvent. The salts are added to each solution to achieve the proper stoichiometry, which is reported in Tab. 9.

	La:Sr	Cu:Fe	Cu:Mn	Mn
LSM	6:4	[-]	[-]	1
LSCuM_1	6:4	[-]	1:9	[-]
LSCuM_2	6:4	[-]	2:8	[-]
LSCuF	6:4	2:8	[-]	[-]

Tab. 9: Molar ratios of the perovskite elements in the investigated electrocatalyst.

As far as the GDC stoichiometry is concerned, the molar ratio between Ce and Gd is 9:1. In the core solution, the PVP represented the 11.5% wt/wt, whereas, in every electrocatalyst solution, the PVP represented the 13% wt/wt. The electrospinning parameters selected for the process are reported in Tab. 10.

	Voltage [kV/cm]	Flow Rate [ml/h]	Rotational Speed [rpm]	Humidity [%]
Electrocatalyst	2.5	1	150	30-35
GDC	2.5	1	150	30-35

Tab. 10: Set of parameters for the core-shell electrospinning process.

After electrospinning, all the raw core-shell nanofibers tissues are cut in a circular shape and then heat-treated with a maximum temperature of 800°C, with a heating ramp of 60°C/h. However, between 350°C and 500°C, the heating ramp was set at 12°C/h to prevent the nanofibers degradation. The heat-treated electrode diameters and the consequent electrode area are reported in Tab. 11.

	Area [cm^2]	Radius [cm]
LSM	0.79	0.48
LSCuM_1	0.77	0.46
LSCuM_2	0.76	0.45
LSCuF	0.76	0.45

Tab. 11: Core-shell nanofibers electrode specifications.

The GDC electrolytes are made by pressing the GDC powder (particle size 0.1-0.4 μm, surface area 5.9 m2/g). Uniaxial pressing is carried out by filling the die body from the bottom achieving a high uniformity and obtaining a high-density sintered electrolyte. The electrolytes are prepared using a pressing force of 5 tons. Then, the electrolytes are sintered with a maximum temperature of 1300°C. After the sintering process, the complete cells are assembled attaching symmetrically the heat-treated electrodes using a droplet of GDC electrospinning solution as glue. The complete symmetrical cells were heat-treated at 950°C for 2 hours, using a thermal ramp of 60°C/h.

2. Experimental studies carried out during the Ph.D.

In this work, the manufacture and characterization of nanofiber-based electrodes are deeply investigated. The better electrochemical performance of nanofibers electrodes compared to powders-based ones is well described in the literature, generally for all the electrodes material. Thus, the first study reported in this work consists of the comparison between structural features and electrochemical performance of $La_{0.6}Sr_{0.4}Co_{0.2}Fe_{0.8}O_{3-\delta}$ nanofibers and granular powders. The $La_{0.6}Sr_{0.4}Co_{0.2}Fe_{0.8}O_{3-\delta}$ represents the state-of-the-art material for IT-SOFC cathodes and thus the best candidate for this work. The structural characterization of $La_{0.6}Sr_{0.4}Co_{0.2}Fe_{0.8}O_{3-\delta}$ nanofibers and granular powders was performed through high-temperature XRD data acquired at the Elettra synchrotron-based in Trieste (Italy), which were compared with EIS data acquired on the same samples. The results highlighted an interesting correlation between the variation of crystal structure and electrochemical performance (Rp) with temperature, suggesting that the activation energy Ea associated with the Rp accounts for both electrochemical phenomena and crystal structure variation. The main results are summarized in Section 2.1 of this work.

Then, the manufacture of an innovative composite electrode using the co-electrospinning technique is investigated. The composite electrode consisted in $La_{0.6}Sr_{0.4}Co_{0.2}Fe_{0.8}O_{3-\delta}$ and $Ce_{0.9}Gd_{0.1}O_{1.95}$ nanofibers which were simultaneously electrospun and randomly disposed on the electrode. The morphological and electrochemical characterization was carried out, as well as an aging investigation. The polarization resistance of these composite nanofiber-based electrodes turned out to be 5.6 Ωcm^2. The main results are summarized in Section 2.2 of this thesis, whereas the complete study is reported in Annex 1 (C. Sanna, W. Zhang, P. Costamagna, P. Holtappels, Synthesis and electrochemical characterization of La0.6Sr0.4Co0.2Fe0.8O3–δ / Ce0.9Gd0.1O1.95 co-electrospun nanofiber cathodes for intermediate-temperature solid oxide fuel cells, Int. J. Hydrogen Energy. 46 (2021) 13818–13831. https://doi.org/10.1016/j.ijhydene.2020.11.216“).

Due to the recent geopolitical problems related to Co extraction and commercialization, Co-free materials are intensively studied. Therefore, Co-free nanofibers-based electrodes are investigated, starting with the state-of-the-art cathode for HT-SOFC, the $La_{0.6}Sr_{0.4}MnO_3$. Firstly, structural and catalytic characterization of $La_{0.6}Sr_{0.4}MnO_3$ nanofibers and powders was carried out to point out any differences between the two architectures. The $La_{0.6}Sr_{0.4}MnO_3$ was also investigated for possible anode application in direct methane IT-SOFC. Then, composite electrodes based on $La_{0.6}Sr_{0.4}MnO_3$ and $Ce_{0.9}Gd_{0.1}O_{1.95}$ nanofibers and powders were structurally and electrochemically characterized to analyze the electrochemical performance for both cathode and anode applications. The polarization resistance achieved in the methane atmosphere at 815 °C is 0.15 Ωcm^2, ten times lower compared to

the cathode application. The main results are summarized in Sections 2.3 and 2.4 of this thesis, whereas the complete studies are reported in Annex 2 (E. Squizzato, C. Sanna, A. Glisenti, P. Costamagna, Structural and Catalytic Characterization of La0.6Sr0.4MnO3 Nanofibers for Application in Direct Methane Intermediate Temperature Solid Oxide Fuel Cell Anodes, Energies. 14 (2021) 3602. https:// doi.org/10.3390/en14123602.) and Annex 3 (C. Sanna, E. Squizzato, P. Costamagna, P. Holtappels, A. Glisenti, Electrochemical study of symmetrical intermediate temperature - solid oxide fuel cells based on La0.6Sr0.4MnO3 / Ce0.9Gd0.1O1.95 for operation in direct methane/air, Electrochim. Acta. 409 (2022) 139939. https://doi.org/10.1016/j.electacta.2022.139939).

Lastly, the attention was focused on improving the electrochemical performance of the $La_{0.6}Sr_{0.4}MnO_3$ and $Ce_{0.9}Gd_{0.1}O_{1.95}$ nanofibers electrode. Thus, $La_{0.6}Sr_{0.4}MnO_3/Ce_{0.9}Gd_{0.1}O_{1.95}$, $La_{0.6}Sr_{0.4}Cu_{0.1}Mn_{0.9}O_{3-\delta}/Ce_{0.9}Gd_{0.1}O_{1.95}$ and $La_{0.6}Sr_{0.4}Cu_{0.2}Mn_{0.8}O_{3-\delta}/Ce_{0.9}Gd_{0.1}O_{1.95}$ core-shell nanofibers electrode were structurally and electrochemically investigated as cathodes for IT-SOFC. The core-shell represents an innovative manufacturing technique, which makes it possible to prepare co-axial nanofibers with an inner ionic conductor nanofiber (core) covered by an electrocatalyst nanofiber (shell). The employment of the core-shell structure coupled with the Cu-doping of the LSM perovskite is demonstrated to improve the state-of-the-art electrochemical performance. The core-shell nanofibers cathodes turned out to be the most promising electrode architecture, indeed the LSM/GDC core-shell nanofibers achieved a polarization resistance of 0.28 Ωcm^2 at 850°C. The main results are summarized in Section 2.5 of this work.

2.1 $La_{0.6}Sr_{0.4}Co_{0.2}Fe_{0.8}O_{3-\delta}$ nanofibers and granular electrodes

This topic is the subject of a paper, currently in preparation, titled "Correlations between morphology, crystal structure, microstructure, and electrocatalytic properties in nanofiber and granular $La_{0.6}Sr_{0.4}Co_{0.2}Fe_{0.8}O_{3-\delta}$ perovskite for intermediate temperature solid oxide fuel cell cathodes" by Marta Daga, Caterina Sanna, Giorgio Bais, Maurizio Polentarutti, Sara Massardo, Marilena Carnasciali, Peter Holtappels, Paola Costamagna, Marcella Pani, Cristina Artini to be submitted to Applied Catalysis B: Environmental.

$La_{0.6}Sr_{0.4}Co_{0.2}Fe_{0.8}O_{3-\delta}$ electrospun nanofibers and commercial granular powders are investigated through synchrotron powder x-ray diffraction and electrochemical impedance spectroscopy in the temperature range of 550-900°C. The nanofibers manufacturing process is described in chapter 1.4.1. This study aims to correlate the structural modifications which may take place with the rising of temperature and the electrochemical performance of both LSCF nanofibers and powders. Indeed, the better electrochemical performance of nanofibers-based electrodes compared to powders-based ones is well described in the literature, but the explanation of this behavior hasn't been investigated in deep. In this chapter, the experimental data acquired at the Elettra synchrotron (Basovizza (TS), Italy) are analyzed and correlated with the EIS experimental data acquired at the Technical University of Denmark (DTU) for both LSCF nanofibers and powders.

2.1.1 High-temperature synchrotron x-ray diffraction set-up

The XRD characterization is carried out at the XRD1 beamline of the Elettra synchrotron, which is based in Trieste (Italy). The measurements are performed on the heat-treated LSCF nanofibers and LSCF powders. Both samples are separately crumbled and ground in an agate mortar, and subsequently put in quartz capillaries with an inner diameter of 0.5 mm. Patterns were collected for both samples at room temperature (RT), 500°C, 600°C, 700°C, 800°C, and 900°C in the 5-55° 2θ range, with the energy of the incident x-ray beam set at 18 keV (corresponding to λ=0.68881 Å). The high temperature is obtained through a blower and the capillary is maintained in rotation during measurements. The beamline is equipped with a Pilatus 2M detector, having 1475x1679 pixels with a size of 0.172 mm; during acquisitions, samples are placed at 85 mm from the detector; the spot size is 0.15x0.15 mm. The undesired fluorescence effect caused by the presence of Sr is reduced by setting a threshold at 16750 eV so that less energetic photons are discarded by the detector. The measurements are carried out also on an external standard, which is the LaB_6. This is done to calculate the instrumental resolution function to separate the sample and the instrument contribution to peak

broadening. The acquired 2D data are converted to 1D using the fit2D software, while a refinement with the Rietveld method is performed on the experimental patterns using the Full Prof software.

2.1.2 Electrochemical impedance spectroscopy set-up

The electrochemical performance of the LSCF nanofibers and powder electrodes is evaluated through EIS measurements. Firstly, both the nanofibers and powders symmetrical cells are prepared following the step reported in 1.2.1, while the electrolyte chosen for this project is made of GDC. To improve the adhesion of the nanofibers on the electrolyte, some electrospinning solution is used as glue, while the powders are added to some α-terpinol and deposited on the electrolyte as slurry. The final heat treatment is performed until 950°C, a temperature which is held for 2 hours. The final nanofibers electrode area is 0.32 cm^2 while the powder electrode area is 0.58 cm^2. Then, the symmetrical cells are placed in the experimental set up which is similar to the one reported in Fig. *6*. The EIS measurements are performed in an oxygen/argon atmosphere, with p_{O2} = 0.2 atm and p_{Ar} = 0.8 atm.

2.1.3 Results

2.1.3.1 Morphological characterization

Fig. 7 shows the SEM images of as-spun on as-spun (a-b) and heat-treated (c-d) LSCF nanofibers, acquired through a Zeiss Ultra 55 scanning electron microscope, using the secondary electrons detector with an acceleration voltage of 10 kV and 15 kV. Raw LSCF nanofibers appear continuous and well-elongated providing a good network. As far as the heat-treated nanofibers, it is possible to see that after the thermal treatment, there is no loss of morphology, indeed they appear still intact and well entangled.

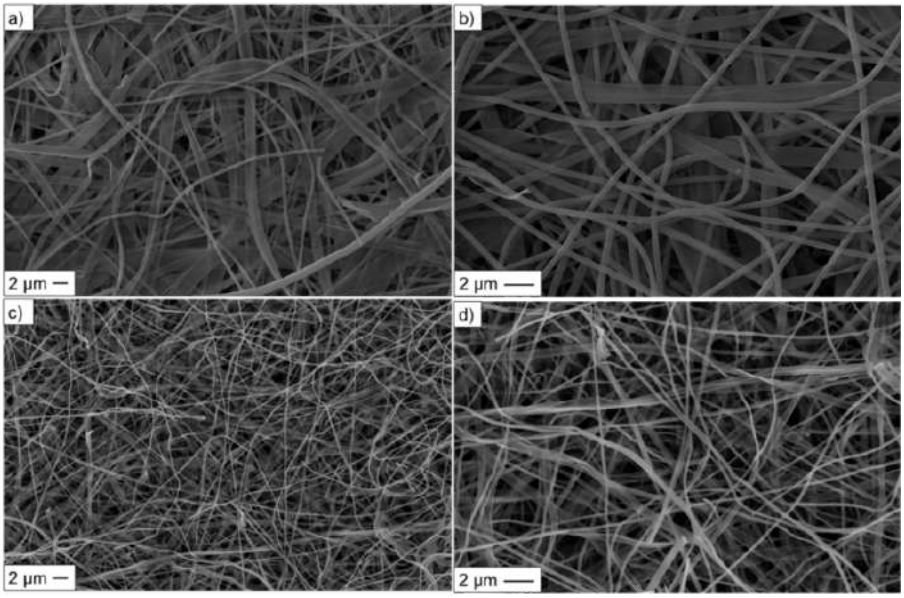

Fig. 7: SEM images of LSCF nanofibers before (a-b) and after (c-d) thermal treatment.

The average diameter of LSCF nanofibers before and after the thermal treatment is investigated as well, using the Image J tool called Diameter J. The analysis is carried out on the images reported in Fig. 7 (a) and (c) for raw and heat-treated nanofibers respectively, as well as on additional SEM images acquired on the same samples with the same magnification. The analysis results are shown in Fig. 8, where the relative frequency of specific diameter ranges is reported. The highest frequency for the raw LSCF nanofibers occurs at around 0.41 µm, while for the heat-treated it occurs at ~0.19 µm, suggesting a 50% reduction of the average fiber diameter as a consequence of the degradation of PVP during the thermal process [12].

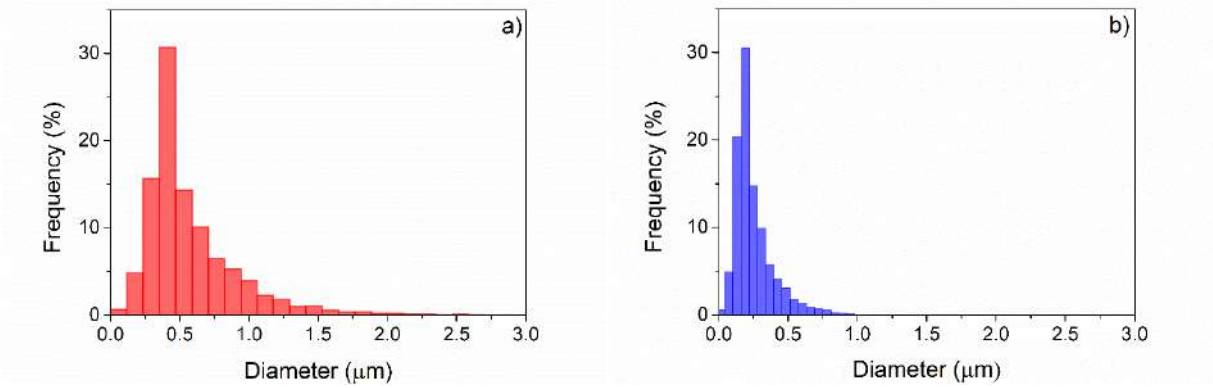

Fig. 8: Average diameter of nanofibers before (a) and after (b) thermal treatment. The diameter analysis is carried out on the SEM images reported in Fig. 7 (a) and (c).

The SEM characterization is carried out on LSCF commercial powder as well, and the results are reported in Fig. 9.

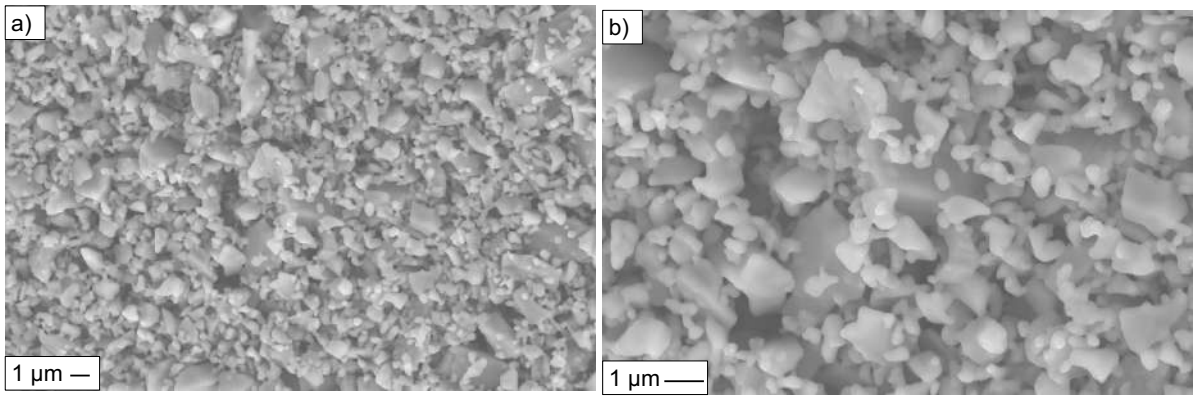

Fig. 9: SEM images of LSCF commercial powders.

2.1.3.2 Structural and electrochemical characterization

The two different LSCF morphologies are tested experimentally through synchrotron x-ray diffraction spectroscopy and EIS in the temperature range of 500-900°C. All the analyses shed a light on remarkable differences in properties between the two morphologies. In particular, the Rietveld method applied to the synchrotron results demonstrates that, for the nanofibers, the crystalline basic

cell is rhombohedral in all the investigated ranges of temperatures. Instead, the granular morphology has an R→C transition around 750 °C, as described in Fig. 10:

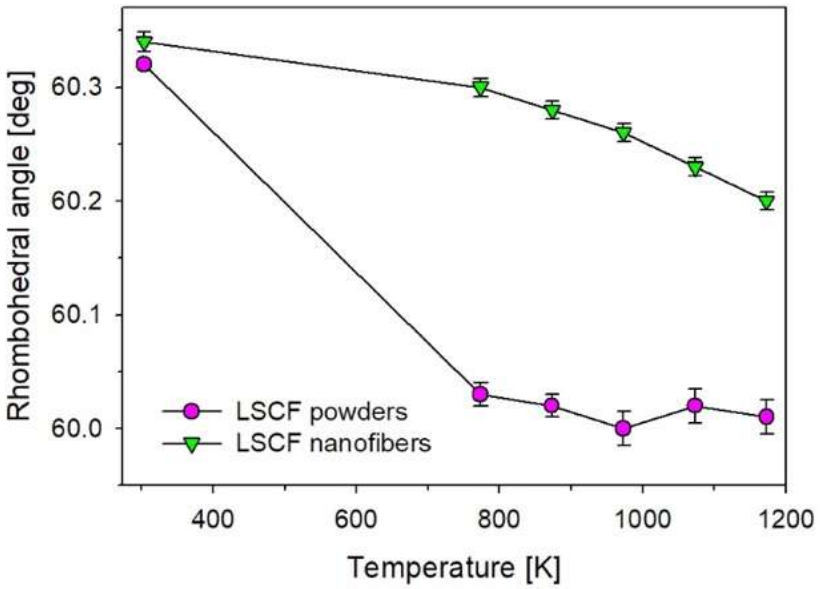

Fig. 10: α rhombohedral angle in powders and nanofibers as a function of temperature.

The evaluation of the electrocatalytic activity for the ORR is performed through EIS for both LSCF nanofibers and powders electrodes, as reported in Fig. 13. The interpretation of the EIS results is based on equivalent circuit fitting, through the Rs-RQ_1-RQ_2-G-FLW circuit. This equivalent circuit, used for both the nanofibers and the granular powders, is proposed as a general framework for the interpretation of EIS results obtained from LSCF electrodes. Each circuit element has a well-defined physical meaning. The RQ_1 element is associated to charge transfer from the electrolyte to the adjacent nanofiber/granule through their interfacial surface (surface path). G represents charge transfer simultaneous with electrochemical reaction inside the nanofibers/granules (bulk path). RQ_2 is associated to charge transfer through two adjacent nanofibers/granules through their interfacial surface (surface path). It is demonstrated that the variation of crystal features with temperature impact significantly on the charge transfer and electrochemical reaction processes. Therefore, the activation energies measured for all the electrochemical processes include a significant contribution originating from the variation of the crystal structure and associated properties. This approach makes it possible to better understand the EIS results obtained from LSCF granular electrodes at different operating temperatures, which often appear less reproducible compared to the nanofibers ones. It is recognized that the R→C transition boosts both the charge conduction and the electrochemical reaction inside the granules, reducing the G impedance. On the other hand, both the RQ_1 and RQ_2 surface paths are negatively affected by the R→C transition, possibly due to a distortion of the crystal lattice at the interfacial surfaces, caused by the transition itself. Therefore, it is recommended to design materials

for solid oxide fuel cell electrodes avoiding as much as possible crystal structure transition in the operating range.

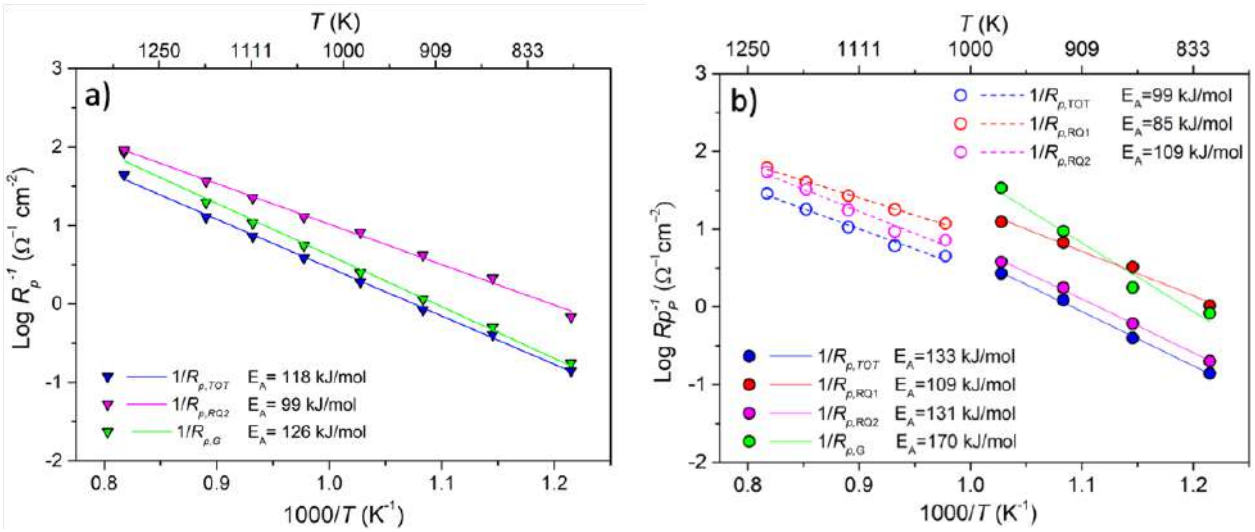

Fig. 11: Arrhenius plot of Rp-1 and the individual contributions associated with the different EC elements. The impedance of the FLW element is excluded. Lines are linear fittings, reported together with the associated activation energies. (a) LSCF nanofibers; (b) LSCF granular powders.

2.1.4 Final Remarks

$La_{0.6}Sr_{0.4}Co_{0.2}Fe_{0.8}O_{3-\delta}$ nanofibers and granular powders are structurally and electrochemically characterized through synchrotron powder x-ray diffraction and electrochemical impedance spectroscopy respectively. The correlation between the structural and electrochemical data explains how the R→C transition reduces the Gerisher resistance but affects the RQ surface paths. Thus, the nanofiber-based electrodes offer higher guarantees in this respect since the R→C transition temperature is above the operating range of IT-SOFCs. In conclusion, a strict correlation between morphology, crystal structure, and electrocatalytic properties is demonstrated for the LSCF perovskite to be used in IT-SOFC cathodes. These features, unprecedented for the present system, are expected to be beneficial in guiding the design of progressively more effective IT-SOFC electrode materials.

2.2 $La_{0.6}Sr_{0.4}Co_{0.2}Fe_{0.8}O_{3-\delta}/Ce_{0.9}Gd_{0.1}O_{1.95}$ co-electrospinning

A detailed description of this study is reported in the paper "C. Sanna, W. Zhang, P. Costamagna, P. Holtappels P., Synthesis and electrochemical characterization of $La_{0.6}Sr_{0.4}Co_{0.2}Fe_{0.8}O_{3-\delta}$/ $Ce_{0.9}Gd_{0.1}O_{1.95}$ co-electrospun nanofiber cathodes for intermediate-temperature solid oxide fuel cells, Int. J. Hydrogen Energy. 46 (2021) 13818–13831. https://doi.org/10.1016/j.ijhydene.2020.11.216." which is the Annex 1 of this work. Here, only the main points of this study are reported and discussed. The nanofibers manufacturing process is described in chapter 1.4.2. SEM characterization is carried out on both raw and heat-treated LSCF and GDC co-electrospun nanofibers, the results for the raw ones are reported in Fig. 12 (a-b) and the heat-treated ones are shown in Fig. 12 (c-d). The raw nanofibers are well entangled, with no detachments, while the heat-treated nanofibers images show thinner non-transparent nanofibers mixed with larger transparent nano- fibers, with ribbon features.

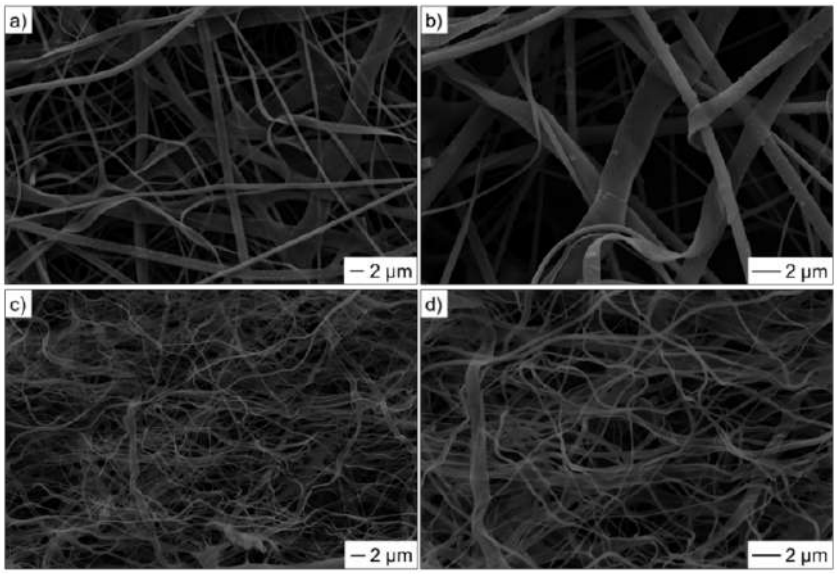

Fig. 12: SEM pictures of LSCF/GDC co-electrospun nanofibers: a) and b) as-electrospun tissue; c) and d) after thermal treatment.

Thus, EDX measurements are performed on the LSCF/GDC thermally treated tissue, to understand the composition of the individual nanofibers. Lanthanum is the main metal found in thick nanofibers, suggesting that they are made of LSCF. Conversely, cerium is the main metal found in thin nanofibers, suggesting that they are made of GDC. An ImageJ analysis is carried out to evaluate the average diameter of nanofibers, pointing out highest diameter probability is around 0.41 µm for the raw nanofibers, and around 0.20 µm for the thermally treated nanofibers. Finally, an XRD measurement is performed on the LSCF/GDC heat-treated tissue, confirming that the desired crystallinity is achieved for each material.

The EIS characterization is performed on LSCF/GDDC10 symmetrical cells, obtained following the steps reported in chapter 1.4.1. The tests are carried out in a 20% oxygen and 80% argon atmosphere,

in a temperature range between 600°C and 950°C. The experimental data are fitted through an Rs-RQ-G-FLW equivalent circuit model, demonstrating very low fitting error (0.1% at 800 °C and 0.05% at 950 °C). The Nyquist and bode plots obtained at 650°C are shown in Fig. 13. The polarization resistance is 5.6 Ωcm^2, which means that the electrode resistance is 5-6 times higher compared to electrospun pure LSCF fibers experimented in previous work.

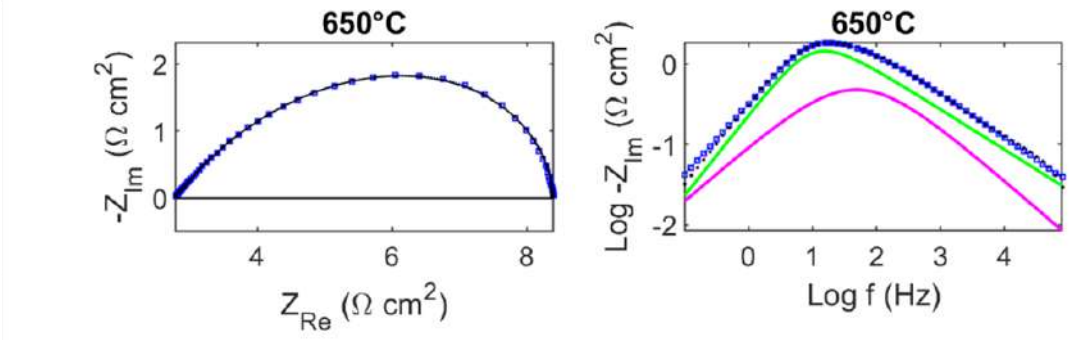

Fig. 13: Nyquist (left) and Bode (right) plots of the EIS results at operating temperatures from 650°C to 800°C: • experimental data; –□– fitting through the Rs-RQ-G equivalent circuit model; — Gerischer contribution; and — RQ contribution.

The high polarization resistance found for the investigation of LSCF/GDC co-electrospun nanofibers electrode may be explained by several percolation issues detected. Indeed, the high values obtained for the serial ohmic resistance Rs are explained in terms of a lack of percolation of the LSCF fibers throughout the electrode. This is attributed to the fact that the LSCF and GDC nanofibers do not have the same dimensions, with LSCF nanofibers being larger than those of GDC. As a consequence, only the GDC nanofibers percolate through the electrode, whereas percolation is hindered for the LSCF nanofibers, which exhibit larger sizes. This lack of percolation for the LSCF nanofibers results in a lack of electronic conduction through the electrode, which forces the electrochemical reaction to take place in the outer part of the electrode, at the interface with the current collector. The oxygen ions resulting from the electrochemical reaction are then transferred to the electrolyte through the percolating high-resistance ionic conduction path. Although, the LSCF/GDC nanofiber cathode shows reasonable stability during the electrochemical tests, with a 22% increase in the polarization resistance during 120 h of experimentation. A detailed analysis of the parameters of the Rs-RQ-G-FLW equivalent circuit model suggests that the source of degradation could be associated with a reduction in the number of contact points between LSCF and GDC fibers in the electrode over time. To conclude, percolation issues affect not only state-of-the-art bimodal granular electrodes but also bimodal nanofiber electrodes.

2.3 $La_{0.6}Sr_{0.4}MnO_3$ structural and catalytic characterization

The complete explanation of the experimental work carried out on the LSM nanofibers and powders is found in the article: "E. Squizzato, C. Sanna, A. Glisenti, P. Costamagna, Structural and Catalytic Characterization of La0.6Sr0.4MnO3 Nanofibers for Application in Direct Methane Intermediate Temperature Solid Oxide Fuel Cell Anodes, Energies. 14 (2021) 3602. https:// doi.org/10.3390/en14123602. ", which represents the Annex 2 of this thesis. Here, only the main points of this study are reported and discussed.

The nanofibers manufacturing process is described in chapter 1.4.3. The structural and catalytic characterization of $La_{0.6}Sr_{0.4}MnO_3$ (LSM) nanofibers and powder is reported in this chapter. An SEM characterization is carried out in order to control the morphology of the two samples. Fig. 14 (a-b) shows the LSM nanofibers after the thermal treatment, which is thin with no detachment, ensuring a compact network. The nanofibers show a preferential cylindrical shape which is the result of correct solvent evaporation during the electrospinning process. Fig. 14 (c-d) report the LSM powders, which are composed of particles with different dimensions and shape.

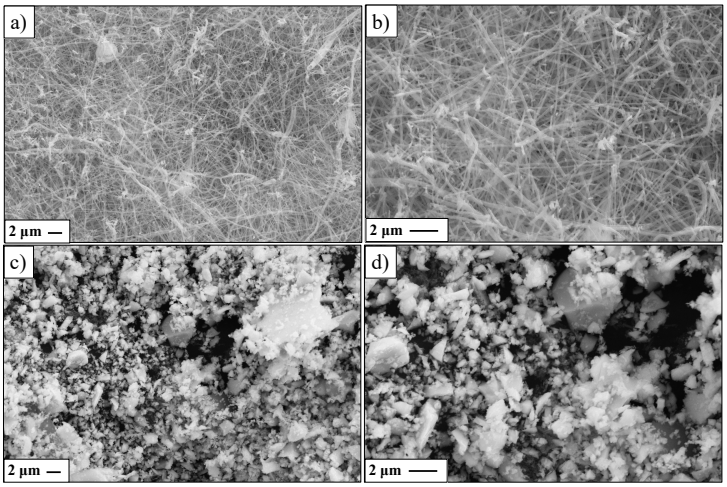

Fig. 14: SEM pictures of LSM nanofibers (a-b) and LSM powders (c-d).

Proper synthesis and crystallinity are confirmed for both samples by XRD. The X-ray photoelectron spectroscopy (XPS) measurements point out several differences between LSM nanofibers. In order to determine the BET surface area of the nanofibers, the N_2-adsorption-desorption isotherms are carried out on LSM nanofibers and powders. The calculated surface area of the LSM nanofibers is 16.7 m^2/g, a value which is greatly higher compared to the 5.8 m^2/g pointed out for the LSM powders. The XPS measurements are carried out on both samples, pointing out a structural difference between LSM nanofibers and powders. The result obtained for the Sr 3d spectrum of LSM is reported in Fig. 15:

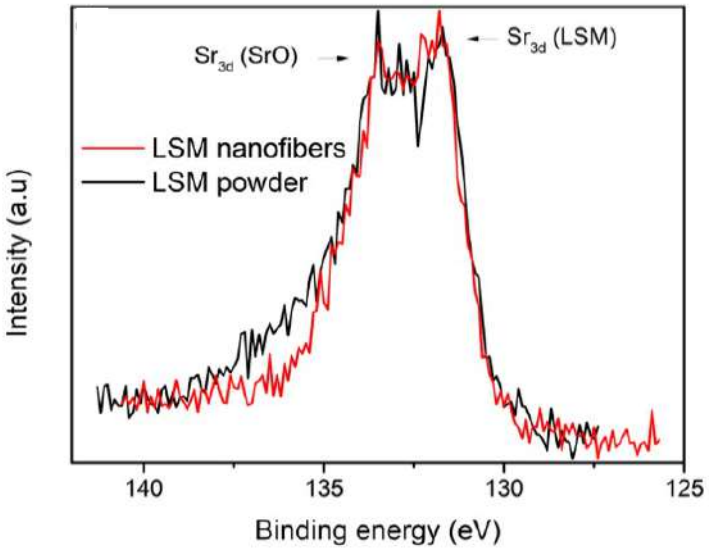

Fig. 15: Sr 3d XP spectra of LSM samples.

In the spectrum referred to the powders, in fact, it is possible to observe a tail around 135-137 eV which confirms the more relevant presence of SrO, which is not detected in the LSM nanofibers spectrum. This investigation demonstrates that the two different synthesis routes heavily influence the surface properties since LSM powders display strontium oxide segregation, which is not detected in nanofibers. As far as the La and Mn spectra, no differences are detected between the two samples. The catalytic activity towards direct methane oxidation is analyzed for the two samples, to investigate the possible employment of LSM as an anode for IT-SOFC. The result of this measurement is reported in Fig. 16:

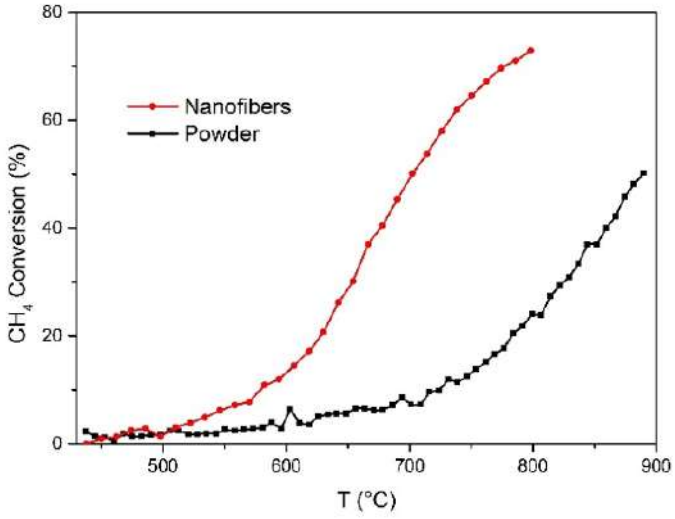

Fig. 16: Catalytic activity in methane oxidation observed for LSM powders (black line) and nanofibers (red line).

Fig. 16 shows that the onset temperature for methane oxidation is 500°C for the nanofibers and 600 °C for the powders. Methane conversion at 800°C is 73% with nanofibers and 50% at 900°C with powders. Two explanations are proposed for the superior nanofiber performance. The first is the absence of strontium oxide segregation on the surface, which exhibits perovskitic active sites till the last atomic layers. The second is the higher surface area.

In conclusion, the catalytic characterization performed through a methane oxidation activity test reveals a better catalytic performance of the LSM nanofibers, which is confirmed by the differences found with the structural characterizations.

2.4 $La_{0.6}Sr_{0.4}MnO_3$/ $Ce_{0.9}Gd_{0.1}O_{1.95}$ composite electrodes

The complete explanation of the experimental work carried out on the LSM nanofibers and powders is found in the article: "C. Sanna, E. Squizzato, P. Costamagna, P. Holtappels, A. Glisenti, Electrochemical study of symmetrical intermediate temperature - solid oxide fuel cells based on La0.6Sr0.4MnO3 / Ce0.9Gd0.1O1.95 for operation in direct methane/air, Electrochim. Acta. 409 (2022) 139939. https://doi.org/10.1016/j.electacta.2022.139939." which represents the Annex 3 of this thesis. Here, only the main points of this study are reported and discussed.

$La_{0.6}Sr_{0.4}MnO_3$ (LSM), which is considered a state-of-the-art SOFC cathode, in this chapter is investigated for both cathode and anode applications in direct methane intermediate temperature - solid oxide fuel cells (IT-SOFCs). The nanofibers manufacturing process is described in chapter 1.4.3. Two electrode architectures are investigated as both cathode and anode. The first one consists of LSM crushed nanofibers mixed with GDC powders, while the second one consists of LSM powders mixed with GDC powders. The choice to manufacture both nanofiber and powder-based electrodes is to investigate any differences due to the different preparation procedures as found for the catalytic characterization. The cell assembly follows the procedure reported in chapter 1.3.1, and the electrolytes used in this work are GDC ones. Both the LSM nanofibers and powders are prepared following the same procedure reported in chapter 5. The SEM characterization is carried out in order to visualize the morphology of the electrodes and the results are reported in Fig. 17:

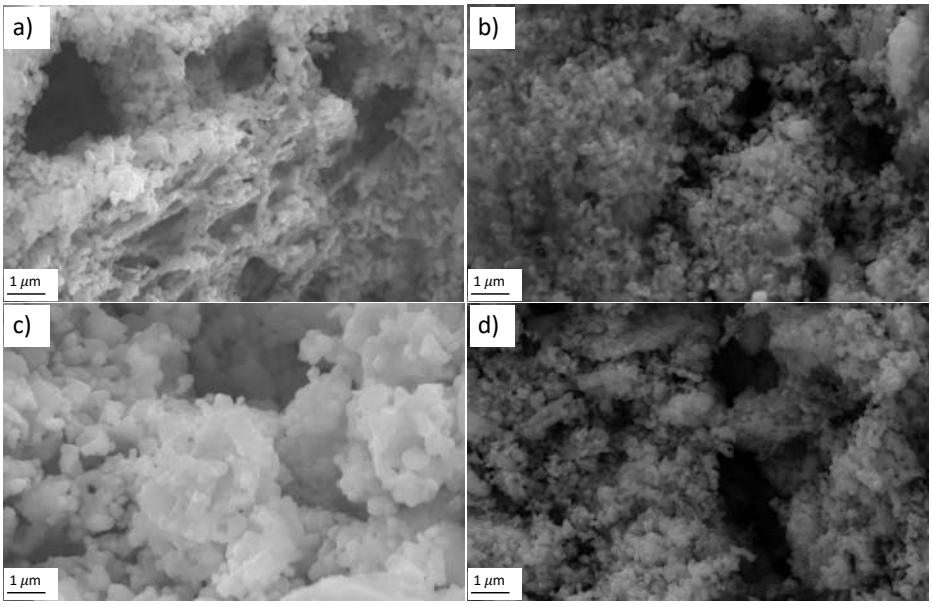

Fig. 17: SEM images of LSM/GDC nanofiber-based electrode (a-c) and LSM/GDC powder-based electrode (b-d). Electrode internal morphology: (a,b) pre-electrochemical test, (c,d) post-electrochemical test.

The grinding process used to mix the GDC with the LSM nanofibers leads to the loss of the original nanofiber structure, which is naturally well-elongated and arranged in a continuous network. Indeed,

due to the grinding process, no difference between LSM nanofibers (Fig. 17 (a)) and LSM powders (Fig. 17 (b)) is detected. Furthermore, it is possible to see that no difference in particle size between the GDC powders and the LSM is displayed, instead, the size distribution appears homogenous. Lastly, Fig. 17 (c-d) demonstrates no relevant changes in porosity and morphology despite the high temperatures reached during the electrochemical tests. The XRD measurements are carried out both after air exposure and methane exposure, to evaluate the stability and crystallinity in both atmospheres. The LSM/GDC electrodes show good structural stability in the oxidizing and reduction atmosphere. Although, the XRD measurements identify a change in the LSM crystal structure from the single perovskite obtained after the preparation process to the RP structure achieved after the exposition to the methane atmosphere. However, this transition is reversible after reoxidation. The XRD experimental patterns are reported in Fig. 18:

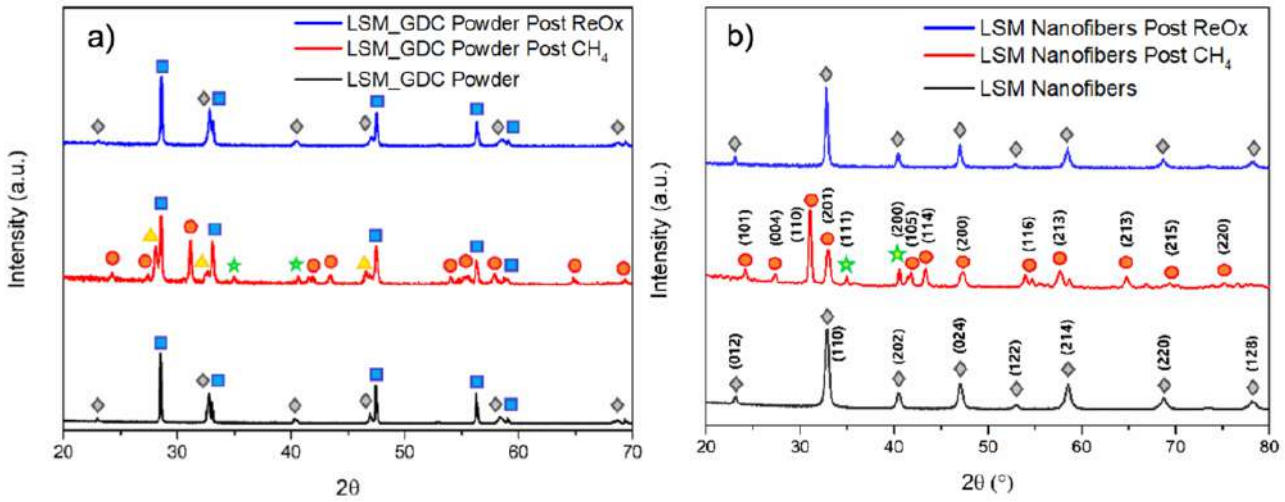

Fig. 18: a) LSM_GDC composite electrode and b) LSM nanofibers stability test results. Peak identification: blue square: $Ce_{0.9}Gd_{0.1}O_2$; Grey rhombus: $La_{0.6}Sr_{0.4}MnO_3$; Orange circles: $La_{1.2}Sr_{0.8}MnO_{3.84}$; Yellow triangle: $Ce_{11}O_{20}$; Green star: MnO.

The electrochemical characterization is carried out through EIS, performed both in air and in pure methane. As far as the air atmosphere is concerned, the equivalent circuit used for the experimental data fitting is the Rs-RQ-RQ(-RQ-FLW). The LSM/GDC electrodes show a good electrochemical performance in air, consistent with literature data, reporting a polarization resistance of 1.6 Ωcm^2 at 815 °C, as reported in the Nyquist plot shown in Fig. 19:

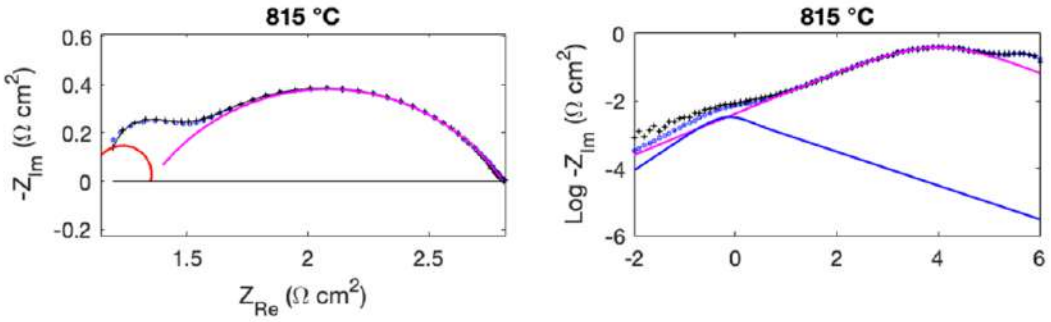

Fig. 19: Nyquist (left) and Bode (right) plots of the EIS results obtained with the nanofiber-based LSM/GDC electrode at 815°C, in air atmosphere: • experimental data; -□- fitting through the Rs-RQ-RQ-FLW equivalent circuit model; -- RQ1 contribution; -- RQ2 contribution and -- FLW contribution.

Furthermore, the LSM/GDC electrodes show even better electrochemical performance once tested as an anode, in the methane atmosphere. In reducing atmosphere, the equivalent circuit used for the data fitting involves the Gerisher element. The polarization resistance achieved at 815 °C is 0.15 Ωcm^2, ten times lower compared to the cathode application. These very low values obtained in the methane atmosphere may find an explanation by considering the possibility of a reduction of GDC. This can lead to the presence of a parallel electron conductive pathway that may not affect the shape and the description of the electrochemical impedance phenomena, but it may influence the measured R_p. In other cases, a contribution to the decrease of polarization resistance was attributed to the presence of C-nanoparticles whose formation was consequent to the use of methane. In this case, XPS allowed verifying the absence of relevant deposition of carbon (no significant differences between surface composition).

2.5 Core-shell nanofiber cathodes

This topic is the subject of a paper, titled "Electrochemical impedance spectroscopy of core-shell nanofibers cathodes, with $Ce_{0.9}Gd_{0.1}O_{1.95}$ (core) and Cu-doped $La_{0.6}Sr_{0.4}MnO_3$ (shell), for application in intermediate-temperature solid oxide fuel cells" by Caterina Sanna, Paola Costamagna and Peter Holtappels, currently submitted to Electrochimica Acta.

Several materials are investigated to prepare core-shell nanofibers electrodes for application as IT-SOFC cathodes. The materials investigated are the $La_{0.6}Sr_{0.4}MnO_3$ (LSM), $La_{0.6}Sr_{0.4}Cu_{0.1}Mn_{0.9}O_{3-\delta}$ (LSCuM_1), $La_{0.6}Sr_{0.4}Cu_{0.2}Mn_{0.8}O_{3-\delta}$ (LSCuM_2) and $La_{0.6}Sr_{0.4}Cu_{0.2}Fe_{0.8}O_{3-\delta}$ (LSCuF) perovskites coupled with the $Ce_{0.9}Gd_{0.1}O_{1.95}$ (GDC) fluorite. The nanofibers manufacturing process is described in chapter 1.4.4. The core-shell architecture consists in a perovskite solution which is electrospun simultaneously with the fluorite one, to provide nanofibers with a GDC core and LSM or Cu-based perovskite as a shell. The structural and electrochemical characterization of the core-shell nanofibers and their electrodes is performed. The polarization resistance of the LSM/GDC core-shell nanofiber electrodes is measured as Rp=4.5 Ωcm^2 at 650°C. This electrochemical performance is better than that of the LSM/GDC powder-based electrodes reported in chapter 6 (Rp=11 Ωcm^2 at 650°C). A further improvement is achieved with LSCuM_1/GDC and LSCuM_2/GDC, which reported a polarization resistance of around 0.9 Ωcm^2 and 0.8 Ωcm^2 respectively. A post-test SEM characterization is carried out as well, to ascertain possible degradation and identify the best core-shell nanofibers electrode.

2.5.1 Structural and morphological characterization

Fig. 20 shows the SEM images of the core-shell nanofibers after the thermal treatment: LSCuF/GDC (a-b), LSM/GDC (c-d), LSCuM_1/GDC (e-f), and LSCuM_2/GDC (g-h). From Fig. 20 (a-c-e-g) it is possible to see that the core-shell nanofibers tissue appears intact and well entangled in all the samples, providing a good network and a continuous path for both electrons and oxygen ions. Fig. 20 (b-d-f-h) highlights the morphology of the single core-shell nanofibers, which is similar in all the different samples. The GDC nanofibers (core) appear covered by a thin layer of electrocatalyst (shell), ensuring a good connection between the two phases and extending the TPB in the whole electrode thickness. Indeed, the continuous connection between the electronic conductor perovskite (shell) and the ionic conductor fluorite (core) is expected to promote the formation of many reaction sites along the whole core-shell nanofiber.

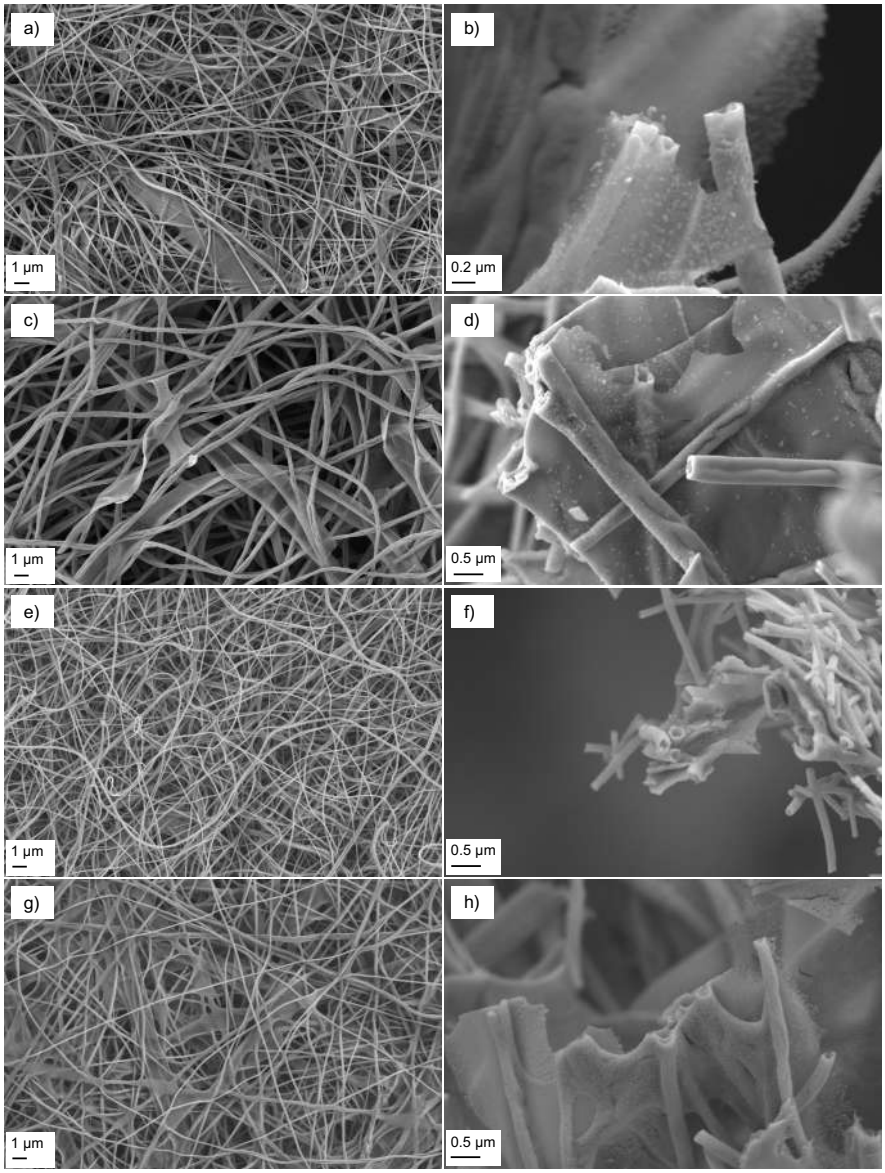

Fig. 20 – Core-shell nanofibers after the thermal treatment. a-b) LSCuF/GDC, b-c) LSM, d-e) LSCuM_1/GDC, (g-h) LSCuM_2/GDC.

Fig. 21 shows the morphology of the core-shell nanofibers after the EIS measurements: LSCuF/GDC (a-b), LSM/GDC (c-d), LSCuM_1/GDC (e-f), and LSCuM_2/GDC (g-h). Compared to Fig. 20, the core-shell nanofibers appear slightly broken but the morphology of the nanofibers is still present in all samples. As reported in Fig. 21 (a-b) and (e-f), the LSCuF/GDC and LSCuM_2/GDC show major signs of degradation compared to the other perovskites where the copper amount is present in a lower amount.

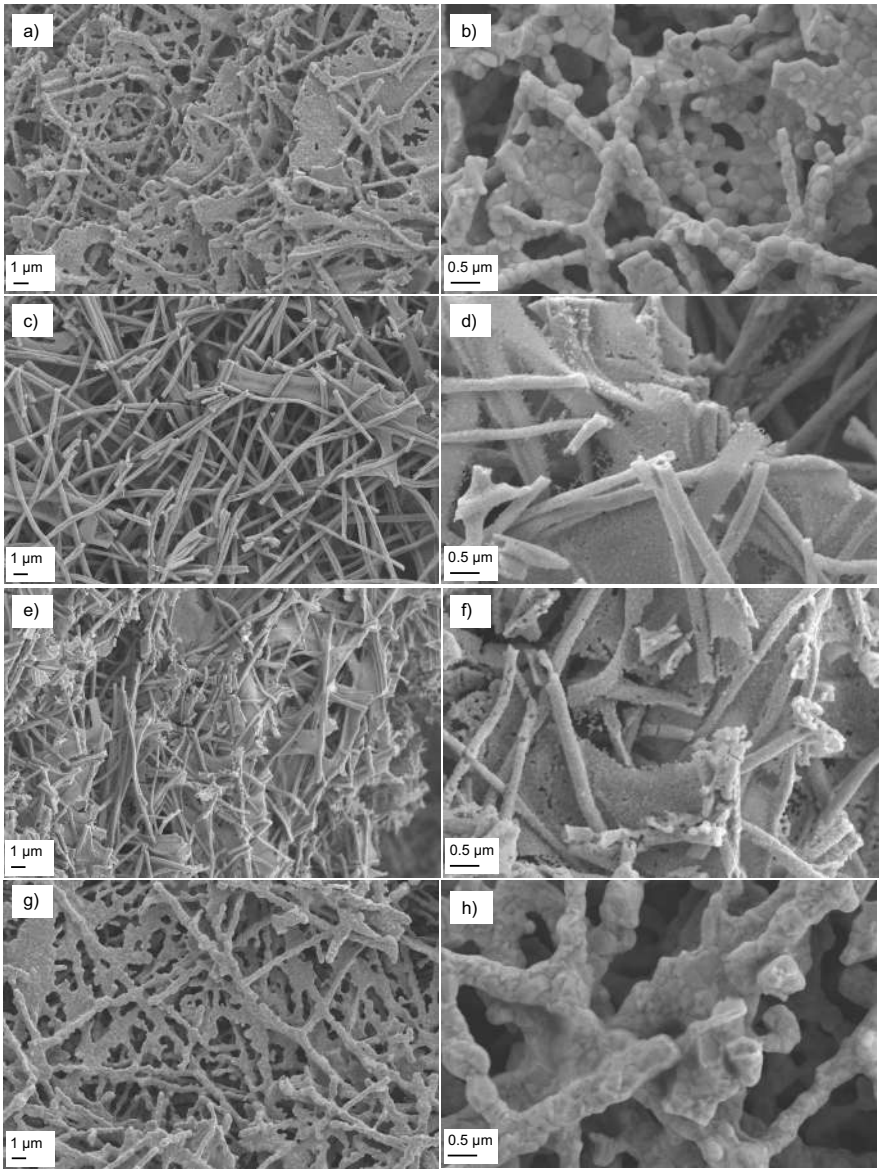

Fig. 21 – Core-shell nanofibers after the EIS measurements. a-b) LSCuF/GDC, b-c) LSM, d-e) LSCuM_1/GDC, g-h) LSCuM_2/GDC.

XRD measurements are acquired after the first heat-treatment process to check the achievement of the desired crystal phases and any eventual presence of secondary phases. In Fig. 22 the experimental patterns are reported within the reference patterns. LSM, LSCuM_1/GDC, and LSCuM_2/GDC core-shell nanofibers present an experimental pattern that contains all peaks related to the $La_{0.6}Sr_{0.4}MnO_3$ and the $Ce_{0.9}Gd_{0.1}O_{1.95}$ which are respectively the reference perovskite and fluorite. It is possible to see that the experimental patterns do not contain additional peaks, therefore no secondary phases are detected.

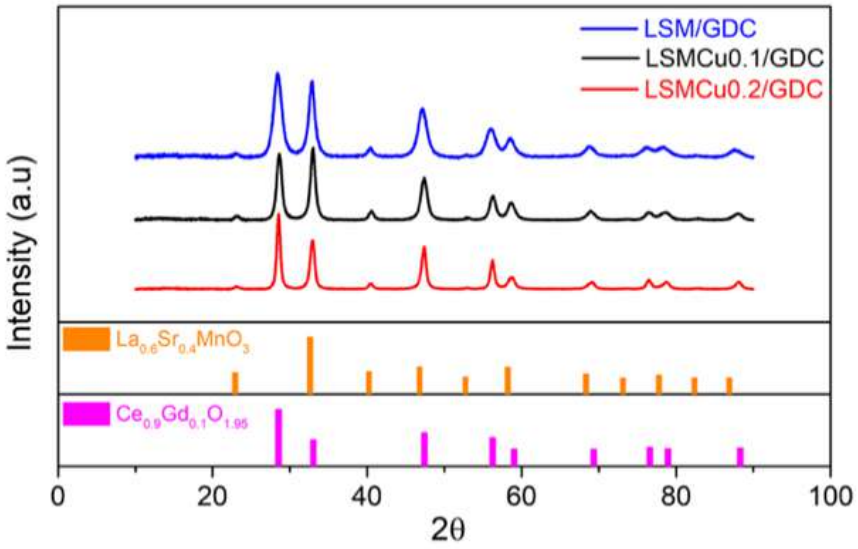

Fig. 22 – XRD experimental patterns of LSM/GDC (—), LSCuM_1/GDC (—), and LSCuM_2/GDC (—) within the La0.6Sr0.4MnO3 and Ce0.9Gd0.1O1.95 reference peaks.

In Fig. 23 the XRD experimental patterns after the EIS test are reported. The measurements are carried out on LSM, LSCuM_1/GDC, and LSCuM_2/GDC symmetrical cells after the electrochemical characterization, to investigate the stability of the electrode under working conditions. As shown in Fig. 23 all the experimental patterns contain the pick related to the reference pattern of $La_{0.6}Sr_{0.4}MnO_3$ and the $Ce_{0.9}Gd_{0.1}O_{1.95}$, confirming the maintenance of the starting crystal structure. All samples contain some additional picks which are consistent with the reference pattern of platinum, which is used as a current collector in the symmetrical cell assembly. No other additional picks are shown in Fig. 23, confirming the stability under working conditions.

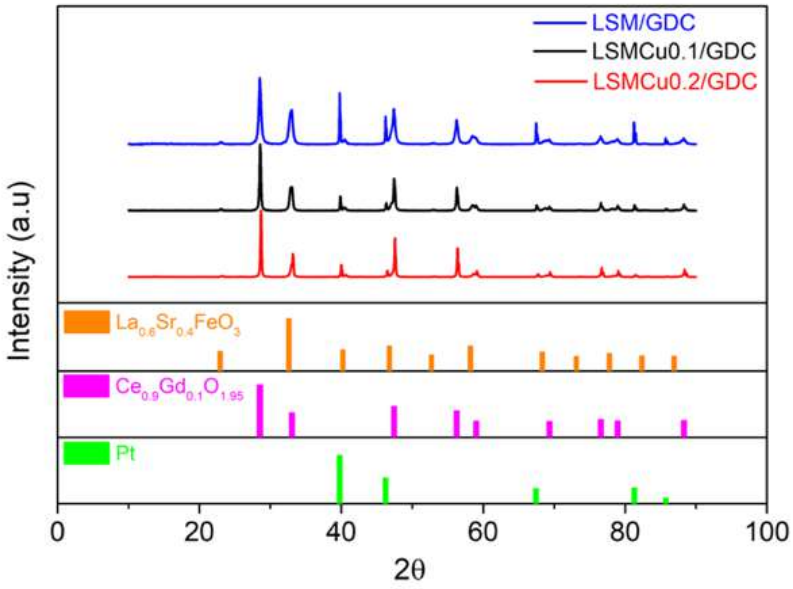

Fig. 23 – XRD experimental patterns of LSM/GDC (—), LSCuM_1/GDC (—), and LSCuM_2/GDC (—) after the EIS measurements, within the La0.6Sr0.4MnO3, Ce0.9Gd0.1O1.95, and Pt reference peaks.

As far as the LSCuF/GDC nanofibers, the XRD measurements are carried out as well. The measurements took place before the EIS test to detect eventually secondary phases which might compromise the electrochemical characterization.

2.5.2 Electrochemical characterization

Fig. 24 reports the Nyquist and Bode plots of LSM/GDC, LSCuM_1/GDC, LSCuM_2/GDC, and LSCuF/GDC core-shell nanofibers electrodes, at the operating temperature of 700°C. The equivalent circuit used to fit the experimental data consisted of several RQs placed in series in the case of LSM/GDC, LSCuM_1/GDC, and LSCuM_2/GDC. Conversely, the LSCuF/GDC EIS data are fitted with an equivalent circuit containing a Gerischer element. At each investigated temperature it was possible to identify two main arcs, one at high frequency and one at middle-low frequencies. The first one was well fitted using only one RQ element, which is named RQ1, for all the core-shell electrodes. The middle-low frequency arc is fitted with two RQ elements, RQ2 and RQ3, in the case of the manganite materials, and with the Gerischer element and the RQ2 in the case of the LSCuF/GDC. Despite the presence of both electronic and ionic conductivity inside all the composite electrodes, there is no presence of Gerischer behavior in the LSM/GDC, LSCuM_1/GDC, and LSCuM_2/GDC. The Gerischer element is normally detected in the case of mixed ionic and electronic conductor materials, such as $La_{1-x}Sr_xCo_yFe_{1-y}O_{3-\delta}$ [27,28,37] and similar materials (such as LSCuF).

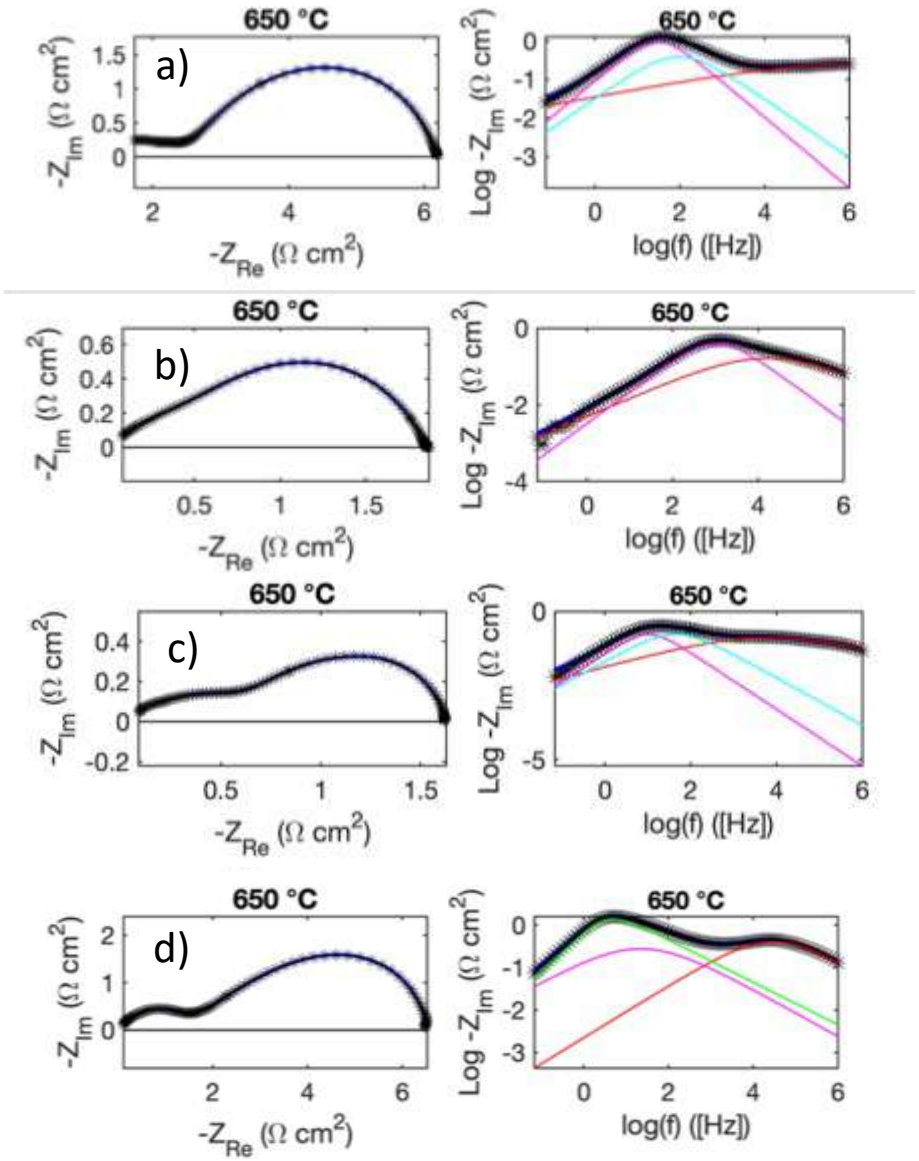

Fig. 24 - Nyquist (left) and Bode (right) plots of the EIS measurements obtained with the LSM/GDC (a), LSCuM_1/GDC (b), LSCuM_2/GDC (c), and LSCuF/GDC (d) core-shell nanofibers electrode at 650°C: • experimental data; -*- fitting through the equivalent circuit model; -- RQ1 contribution; -- RQ2 contribution; -- RQ3 contribution; -- G contribution.

The no-Gerisher behavior of Mn-based perovskites may be explained starting from the morphological properties of composite electrodes. In composite electrodes, the ionic conduction and the electronic conduction paths are placed in two different materials, and the oxygen reduction reaction (ORR) can take place only where there is a connection point between the two materials. Thus, the charge transfer takes place in these active sites and the oxygen ions produced during the reaction follow the ionic path along the ionic conductor material. On the other side, in MIEC materials the two paths coexist in the same material. Thus, the ORR can take place at any site, and the oxygen ions produced during the electrochemical reaction follow the ionic path which is inside the same material. A schematic representation of the electrochemical reaction performed in composite electrodes and the MIEC electrodes process is reported in Fig. 25.

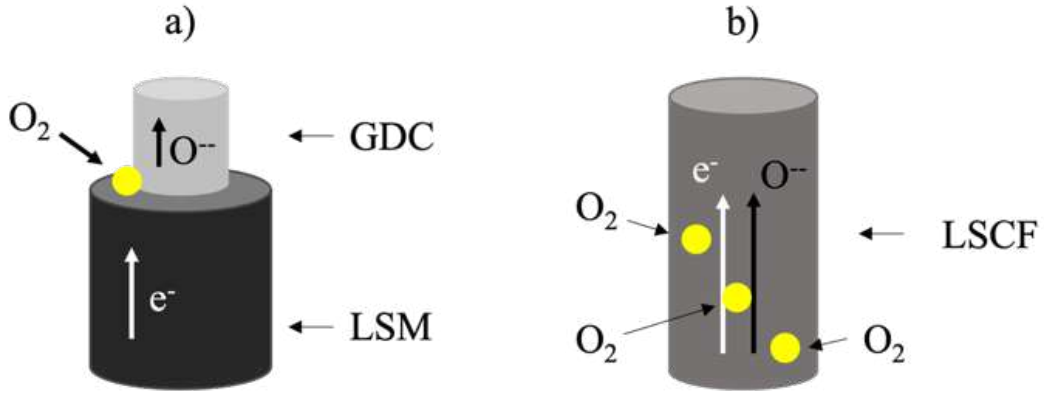

Fig. 25 – The charge transfer process of an electrochemical reaction in the composite electrode (a) and MIEC materials (b). The • represents the reaction active site.

As far as the electrochemical performance is concerned, the results achieved with the EIS measurements are analyzed and compared to the literature. As reported in Fig. 24, the polarization resistance of the LSM/GDC core-shell nanofibers electrode is around 4.5 Ωcm^2 at 650°C, a value that decreases rising temperature, reaching 0.28 Ωcm^2 at 850°C. The LSM/GDC composite powder-based electrodes tested during my second year of Ph.D., reported an R_P around 11 Ωcm^2 at 650 °C and 1 Ωcm^2 at 850 °C. Therefore, the LSM/GDC core-shell nanofibers electrodes turned out to be very promising at both low and intermediate operating temperatures.

As far as LSCuM_1/GDC and LSCuM_2/GDC core-shell nanofibers are concerned, the polarization resistances achieved with these cathodes appeared interesting. Indeed, as reported in Fig. 24, the Cu-based perovskite materials show better performance compared to the LSM/GDC core-shell nanofibers. Indeed, at 650°C the polarization resistance of the LSCuM_1/GDC and LSCuM_2/GDC core-shell nanofibers cathodes are around 1.8 Ωcm^2 and 1.6 Ωcm^2 respectively. These numbers confirm the expected efficiency of Cu, which improves the electrocatalytic activity of LSM-based electrodes. Finally, the R_P of LSCuF/GDC, reported in Fig. 24 as well, is around 2.5 Ωcm^2 at 650 °C.

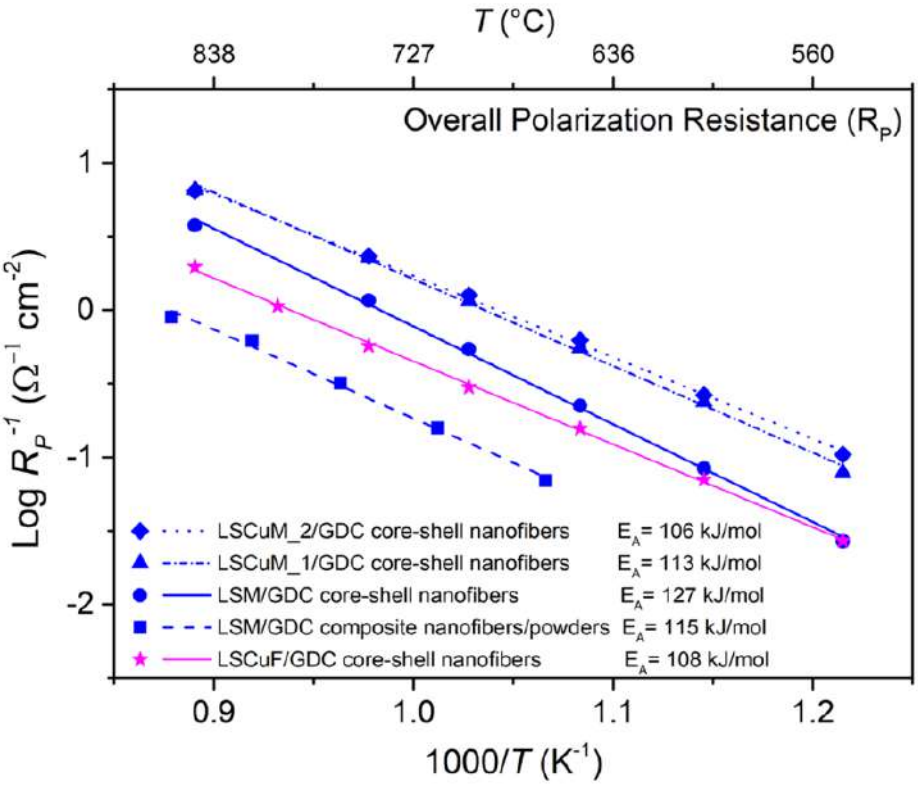

Fig. 26: - Arrhenius plot of Rp^{-1} of LSM/GDC, LSCuM_1/GDC, LSCuM_2/GDC, and LSCuF/GDC core-shell nanofibers.

Fig. 26 shows the Arrhenius plot of the overall polarization resistances for each Mn-based investigated core-shell nanofibers electrode. It is possible to see that all the core-shell nanofibers electrodes have better performance compared to the powder-based LSM/GDC composite cathode, reported previously in chapter 6. In particular, the LSCuM_1/GDC and LSCuM_2/GDC core-shell nanofibers electrodes are the best in terms of electrochemical performances. Furthermore, it is possible to see that the addition of Copper to the LSM perovskite has the effect to decrease the activation energy of the overall polarization resistance process. In particular, the LSCuM_2/GDC core-shell nanofibers report the lowest value of activation energy (106 kJ/mol). As far as the electrochemical performance is concerned, the LSCuM_2/GDC shows the lowest polarization resistance, similar to that of LSCuM_1/GDC.

Another important remark regards degradation. As shown in Fig. 21, the higher the amount of Cu in the perovskite, the stronger the degradation during the EIS measurements. Therefore, even if the electrochemical performance of the Cu-doped materials is similar, the LSCuM_1/GDC core-shell nanofibers grant a lower degradation and higher morphological stability.

2.5.3 Final Remarks

The core-shell nanofibers cathodes turn out to be a promising electrode architecture for IT-SOFC applications. Indeed, this innovative electrode structure provides interesting electrochemical performances with all the investigated perovskites. Furthermore, the copper-based core-shell nanofibers electrodes reported better electrochemical performance compared to LSM-based. Indeed, the polarization resistance obtained with the LSCuM_2/GDC at 700°C is 0.8 Ωcm^2, while the LSM/GDC shows an Rp of 1.9 Ωcm^2 at the same operating temperature. Nevertheless, it is important to control the amount of copper inside the perovskite, in order to avoid electrode degradation.

3. General Conclusions

Several nanofibers-based electrodes are morphologically and electrochemically characterized. It is possible to draw the following conclusions:

- The electrospinning process represents an innovative and powerful technique to produce nanofibers-based electrodes. Indeed, several characterizations such as XRD, XPS, and BET point out structural and morphological differences between the electrospun nanofibers and granular powders, which are considered state-of-the-art electrode architecture. The electrochemical characterization carried out through EIS measurements confirms the better performance of the nanofibers-based electrodes compared to the powders-based ones.
- Among all the investigated electrode architectures, the core-shell nanofibers electrode has been demonstrated to be the most promising. Indeed, the continuous connection between the ionic conductor and electronic conductor achieved with the co-axial electrospinning process allows the extension of the TPB inside the whole electrode volume. Furthermore, it is possible to avoid any percolation problem, identified with the co-electrospun nanofiber cathode.
- Copper-based core-shell nanofibers electrodes reported better electrochemical performance compared to LSM-based and LSCF-based electrodes. Indeed, the polarization resistance obtained with the LSCuM_2/GDC at 700°C is 0.8 Ωcm^2, while the LSM/GDC shows an Rp of 1.9 Ωcm^2 at the same operating temperature. Thus, the $La_{0.6}Sr_{0.4}Cu_xMn_{1-x}O_{3-\delta}$ perovskite has been demonstrated to be a promising cathode material for IT-SOFC application. Nevertheless, it is important to control the amount of copper inside the perovskite, in order to avoid electrode degradation.
- Electrochemical impedance spectroscopy is a powerful tool for the characterization of IT-SOFC electrodes. In particular, the EIS experimental data and EC modeling confirm the absence of Gerischer behavior for the LSM, LSCuM_1, and LSCuM_2, whereas it is detected in LSCF and LSCuF. Instead, the manganite-based cathodes EIS experimental data perfectly fit with RQ-based EC. This suggests that only MIEC electrodes featuring electronic/ionic conductivity and electrochemical reaction inside the same material display a Gerischer element in the EIS experimental data. Conversely, in composite electrodes, where electronic and ionic conductions occur in two different materials with the electrochemical reaction at the interface, the EIS response is dominated by the RQ elements associated with the interfacial charge transfer reaction.

List of Abbreviations

- LSM = $La_{0.6}Sr_{0.4}MnO_3$
- LSCuM_1 = $La_{0.6}Sr_{0.4}Cu_{0.1}Mn_{0.9}O_{3-\delta}$
- LSCuM_2 = $La_{0.6}Sr_{0.4}Cu_{0.2}Mn_{0.8}O_{3-\delta}$
- LSCuF = $La_{0.6}Sr_{0.4}Cu_{0.2}Fe_{0.8}O_{3-\delta}$
- LSCF = $La_{0.6}Sr_{0.4}Co_{0.2}Fe_{0.8}O_{3-\delta}$
- GDC = $Ce_{0.9}Gd_{0.1}O_{1.95}$
- EIS = Electrochemical Impedance Spectroscopy
- ORR = Oxygen Reduction Reaction
- SEM = Scanning Electron Microscope
- XRD = X-Ray Diffraction
- XPS = X-ray photoelectron spectroscopy
- MIEC = Mixed Ionic and Electronic Conductor
- SOFC = Solid Oxide Fuel Cells
- EC = Equivalent Circuit
- TPB = Triple Phase Boundary
- PVP = Polyvinylpyrrolidone

References

[1] K. Huang, J.B. Goodenough, Solid oxide fuel cell technology, Woodhead Publishing Limited, Cambridge, UK, 2009.

[2] S.P. Jiang, Development of lanthanum strontium cobalt ferrite perovskite electrodes of solid oxide fuel cells – A review, Int. J. Hydrogen Energy. 44 (2019) 7448–7493. https://doi.org/10.1016/j.ijhydene.2019.01.212.

[3] P. Costamagna, P. Costa, V. Antonucci, Micro-modelling of solid oxide fuel cell electrodes, Electrochim. Acta. 43 (1998) 375–394. https://doi.org/10.1016/S0013-4686(97)00063-7.

[4] S. Tao, J.T.S. Irvine, Discovery and Characterization of Novel Oxide Anodes for Solid Oxide Fuel Cells, (2004) 83–95. https://doi.org/10.1002/tcr.20003.

[5] E. Jud, L.J. Gauckler, The effect of cobalt oxide addition on the conductivity of Ce 0.9Gd0.1O1.95, J. Electroceramics. 15 (2005) 159–166. https://doi.org/10.1007/s10832-005-2193-3.

[6] P. Kaur, K. Singh, Review of perovskite-structure related cathode materials for solid oxide fuel cells, Ceram. Int. 46 (2020) 5521–5535. https://doi.org/10.1016/j.ceramint.2019.11.066.

[7] G. Yang, W. Jung, S.J. Ahn, D. Lee, Controlling the oxygen electrocatalysis on perovskite and layered oxide thin films for solid oxide fuel cell cathodes, Appl. Sci. 9 (2019). https://doi.org/10.3390/app9051030.

[8] S.P. Jiang, Development of lanthanum strontium manganite perovskite cathode materials of solid oxide fuel cells: A review, 2008. https://doi.org/10.1007/s10853-008-2966-6.

[9] G. Nirala, D. Yadav, S. Upadhyay, Ruddlesden-Popper phase A2BO4 oxides: Recent studies on structure, electrical, dielectric, and optical properties, J. Adv. Ceram. 9 (2020) 129–148. https://doi.org/10.1007/s40145-020-0365-x.

[10] M. Ghamarinia, A. Babaei, C. Zamani, Electrochimica Acta Electrochemical characterization of La 2 NiO 4 -infiltrated La 0 . 6 Sr 0 . 4 Co 0 . 2 Fe 0 . 8 O 3- d by analysis of distribution of relaxation times, 353 (2020) 1–9. https://doi.org/10.1016/j.electacta.2020.136520.

[11] B. Shri Prakash, S. Senthil Kumar, S.T. Aruna, Properties and development of Ni/YSZ as an anode material in solid oxide fuel cell: A review, Renew. Sustain. Energy Rev. 36 (2014) 149–179. https://doi.org/10.1016/j.rser.2014.04.043.

[12] L.J. Gauckler, D. Beckel, B.E. Buergler, E. Jud, U.P. Muecke, M. Prestat, J.L.M. Rupp, J. Richter, Solid oxide fuel cells: Systems and materials, Chimia (Aarau). 58 (2004) 837–850. https://doi.org/10.2533/000942904777677047.

[13] M.J. Escudero, J.T.S. Irvine, L. Daza, Development of anode material based on La-substituted SrTiO3 perovskites doped with manganese and/or gallium for SOFC, J. Power

Sources. 192 (2009) 43–50. https://doi.org/10.1016/j.jpowsour.2008.11.132.

[14] X. Li, H. Zhao, W. Shen, F. Gao, X. Huang, Y. Li, Z. Zhu, Synthesis and properties of Y-doped SrTiO3 as an anode material for SOFCs, J. Power Sources. 166 (2007) 47–52. https://doi.org/10.1016/j.jpowsour.2007.01.008.

[15] C. Marcilly, P. Courty, B. Delmon, Preparation of highly dispersed mixed oxides and oxide solid solutions, J. Am. Ceram. Soc. 53 (1970) 56. https://doi.org/10.1111/j.1151-2916.1970.tb12003.x.

[16] X.L. Xu, J.D. Guo, Y.Z. Wang, A novel technique by the citrate pyrolysis for preparation of iron oxide nanoparticles, Mater. Sci. Eng. B Solid-State Mater. Adv. Technol. 77 (2000) 207–209. https://doi.org/10.1016/S0921-5107(00)00485-2.

[17] A. Barbucci, R. Bozzo, G. Cerisola, P. Costamagna, Characterisation of composite SOFC cathodes using electrochemical impedance spectroscopy . Analysis of Pt / YSZ and LSM / YSZ electrodes, 47 (2002) 2183–2188.

[18] P. Costamagna, M. Panizza, G. Cerisola, A. Barbucci, Effect of composition on the performance of cermet electrodes. Experimental and theoretical approach, 47 (2002) 1079–1089.

[19] P. Costamagna, P. Costa, E. Arato, Some more considerations on the optimization of cermet solid oxide fuel celle electrodes, Electrochim. Acta. 43 (1998) 967–972.

[20] E. Squizzato, C. Sanna, A. Glisenti, P. Costamagna, Structural and Catalytic Characterization of La0.6Sr0.4MnO3 Nanofibers for Application in Direct Methane Intermediate Temperature Solid Oxide Fuel Cell Anodes, Energies. 14 (2021) 3602.

[21] E. Zhao, C. Ma, W. Yang, Y. Xiong, J. Li, C. Sun, Electrospinning La0.8Sr0.2Co0.2Fe 0.8O3-δ tubes impregnated with Ce 0.8Gd0.2O1.9 nanoparticles for an intermediate temperature solid oxide fuel cell cathode, Int. J. Hydrogen Energy. 38 (2013) 6821–6829. https://doi.org/10.1016/j.ijhydene.2013.03.111.

[22] V.C. Kournoutis, F. Tietz, S. Bebelis, AC impedance characterisation of a La0.8Sr0.2Co 0.2Fe0.8O3-δ electrode, Fuel Cells. 9 (2009) 852–860. https://doi.org/10.1002/fuce.200800120.

[23] V. Dusastre, J.A. Kilner, Optimisation of composite cathodes for intermediate temperature SOFC applications, Solid State Ionics. 126 (1999) 163–174. https://doi.org/10.1016/S0167-2738(99)00108-3.

[24] E. Zhao, Z. Jia, L. Zhao, Y. Xiong, C. Sun, M.E. Brito, One dimensional La 0.8Sr 0.2Co 0.2Fe 0.8O 3-δ/Ce 0.8Gd 0.2O 1.9 nanocomposite cathodes for intermediate temperature solid oxide fuel cells, J. Power Sources. 219 (2012) 133–139.

https://doi.org/10.1016/j.jpowsour.2012.07.013.

[25] E. Zhao, X. Liu, L. Liu, H. Huo, Y. Xiong, Effect of La0.8Sr0.2Co0.2Fe0.8O3-δ morphology on the performance of composite cathodes, Prog. Nat. Sci. Mater. Int. 24 (2014) 24–30. https://doi.org/10.1016/j.pnsc.2014.01.008.

[26] A. Enrico, W. Zhang, M. Lund Traulsen, E.M. Sala, P. Costamagna, P. Holtappels, La0.6Sr0.4Co0.2Fe0.8O3-δ nanofiber cathode for intermediate-temperature solid oxide fuel cells by water-based sol-gel electrospinning: Synthesis and electrochemical behaviour, J. Eur. Ceram. Soc. 38 (2018) 2677–2686. https://doi.org/10.1016/j.jeurceramsoc.2018.01.034.

[27] P. Costamagna, C. Sanna, A. Campodonico, E.M. Sala, R. Sažinas, P. Holtappels, Electrochemical Impedance Spectroscopy of Electrospun La0.6Sr0.4Co0.2Fe0.8O3–Δ Nanorod Cathodes for Intermediate Temperature – Solid Oxide Fuel Cells, Fuel Cells. 19 (2019) 472–483. https://doi.org/10.1002/fuce.201800205.

[28] A. Enrico, W. Zhang, M. Lund Traulsen, E.M. Sala, P. Costamagna, P. Holtappels, La0.6Sr0.4Co0.2Fe0.8O3-δ nanofiber cathode for intermediate-temperature solid oxide fuel cells by water-based sol-gel electrospinning: Synthesis and electrochemical behaviour, J. Eur. Ceram. Soc. 38 (2018) 2677–2686. https://doi.org/10.1016/j.jeurceramsoc.2018.01.034.

[29] P. Costamagna, E.M. Sala, W. Zhang, M. Lund Traulsen, P. Holtappels, Electrochemical impedance spectroscopy of La0.6Sr0.4Co0.2Fe0.8O3-δ nanofiber cathodes for intermediate temperature-solid oxide fuel cell applications: A case study for the ‘depressed’ or ‘fractal’ Gerischer element, Electrochim. Acta. 319 (2019) 657–671. https://doi.org/10.1016/j.electacta.2019.06.068.

[30] M. Sluyters-Rehbach, S.H. Sluyters, Electroanalytical Chemistry, A Series of Advances, Marcel Dekker, New York, 1970.

[31] E. Barsoukov, J.R. Macdonald, Impedance Spectroscopy: Theory, Experiment, and Applications, Second edi, John Wiley & Sons, Hoboken, New Jersey, 2005.

[32] M.E. Orazem, B. Tribollet, Electrochemical Impedance Spectroscopy, Second edi, John Wiley & Sons, Hoboken, New Jersey, 2017.

[33] C. Sanna, E. Squizzato, P. Costamagna, P. Holtappels, A. Glisenti, Electrochemical study of symmetrical intermediate temperature - solid oxide fuel cells based on La0.6Sr0.4MnO3 / Ce0.9Gd0.1O1.95 for operation in direct methane / air, Electrochim. Acta. 409 (2022) 139939. https://doi.org/10.1016/j.electacta.2022.139939.

[34] E. Perry Murray, S.A. Barnett, (La,Sr)MnO3-(Ce,Gd)O2-x composite cathodes for solid oxide fuel cells, Solid State Ionics. 143 (2001) 265–273. https://doi.org/10.1016/S0167-2738(01)00871-2.

[35] K. Chen, N. Ai, S.P. Jiang, Performance and structural stability of Gd0.2Ce 0.8O1.9 infiltrated La0.8Sr 0.2MnO3 nano-structured oxygen electrodes of solid oxide electrolysis cells, Int. J. Hydrogen Energy. 39 (2014) 10349–10358. https://doi.org/10.1016/j.ijhydene.2014.05.013.

[36] V. Yousefi, D. Mohebbi-kalhori, A. Samimi, Equivalent Electrical Circuit Modeling of Ceramic-Based Microbial Fuel Cells Using the Electrochemical Impedance Spectroscopy (EIS) Analysis, J. Renew. Energy Environ. 6 (2019) 21–28.

[37] C. Sanna, W. Zhang, P. Costamagna, P. Holtappels, Synthesis and electrochemical characterization of La0.6Sr0.4Co0.2Fe0.8O3–δ / Ce0.9Gd0.1O1.95 co-electrospun nanofiber cathodes for intermediate-temperature solid oxide fuel cells, Int. J. Hydrogen Energy. 46 (2021) 13818–13831. https://doi.org/10.1016/j.ijhydene.2020.11.216.

[38] Y. Chen, Y. Bu, Y. Zhang, R. Yan, D. Ding, B. Zhao, S. Yoo, D. Dang, R. Hu, C. Yang, M. Liu, A Highly Efficient and Robust Nanofiber Cathode for Solid Oxide Fuel Cells, Adv. Energy Mater. 7 (2017) 1–7. https://doi.org/10.1002/aenm.201601890.

[39] S. Koch, K. V. Hansen, B.S. Johansen, Elchemea, (2005).

ANNEX #1

"C. Sanna, W. Zhang, P. Costamagna, P. Holtappels, Synthesis and electrochemical characterization of La0.6Sr0.4Co0.2Fe0.8O3–δ / Ce0.9Gd0.1O1.95 co-electrospun nanofiber cathodes for intermediate-temperature solid oxide fuel cells, Int. J. Hydrogen Energy. 46 (2021) 13818–13831. https://doi.org/10.1016/j.ijhydene.2020.11.216. "

Available online at www.sciencedirect.com

ScienceDirect

journal homepage: www.elsevier.com/locate/he

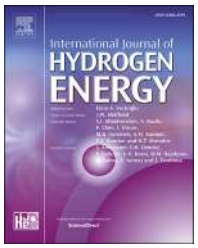

Synthesis and electrochemical characterization of $La_{0.6}Sr_{0.4}Co_{0.2}Fe_{0.8}O_{3-\delta}$ / $Ce_{0.9}Gd_{0.1}O_{1.95}$ co-electrospun nanofiber cathodes for intermediate-temperature solid oxide fuel cells

Caterina Sanna [a], *Wenjing Zhang* [b], *Paola Costamagna* [a,*], *Peter Holtappels* [c]

[a] *DCCI, Department of Chemistry and Industrial Chemistry, University of Genoa, Via Dodecaneso 31, Genoa, I-16146, Italy*

[b] *DTU Environment, Technical University of Denmark, Bygningstorvet, Building 115, DK-2800 Kgs. Lyngby, Denmark*

[c] *DTU Energy, Technical University of Denmark, Elektrovej 375, DK-2800 Kgs. Lyngby, Denmark*

HIGHLIGHTS

- LSCF/GDC electrospun nano-fiber cathodes for IT-SOFCs.
- New co-electrospinning technique.
- Electrochemical characterization through EIS.
- Percolation issues affect bimodal nanofiber electrodes.
- Polarization resistance $R_p = 5.6\ \Omega\ cm^2$ at T = 650 °C in air.

ARTICLE INFO

Article history:
Received 30 April 2020
Received in revised form
12 October 2020
Accepted 24 November 2020
Available online 23 December 2020

Keywords:
Electrochemical impedance spectroscopy (EIS)
Electrospinning
Mixed ionic electronic conductor (MIEC)
Percolation
Intermediate temperature-Solid oxide fuel cell

ABSTRACT

Synthesis and electrochemical characterization of composite cathodes, formed from a mixture of $La_{0.6}Sr_{0.4}Co_{0.2}Fe_{0.8}O_{3-\delta}$ (LSCF) and $Ce_{0.9}Gd_{0.1}O_{1.95}$ (GDC) nanofibers, is reported. The electrodes are obtained by simultaneous electrospinning of the two precursor solutions, using apparatus equipped with two spinnerets working in parallel. Results of electrochemical testing carried out through electrochemical impedance spectroscopy (EIS) are presented and discussed. The results suggest that the electrochemical reaction takes place in an electrode region close to the electrode/current collector interface and that the oxygen ions then flow along the ionic conducting path of the GDC fibers. At 650 °C, the polarization resistance is $R_p = 5.6\ \Omega\ cm^{-2}$, in line with literature values reported for other IT-SOFC cathodes.

* *Corresponding author.*
E-mail address: paola.costamagna@unige.it (P. Costamagna).

https://doi.org/10.1016/j.ijhydene.2020.11.216

Introduction

Intermediate temperature-solid oxide fuel cells (IT-SOFCs) are under development for operation in the temperature range of 600–800 °C. This working temperature, lower than that of high temperature-solid oxide fuel cells (HT-SOFC), is expected to mitigate degradation, reduce sealing problems, enable the use of inexpensive materials and improve response to rapid start-up. However, lowering the operating temperature also lowers fuel cell performance. For this reason, high-performance electrolytes and electrodes are currently under development, the latter often based on mixed ionic electronic conductors (MIECs). Among MIECs, perovskite oxides (ABO_3) are the most promising candidates for IT-SOFCs [1] and, among perovskites, $La_{1-x}Sr_xCo_{1-y}Fe_yO_{3-\delta}$ (LSCF) is the most investigated material thanks to its superior catalytic properties due to the oxygen reduction reaction (ORR) [2,3]. At a temperature of 650 °C, the electron conductivity of $La_{0.6}Sr_{0.4}Co_{0.2}Fe_{0.8}O_{3-\delta}$ is $\sigma_{el} \simeq 39.5\ 10^3$ S/m, and the oxygen ion conductivity is $\sigma_{io} \simeq 0.36$ S/m [4]. In this work, the $La_{0.6}Sr_{0.4}Co_{0.2}Fe_{0.8}O_{3-\delta}$ is the composition adopted for LSCF. In order to improve the electrode ionic conductivity, and also in order to extend the three-phase boundary (TPB) inside the electrode bulk, composite electrodes are investigated here, obtained by coupling LSCF with the oxygen ion conductor used for the electrolyte, i.e. $Ce_{0.9}Gd_{0.1}O_{1.95}$ (GDC). Throughout this work, the terminology 'electrode bulk' is used as opposed to 'electrode/electrolyte interface', the previous referring to the inside of the electrode thickness, and the latter being defined as the electrolyte surface on which the electrode adheres.

Another novelty of the present study is the electrode manufacturing technique, i.e. electrospinning. Electrospun 1-D materials like nanotubes, nanowires, nanorods and nanofibers are currently gaining significance due to their high surface area and mechanical properties [5–10]. The working principle of electrospinning is based on the electrostatic force that is created when a voltage difference is applied between the starting precursor solution, injected through a syringe, and the nanofiber collector. The process is sensitive to several solution and equipment parameters, such as voltage, solution flowrate, the distance between syringe tip and collector, syringe translation speed, collector rotation speed, environment temperature and humidity. Once the process parameters are set, the results are reproducible [11–14]. In our previous work, we developed an electrospun LSCF nanofiber electrode with 37.5% porosity, average nanofiber diameter 250 nm, and polarization resistance $R_p = 1.0\ \Omega\ cm^2$ at 650 °C [15]. The electrochemical impedance spectroscopy (EIS) Nyquist plots were interpreted as a combination of an RQ element, associated with the electrode/electrolyte interface, and of a pure Gerischer element, associated with the electrode bulk, which was demonstrated to account for the larger part of the polarization resistance [16]. Since the oxygen ion conduction through the electrode bulk appeared to be the rate-determining step of the overall phenomenon, the previous results suggested increasing the electrode ionic conductivity, which can be achieved by incorporating GDC into the electrode bulk. This is the same strategy applied to cermet and composite electrodes employed in the $(ZrO_2)_{1-x}(Y_2O_3)x$ (YSZ) based high-temperature SOFCs (HT-SOFCs). Indeed, in HT-SOFCs, Ni/YSZ anodes have been demonstrated to provide superior performance compared to pure Ni [17–20]. The same result was also obtained at the cathode side, where LSM/YSZ composites have substituted the previously adopted, pure LSM electrodes [21–24]. The importance of percolation in cermet and composite electrodes has been demonstrated on both theoretical and experimental bases [25–30]. The application of the same principle to the IT-SOFCs under consideration here, based on GDC electrolytes, leads to the addition of GDC into the electrode structure. In this respect, it has already been widely demonstrated in the literature, through experimental [31–33] and modeling [34] approaches, that LSCF fibrous electrodes infiltrated with GDC, demonstrate an increase in performance by increasing the level of infiltrations. This takes place even below percolation, i.e., without attaining continuous conduction paths for the oxygen ions through the electrode [34], the reason not yet being completely understood.

In this framework, the present work focuses on composite LSCF/GDC nanofiber electrodes manufactured through co-electrospinning, which is performed through electrospinning apparatus equipped with two spinnerets. Co-electrospinning allows the simultaneous ejection of two solutions, and the result is a tissue made of two types of nanofibers, which are expected to be randomly mixed throughout the tissue. The tissues are then applied on both sides of a GDC electrolyte disk, to obtain symmetrical cells, which are then tested in air, through EIS. The results are then compared to those obtained from single LSCF electrospun cathodes. The final aim is to enhance ionic conductivity and improve the performance of LSCF based cathodes, by employing an advanced microstructure.

Experimental

LSCF and GDC nanofiber preparation

Electrospinning employs two starting solutions, one for LSCF and one for GDC, containing the precursors of the metals involved. Metal nitrates are used as precursors: $Sr(NO_3)_2$ (Sigma-Aldrich 99.9%), $La(NO_3)_3 \cdot 6H_2O$ (Sigma-Aldrich 99.9%), $Fe(NO_3)_3 \cdot 9H_2O$ (Sigma-Aldrich 99.9%), $Co(NO_3)_2 \cdot 6H_2O$ (Sigma-Aldrich 99.9%), $Gd(NO_3)_3 \cdot 6H_2O$ (Sigma-Aldrich 99.9%), $Ce(NO_3)_3 \cdot 6H_2O$ (Sigma-Aldrich 99.999%). In the starting solutions, a carrier polymer is also present. For both solutions, polyvinylpyrrolidone (PVP, Mw = $1.3\ 10^6$ g/mol), supplied by Sigma-Aldrich, is used. The LSCF solution is obtained by the dissolution of the metal nitrates and PVP in de-ionized water. The molar ratios La:Sr and Co:Fe are 6:4 and 2:8 respectively. All the details about the component amounts are given in the Supplementary Information (SI),Table SI1 (a). Further details about the preparation of the LSCF solution are reported in Refs. [15,16].

The GDC starting solution is prepared by dissolving the metal nitrates in a solution 50/50% wt/wt water and ethanol.

The molar ratio Ce:Gd is 9:1. In parallel, PVP is dissolved in another solution 50/50% wt/wt de-ionized water and ethanol. The final GDC solution is obtained by mixing 50/50% vol/vol of the two previous solutions, followed by 24 h of milling, after which a clear and homogeneous solution is obtained. All the details about the component amounts are given in Table SI1 (b), whereas the details about the procedure for the preparation of the GDC starting solution are given in Table SI2.

The precursor solutions are fed into the electrospinning appliance, equipped with 2 spinnerets working in parallel (RT Advance, Linari Engineering, Pisa, Italy). The flow rate used is 0.3 mL/h for the LSCF solution and 1 mL/h for the GDC solution. The applied voltage is 3.3 kV/cm for the GDC solution and 4 kV/cm for the LSCF solution. During the electrospinning process, the relative humidity (RH) is 25%. Following the procedure described above, the overall volume of LSCF and GDC fibers in the final tissue is the same, i.e. the volumetric composition of the final tissue is 50% LSCF and 50% GDC.

The as-spun LSCF/GDC tissue then undergoes thermal treatment. The details of the heating ramp are reported in Table SI3. The heating rate between 350 °C and 500 °C is only 12 °C/h, because the decomposition of PVP occurs in this temperature range, releasing excessive gases. The low heating rate is therefore chosen to provide sufficient time for gas diffusion from inside the nanofiber to the surroundings. After thermal treatment, the LSCF nanofiber tissue is brought back to ambient temperature. The final area of the nanofiber tissue is 45% of that of the as-spun tissue, with uniform shrinkage in all directions. The final electrode diameter is 0.63 cm, and the final electrode area is 0.31 cm^2.

Symmetrical cell preparation

The GDC electrolyte is made by tape casting. The electrolyte is cut in a round shape through laser cutting, and then sintered with a maximum temperature of 1250 °C. After sintering, the diameter of the electrolytes is 1 cm, and the thickness is around 300 μm. The sintered LSCF/GDC electrodes are attached symmetrically onto the GDC electrolytes using a droplet of LSCF electrospinning solution as glue. This step ensures adhesion between the electrode and electrolyte. The symmetrical cells are placed into the sample holder of the test rig. The appliance has a four-sample set up, and each one is equipped with a gold mesh that acts as current collector. A thin layer of platinum is deposited onto the nanofiber electrodes to improve the contact between the meshes and the cell. Lastly, sintering of the symmetrical cells is carried out *in situ*, inside the electrochemical test rig, at 950 °C for 2 h.

Morphological and structural characterization

In order to investigate the nanofiber morphology, scanning electron microscopy (SEM) images are acquired, on the as-spun tissue and after thermal treatment. A Zeiss Ultra 55 microscope is used to obtain the SEM images, with different magnifications, depending on the specimen. The detector employed for the measurements is the SE2, and the acceleration voltage is in a range between 10 kV and 15 kV. A thin layer of gold, around 10 nm, is deposited by sputtering onto the specimen surface. The deposition is performed in a vacuum chamber, through the injection of argon. The ImageJ software, equipped with its plugin DiameterJ, is used to evaluate the nanofiber diameters from the SEM images. DiameterJ analyzes the images through a two-step procedure. Firstly, it performs image segmentation, producing a binary image (black and white pixels only). The second step is the analysis of the segmented image, computing the frequency corresponding to each fiber diameter. The porosity of the tissue is estimated through an analogous approach.

In order to investigate the composition of the individual nanofibers, SEM imaging is coupled with energy dispersive X-ray (EDX) measurements, carried out through a Brucker instrument. The measurements are performed using the QUANTX compact system, consisting of an XFlash® 600Mini Detector, with energy resolution for Mn Kα ≤12 450 kJ/mol, and a scanning control unit (SCU). The measurements are carried out at a working distance of 6.9 mm, with an accelerating voltage of 15 kV. X-ray diffraction (XRD) measurements are carried out through a Bruker D8 X-ray diffractometer (Bruker-Siemens, Germany), using Cu Kα radiation with an acceleration voltage of 40 kV and a filament current of 40 mA.

Electrochemical test set-up

Electrochemical characterization is carried out through electrochemical impedance spectroscopy (EIS). The cells are fixed between two gold meshes, which act as current collectors. In order to improve the interaction between the electrode and the current collector, a thin layer of platinum (Ferro GmbH, Germany) is deposited onto the top of the nanofiber electrodes. Four symmetrical cells are tested in parallel, thanks to the four-sample set-up rig employed for the test. The rig is placed and sealed inside a furnace, with controlled temperature. During the test, EIS measurements are carried out at 600°C, 650 °C, 700 °C, 750 °C, 800 °C, 850 °C, 900 °C and 950 °C. Throughout the test, the rig is fed with a gas flow, with composition 20% oxygen and 80% argon, at atmospheric pressure. The overall duration of the test is 120 h. On the first and the last test day, EIS measurements are performed at all the temperatures reported above. On the intermediate test days, the temperature is maintained at 800 °C, and one EIS test is carried out per day.

The EIS measurements are carried out through a Gamry Reference 600 potentiostat, in a frequency range $0.01 \div 10^6$ Hz with 10 mV of amplitude. Ten measurements per decade are performed. Before starting the test, a blank experiment is carried out, to measure the inductance of the experimental apparatus ($4.9\ 10^{-8}$ H), which is then subtracted from the raw impedance experimental data [16,35]. These data are then divided by 2 (since the raw impedance accounts for two identical electrodes) and multiplied by the electrode area (0.31 cm^2). In this way, the area-specific electrode impedance is obtained, expressed in Ω cm^2. In the range 0.01 Hz to $\div 10^5$ Hz the experimental error is <1%, but in the range between 10^5 Hz to 10^6 Hz the error increases, reaching values as high as 10% at 10^6 Hz [36].

Equivalent circuit-based EIS modeling

The equivalent circuit model used to fit the EIS experimental data is the same as proposed in a previous work [16]. It is an *Rs-RQ-G* series, composed of a resistor *Rs*, an *RQ* element and a Gerischer element *G*. The equivalent circuit also includes a serial inductance *L*, which is a residual inductance of the experimental apparatus [16,35]. *L* is evaluated through the fit, and the values obtained are in the order of ~1.0 10^{-8} H, and thus lower than the inductance of the experimental apparatus (4.9 10^{-8} H), which was determined in a separate experiment and subtracted prior to the fitting. In all the plots reported in this work, the results (both experimental and fits) are represented after subtraction of the residual inductance. For this reason, in the remaining part of the paper, the equivalent circuit employed is referred to simply as *Rs-RQ-G*, without including *L*.

Rs accounts for the overall ohmic resistance of the sample, including the electrolyte resistance, and, at each side of the symmetrical cell, contact and ohmic electrode resistance:

$$Rs = R_{electrolyte} + 2(R_{contact} + R_{electrode}) \quad (1)$$

The *RQ* element is a parallel between a resistor and a constant phase element (*CPE*), and is widely used to simulate electrode/electrolyte interfacial phenomena [37]. The resistor is associated with the charge transfer process, i.e., the oxygen reduction reaction (ORR). The *CPE* is related to the capacity Q of the electrode/electrolyte double layer. The equation representing the *RQ* impedance is:

$$Z_{RQ}(\omega) = \frac{1}{R_{RQ}^{-1} + Q(j\omega)^{\alpha}} \quad (2)$$

where α is a *CPE* parameter, independent of frequency. When $\alpha = 1$, the *CPE* coincides with the capacity Q of the electrode/electrolyte interface, with units (F). The representation of the *RQ* impedance in the Nyquist plot is a semi-circle. On the other hand, values $\alpha < 1$ are attributed to the heterogeneity of the electrode/electrolyte interface, or to continuously distributed time constants for the charge-transfer reactions [38]. The representation of the *RQ* impedance in the Nyquist plot is a depressed semi-circle. In these conditions, Q has units (F $s^{\alpha-1}$). An equivalent capacitance Q_{equiv}, with units (F), can be calculated according to the formula below:

$$Q_{equiv} = \frac{(QR)^{1/\alpha}}{R} \quad (3)$$

The Gerischer element *G* accounts for coupled charge transport and charge transfer reaction in the electrode bulk [39]. The representing equation is:

$$Z_G(\omega) = \frac{1}{Y_G(k + j\omega)^{0.5}} \quad (4)$$

where *k* is the oxygen surface exchange coefficient, whereas Y_G lumps together all the coefficients related to oxygen mass transport into the nanofiber electrodes via bulk or surface diffusion mechanisms, as well as structural parameters [35]. Eq. (4) above refers to the so-called 'pure' Gerischer and is characterized by the 0.5 exponent in the denominator.

In the EIS spectra of IT-SOFC electrodes tested at temperatures higher than ≃ 850 °C, an additional low-frequency arc appears [40]. It has been demonstrated that this is due to gas diffusion limitations [41], and that this additional arc is well fitted through a Finite-Length-Warburg (*FLW*) impedance [40,42]:

$$Z_{FLW}(\omega) = \frac{\tanh\left((Bj\omega)^{0.5}\right)}{(Y_{FLW}j\omega)^{0.5}} \quad (5)$$

where *B* and Y_{FLW} are phenomenological coefficients. In order to account for this additional process, for temperatures equal to or higher than 850 °C, the equivalent circuit model includes an additional *FLW* element in series, resulting in an *Rs-RQ-G-FLW* circuit.

Finally, the polarization resistance R_p is evaluated from the fittings as the difference between the low and high frequency intercepts of the Nyquist impedance spectra with the real axis.

Results and discussion

Morphological and structural characterization

SEM images of the as-spun composite nanofiber tissue are reported in Fig. 1(a and b), showing the structural and morphological characteristics of the LSCF/GDC raw nanofibers. The nanofibers are well entangled, with no detachments. Fig. 1(c and d) confirms that the fiber morphology is maintained after thermal treatment. Overall, Fig. 1 shows thinner non-transparent nanofibers mixed with larger transparent nanofibers, with ribbon features. ImageJ analysis of Fig. 1 is carried out, and details are reported in Figs. SI1 and SI2. The results are reported in Fig. 2, displaying the probability, or relative frequency, of fiber diameter falling in a certain diameter range. In particular, Fig. 2 (a) shows the results obtained for the as-spun nanofibers, from an averaged analysis of Fig. 1 (a) and of a companion SEM image, with the same magnification, taken from another point of the tissue. Fig. 2 (b) shows the results obtained for the thermally treated nanofibers, averaged analysis of Fig. 1 (d) and of a companion SEM image, with the same magnification, taken from another point of the tissue. The highest probability is around 0.41 μm for the as-spun nanofibers, and around 0.20 μm for the thermally treated nanofibers. This result, and a comparison between the frequency distributions reported in Fig. 2 (a) and (b), demonstrate that the thermal treatment causes a ≃50% reduction of the diameter size.

A 2D analysis of the porosity is carried out through the ImageJ software. Details of the procedure are given in Fig. SI3. The result is that the void degree is $\varepsilon = 0.34$, for both the as-spun tissue and for the heat-treated tissue. An important remark is that the estimation of porosity through an analysis of 2D images underestimates the void degree. Indeed, 2D SEM images display the nanofibers as if they were laying perfectly in plane, which is not completely true; however, the real orientation of the nanofibers cannot be inferred from the available 2D SEM images. In the literature, it is reported that, in case of random packings of spheres, there is a correlation between the pore size reported in 2D and 3D. In particular, the chords of the 2D and 3D pores are in a 1:1 ratio [43,44]. Nanofiber electrodes may exhibit a somehow different behavior. Nevertheless, considering the approach mentioned

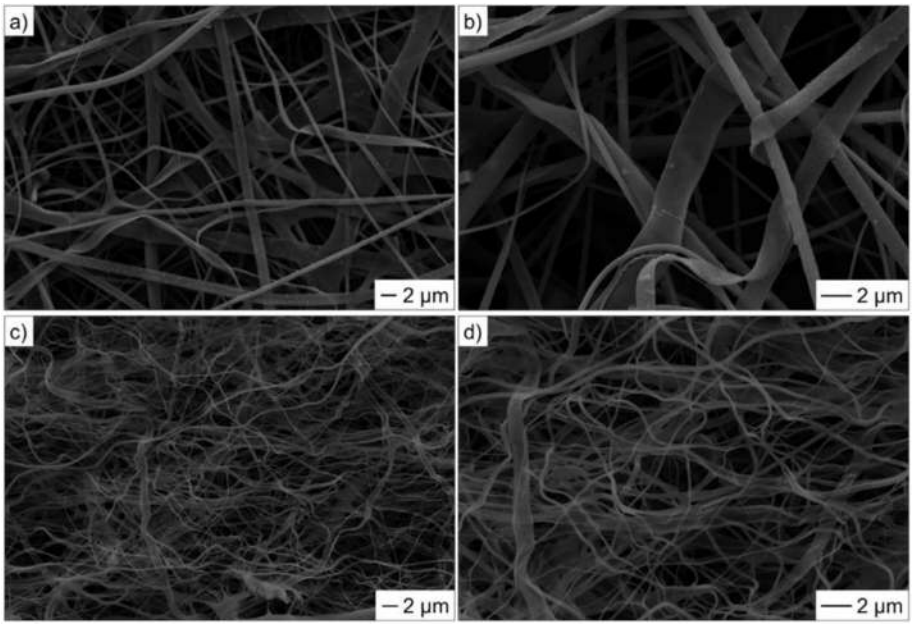

Fig. 1 – SEM pictures of LSCF/GDC co-electrospun nanofibers: a) and b) as-electrospun tissue; c) and d) after thermal treatment.

above, originally developed for random packings of spheres [43,44], and applying it to nanofibers, then the 3D void degree is 45% for the raw nanofibers and 50% for the heat-treated nanofibers. Details of the calculation procedure for the void degree estimation are reported in Table SI4. The fact that the 3D void degree is 5% different before and after heat treatment, agrees well with the result reported above, that the shrinkage of the single fibers during heat treatment is 50%, exactly 5% higher than the shrinkage of the overall tissue (45%).

XRD characterization of the LSCF/GDC heat-treated tissue is also performed, and the results are reported in Fig. 3. The experimental pattern contains all the peacks of the LSCF and GDC references, which confirm that crystallinity is achieved for both LSCF and GDC.

EDX measurements are performed on the LSCF/GDC thermally treated tissue, in order to understand the composition of the individual nanofibers (Fig. SI4). The measurements are carried out pointing at one individual nanofiber at a time, and acquiring its composition. Lanthanum is the main metal found in thick nanofibers, suggesting that they are made of LSCF. Conversely, cerium is the main metal found in thin nanofibers, suggesting that they are made of GDC. The reason why the LSCF nanofibers have a larger diameter compared to the GDC nanofibers, is assumed to be due to the differences in the starting solutions used for electrospinning. In particular, PVP is 10 wt% of the entire LSCF starting solution, whereas PVP is only 7 wt% in the GDC starting solution. This causes a higher viscosity for the previous solution, which results in a larger nanofiber diameter in the electrospinning process [45–47].

Electrochemical characterization

Rs Analysis

In the Nyquist representation of the inductance-free EIS experimental arcs, the high-frequency intercept with the real axis is *Rs*. Fig. 4 reports a plot of the *Rs* obtained from symmetrical cells with co-electrospun LSCF/GDC fiber electrodes, displaying a value of $Rs = 6.8\ \Omega\ cm^2$ at 650 °C. For comparison,

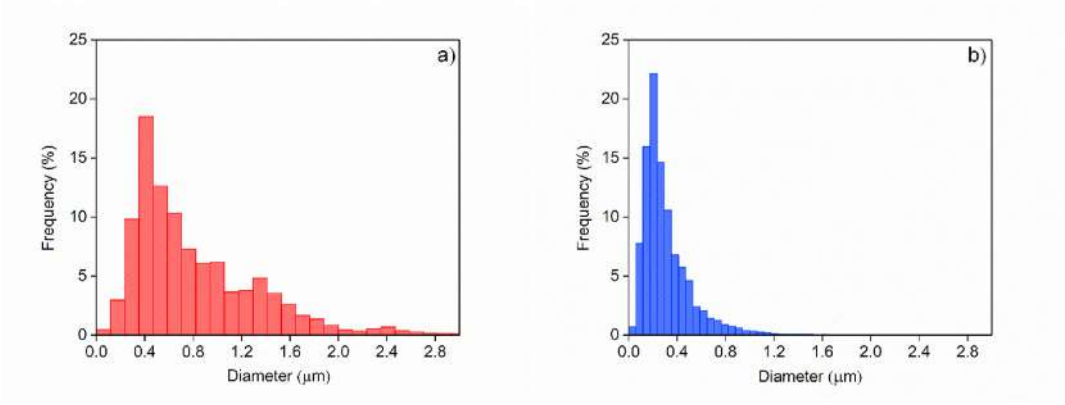

Fig. 2 – ImageJ analysis of LSCF/GDC nanofibers (a) before and (b) after thermal treatment.

the values of *Rs* obtained from previously tested symmetrical cells with LSCF fiber electrodes [15,16,35] are also reported, showing values up to tenfold lower in the temperature range investigated. It is underlined here that, as shown in Fig. 4, the symmetrical cells with LSCF nanofiber cathodes [15,16] and with LSCF nanorod cathodes [35,48] display practically identical *Rs*, even though obtained from symmetrical cells manufactured in different laboratories and with different geometrical arrangement of the nanofibers within the electrode. Thus, the reproducibility of *Rs* is very high, when pure LSCF fibers are considered.

Regarding Fig. 4, another remark is about the non-linear behavior of the *Rs* of symmetrical cells with pure LSCF fiber electrodes, as a function of 1000/T. Indeed, *Rs* embeds the electrolyte resistance. Since the electrolyte is GDC in all cases, the ionic conductivity follows the equation below [49]:

$$\sigma T = C \cdot \exp\left(-\frac{E_a}{R_{gas}T}\right) \quad (6)$$

In [49], the following values are proposed for the pre-exponential term C and the activation energy E_a respectively: $C = 1.81\ 10^5$ S K/cm, and $E_a = 70.4$ kJ/mol. On the basis of this equation, the plot of $R = \sigma^{-1}$ vs. 1000/T, displays a slight deviation from linearity. Moreover, as already remarked, *Rs*, in addition to the electrolyte contribution, also includes the electrode contributions. For symmetrical cells, these are two identical contributions, including the contact resistance between the various layers $R_{contact}$, and the ohmic resistance of the electrode $R_{electrode}$. Usually, $R_{electrode}$ is negligible, due to the high conductivity of the electrode materials. Regarding $R_{contact}$, usually this is constant with temperature. If the contact resistance is non-negligible compared to the electrolyte resistance, then it causes the overall *Rs* to deviate significantly from linearity. In Fig. 4, this is clearly the situation occurring with the LSCF nanorod and nanofiber cathodes. The fitting equation below is clearly derived from Eq. (6):

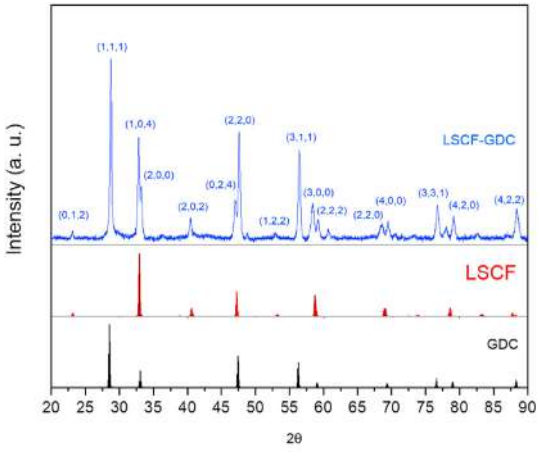

Fig. 3 – XRD of the LSCF/GDC co-electrospun tissue, after thermal treatment (blue). LSCF (red) and GDC (black) reference patterns are reported as well. Crystallographic plane indexes are provided. (For interpretation of the references to color in this Figure legend, the reader is referred to the Web version of this article.)

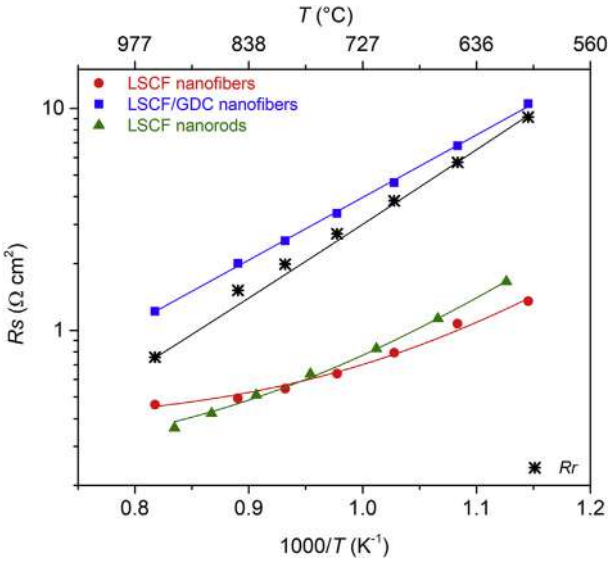

Fig. 4 – Symbols in color: serial resistance *Rs*, from equivalent circuit modeling of EIS experimental data. Black asterisks: *Rr*, obtained as the *Rs* of LSCF/GDC nanofiber cathodes (blue squares) minus the *Rs* of LSCF nanofiber cathodes (red circles). Continuous lines: least squares fittings. (For interpretation of the references to colour in this figure legend, the reader is referred to the Web version of this article.)

$$Rs = \frac{A}{x}exp(Bx) + 2R_{contact} \quad (7)$$

where $x = 1000/T$. The fittings are reported in Fig. 4, and the contact resistance is $R_{contact} = 0.12\ \Omega\ cm^2$ for the LSCF nanorod cathodes, and 0.19 Ω cm^2 for the LSCF nanofiber cathodes. Thus, in both cases these contact resistances become significant, compared to the electrolyte resistance contribution, for $1000/T < 1\ K^{-1}$, i.e., temperatures above 1000 K. This is the region where the non-linearity appears in the Figure.

Fig. 4 also displays the residual resistance *Rr* calculated by subtracting the *Rs* of the cells with LSCF nanofiber cathodes [15,16] from that of the cells with LSCF/GDC co-electrospun nanofiber cathodes investigated in this work. Here, it is assumed that this residual resistance *Rr* is an electrode resistance $R_{electrode}$, associated with the ionic resistance of the GDC fibers in the electrode. Thus, *Rr* is fitted through the equation below, derived from Eq. (6):

$$Rr = 2R_{electrode} = 2\alpha\frac{T}{C}\cdot\exp\left(\frac{E_a}{R_{gas}T}\right)\frac{l}{S}\frac{\tau}{(1-\varepsilon)} \quad (8)$$

where *l* is the electrode thickness, *S* is the electrode area, α is the volumetric ratio of GDC fibers versus overall fibers, τ the fibers tortuosity, ε the electrode void degree and finally the multiplying coefficient 2 accounts for the presence of 2 identical electrodes in the symmetrical cell. The electrode thickness, estimated through SEM images, is $l = 40$ μm, and the electrode area is $S = 0.31\ cm^2$. Overall, the same volume is occupied by GDC and LSCF nanofibers in the electrode (Table SI5), so that $\alpha = 0.5$. The parameters τ and ε are lumped together as follows:

$$\Psi = \frac{\tau}{(1-\varepsilon)} \quad (9)$$

where Ψ is treated as the only fitting parameter. Fig. 4 shows that the least squares fitting of the residual resistance *Rr* through equation Eq. (8) is very satisfactory (goodness of fit: reduced chi-squared $\chi^2_\nu = 0.027$, coefficient of determination $R^2_d = 0.997$). The fitting makes it possible to evaluate Ψ. The value obtained is $\Psi = 8.53$, which is consistent with $\varepsilon = 0.34$ and $\tau = 5.6$, or $\varepsilon = 0.5$ and $\tau = 4.3$.

The results obtained are consistent with a picture of the overall phenomenon as represented in Fig. 5: the electrons, after being injected into the LSCF fibers of the electrode through the current collector, undergo charge transfer reaction in a very thin electrode layer (electrochemically active thickness, EAT) adjacent to the current collector. Then, the oxygen ions formed flow along the GDC fibers towards the GDC electrolyte. In the nanofiber electrode, the fibers lay almost in plane with the electrolyte, with a limited number of contact points between each other. Thus, the oxygen ions must travel a long way in plane along a fiber, before a contact point with a nearby fiber is found. At this point, a short transfer is performed in the cross-plane direction, followed by another in-plane path. This is consistent with the unusually high values of tortuosity τ reported above (4.3 ÷ 5.6).

Overall, this picture is different from typical electrode behavior. Usually, as discussed in Refs. [15,35] and also in other previous papers [40] in the literature, the situation is different, with the electrons moving though the electrode thickness along the highly electron-conducting LSCF phase, and then being transferred to the poorly ion-conducting GDC phase at just a short distance from the electrolyte. In the latter picture, thus, the EAT where the charge transfer reaction takes place is adjacent to the electrolyte. The reason for the relocation of the EAT from being adjacent to the electrolyte (LSCF nanofiber electrode), to being adjacent to the current collector (LSCF/GDC co-electrospun nanofiber electrode), can only be explained by some difficulties encountered in the latter case by the electrons in penetrating the electrode structure. The main explanation proposed here is a lack of percolation among LSCF nanofibers. Indeed, as discussed in the previous sections, the LSCF nanofibers are thicker than those of GDC. Even if no literature data are reported about percolation in bimodal fibrous structures, previous studies [26] demonstrate that, in electrodes composed of bimodal spherical particles, percolation among the larger spheres is hindered. The same situation may occur with fibers, with the larger LSCF fibers being farther away from each other, and thus not percolating, in the three-dimensional bimodal fiber network. These considerations may justify the poor percolation of the LSCF nanofibers. Another alternative or overlapping phenomenon may be a non-uniform distribution of the fibers, with a larger concentration of the LSCF fibers close to the current collector, and a larger concentration of the GDC fibers close to the electrolyte. The SEM images shown in Section 4.1, together with the image analysis carried out though the DiameterJ software, support the previous explanation (lack of percolation), demonstrating that LSCF fibers have a diameter which is almost double that of GDC fibers. Conversely, the SEM pictures do not give any indication about a possible non-uniform distribution of GDC and LSCF fibers in the electrode.

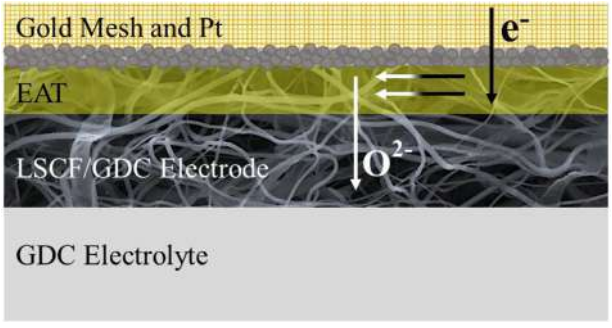

Fig. 5 – Schematic representation of the LSCF/GDC co-electrospun nanofiber electrode. The electrochemical active thickness (EAT), is the portion of the electrode where the charge transfer reaction takes place.

EIS results

Fig. 6 reports the Nyquist and Bode plots of the EIS experimental results obtained for temperatures between 600 °C and 800 °C, together with fittings performed through the *Rs-RQ-G* equivalent circuit model. For temperatures equal to or higher than 850 °C, the EIS experimental results are reported in Fig. 7, and the corresponding equivalent circuit model includes an additional *FLW* element in series, resulting in an *Rs-RQ-G-FLW* circuit. Fig. 6 shows that, at 600°C–700 °C, the Nyquist plot shows a typical Gerischer shape, and in parallel the Bode plot shows that the *RQ* process gives only a minor contribution. By increasing the temperature to 800 °C, the relative importance of the *RQ* process increases, and the *RQ* and *G* elements tend to give comparable contributions in the same frequency domain. As a consequence, the arc in the Nyquist plot shrinks and reshapes, losing the typical Gerischer shape, and taking a form often referred to as 'depressed' or 'fractal' Gerischer. In previous works, it was demonstrated that this shape is a hybrid between *RQ* and Gerischer [16,35]. The bode plots in Figs. 6 and 7 also demonstrate that, by increasing temperature, the maximum impedance of the *RQ* and *G* elements shift towards higher frequencies, which means that the associated time constants decrease. Finally, in the range of 850 °C–950 °C (Fig. 7), the shrinkage of the main impedance in the Nyquist plot, reveals an additional low-frequency arc, whose size is practically independent of temperature. This is associated with an additional peak becoming visible in the Bode plots. Coherently with previous works [16,35], this is interpreted here in terms of gas diffusion resistance [50]. Overall, Figs. 6 and 7 confirm that the proposed equivalent circuit models *Rs-RQ-G* and *Rs-RQ-G-FLW* provide very accurate fitting. Here, the fitting error varies between 0.1% (at 800 °C) and 0.05% (at 950 °C). The behavior in Figs. 6 and 7 is qualitatively analogous to that reported in Refs. [16,35]; nevertheless, the polarization obtained is larger. For example, at 650 °C the polarization resistance is $R_p = 5.6\ \Omega\ cm^2$, whereas $R_p = 1\ \Omega\ cm^2$ with single LSCF nanofiber electrodes [15].

Fig. 8 presents an Arrhenius plot of the $1/R_p$ of the LSCF/GDC nanofiber electrode, compared to that of single LSCF nanofibers investigated in previous work [15,16]. In both cases, the breakdown of the overall $1/R_p$ into the contributions related to the *RQ* and *G* elements is reported. As already

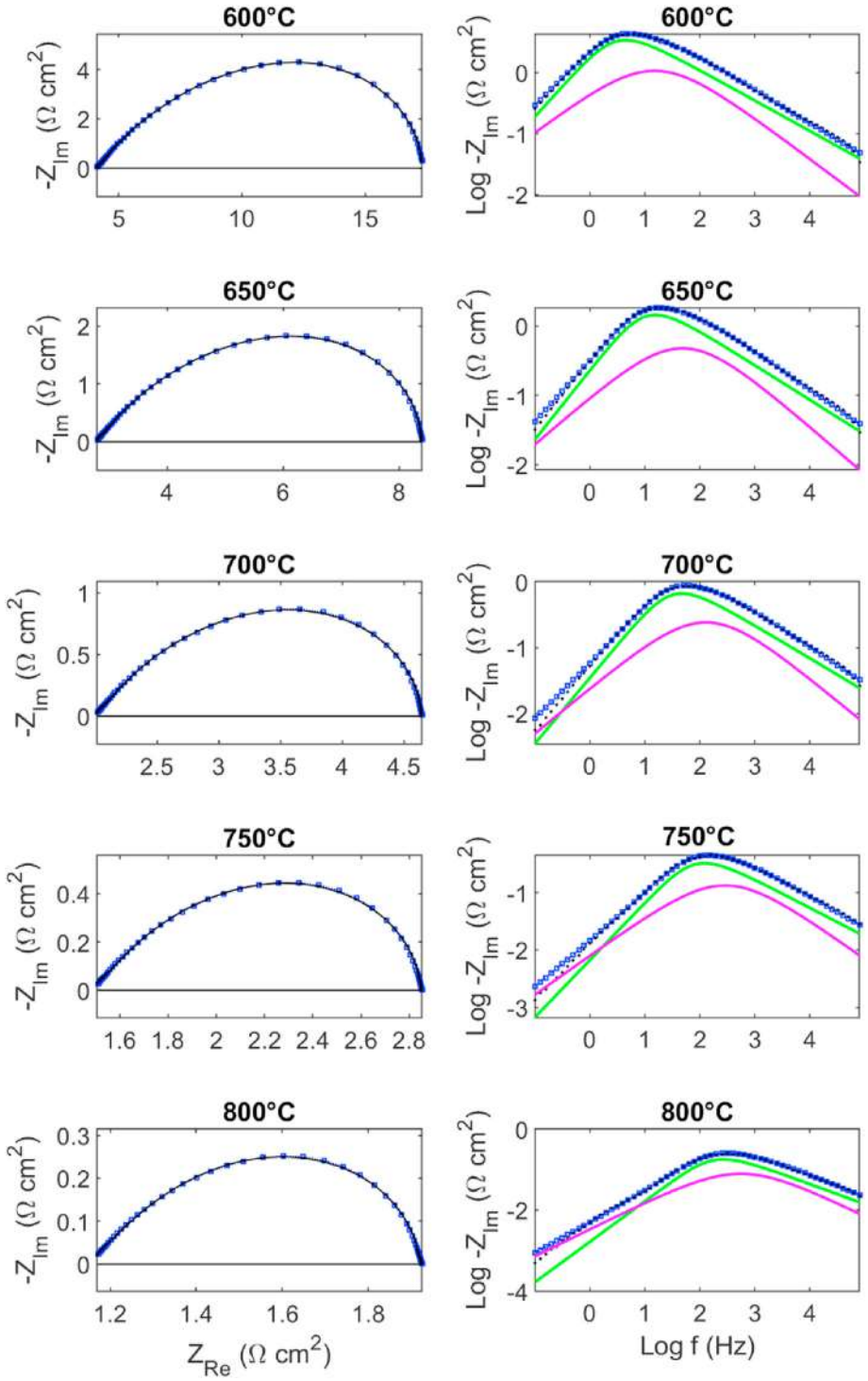

Fig. 6 – Nyquist (left) and Bode (right) plots of the EIS results at operating temperatures from 600 °C to 800 °C: experimental data (black circles); fitting through the Rs-RQ-G equivalent circuit model (blue squares); Gerischer contribution (green lines); and RQ contribution (magenta lines). (For interpretation of the references to colour in this figure legend, the reader is referred to the Web version of this article.)

displayed in the Bode plots reported in Fig. 6, the main contribution to the overall polarization resistance is given by the G element, with the RQ contribution being less impacting. This occurs with both the LSCF/GDC nanofiber electrode and the single LSCF nanofibers. Fig. 9 shows that the $1/R_p$ contribution associated with the RQ element is lower in the LSCF/GDC nanofiber electrode, rather than in the single LSCF nanofiber electrode. This suggests that the interface represented by the RQ element is less electrochemically active in the previous electrode. This is probably because the interface

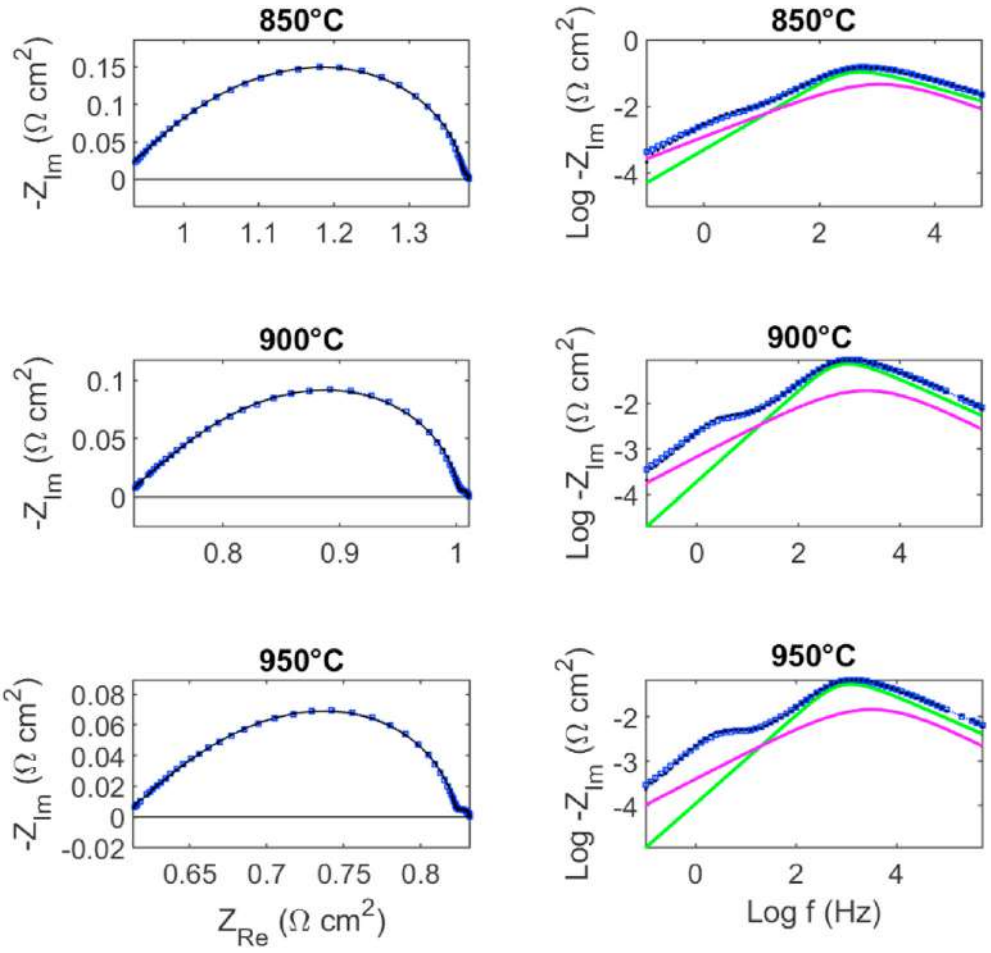

Fig. 7 – Nyquist (left) and Bode (right) plots of the EIS results at operating temperatures from 850 °C to 950 °C: experimental data (black circles); fitting through the *Rs-RQ-G-FLW* equivalent circuit model (blue squares); Gerischer contribution (green lines); and *RQ* contribution (magenta lines). (For interpretation of the references to colour in this figure legend, the reader is referred to the Web version of this article.)

represented by the *RQ* element is between the LSCF/GDC electrode and the current collector. As mentioned before, the current collector is a gold mesh coupled with a thin layer of platinum particles deposited onto the surface of the nanofiber electrodes. Therefore, due to the small number of contact points between the electrode and current collector, and due to the materials employed, the electrochemical activity and thus the $1/R_p$ are lower. Furthermore, Fig. 8 shows that the $1/R_{p,G}$ associated with the *G* element, is also lower in the LSCF/GDC nanofiber electrode, rather than in the single LSCF nanofiber electrode. The *G* element represents the charge transfer with simultaneous electrochemical reaction in the electrode bulk and, in this work, it signifies the intrinsic electrochemical activity of the synthesized LSCF/GDC. In the LSCF/GDC electrode, considering that half of the fiber volume is GDC and does not contribute to the electrochemical reaction, a value of $1/R_{p,G}$ half of that obtained from the LSCF nanofiber electrode may be expected. Instead, Fig. 8 shows that a lower performance is obtained from the LSCF/GDC electrode, about one quarter of that of the LSCF electrode. The reason could be due to a number of reasons, including the non-linearity of the process and a smaller thickness of the EAT with the LSCF/GDC electrode.

Fig. 9 reports the values obtained for the fitting parameters of the equivalent circuit model used to fit the EIS experimental data obtained from the LSCF/GDC nanofiber electrode. The results are discussed with reference to those obtained from pure LSCF nanofiber electrodes, reported and discussed in previous papers [16,35]. Fig. 9 a) reports the values obtained for the *CPE* exponent α. The values are quite constant in the range 0.67 ÷ 0.68, for temperatures of 600 ÷ 850 °C. α drops to 0.58 ÷ 0.59 in the temperature range 900–950 °C. Considering that, usually, α is in the range 0.8 ÷ 1, the values reported appear rather low. The value of α is associated with the broadness of the distribution of the charge transfer phenomenon across the interface thickness, in the sense that $\alpha = 1$ is related to an ideal capacitor (no distribution), and $\alpha < 1$ is associated with a distributed phenomenon (the broader the distribution, the lower the value of α). Therefore, the low value of α identified in the present case is consistent with a highly

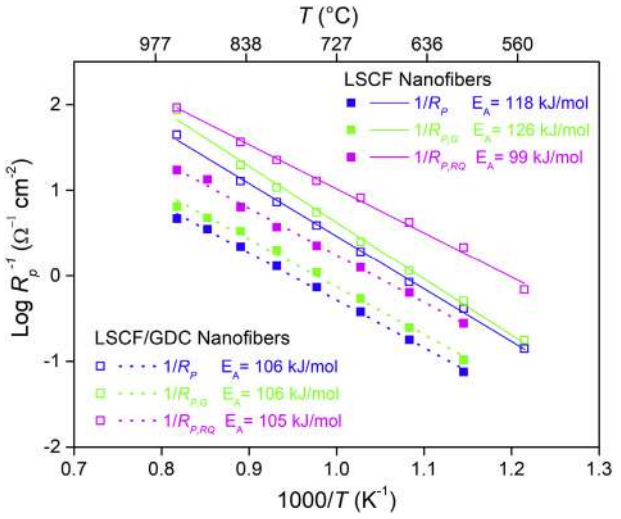

Fig. 8 – Arrhenius plot of $1/R_p$. Solid symbols ■ represent the LSCF/GDC nanofiber electrode, open symbols □ represent the pure LSCF nanofiber electrode [15,16]. Blue: $1/R_p$; green: Gerischer contribution $1/R_{p,G}$; and magenta: RQ contribution $1/R_{p,RQ}$. Arrhenius line fittings are also shown. (For interpretation of the references to colour in this figure legend, the reader is referred to the Web version of this article.)

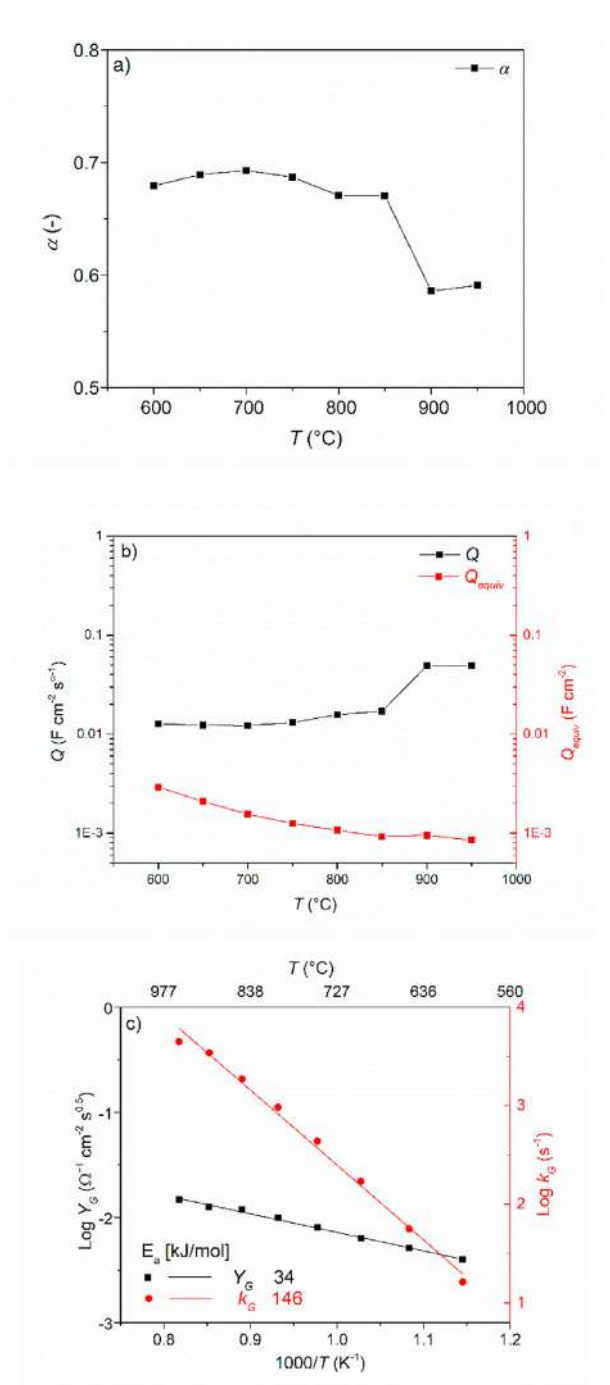

Fig. 9 – Fitting parameters of the equivalent circuit model used to fit the EIS experimental data obtained from the LSCF/GDC nanofiber electrode: a) α, b) Q and Q_{equiv}; and c) Y_G and k_G, with Arrhenius line fittings.

distributed process at the nanoscale (nm) of the fiber/current collector interface, which, from the geometrical point of view, is non-uniform. The values identified here are consistent with those obtained in previous studies on pure LSCF electrospun cathodes [16,35]. Fig. 9 b) shows the values of the area-specific capacitance Q (F cm^{-2} $s^{\alpha-1}$) and area-specific equivalent capacitance Q_{equiv} (F cm^{-2}), evaluated through Eq. (3). For the capacitances, the values identified here are in the range of pseudo-capacitances, and are consistent, although slightly lower, than those obtained in previous studies on single LSCF electrospun cathodes [16,35]. This is in agreement with the previous discussion about $1/R_{p,RQ}$, that the interface represented by the RQ element is less active with the co-electrospun LSCF/GDC nanofiber electrode rather than with the pure LSCF nanofiber electrode. Finally, Fig. 9 c) reports the Arrhenius plots of the parameters Y_G and k_G of the Gerischer circuit element. Interestingly, the values of the oxygen surface exchange coefficient k_G are similar to those obtained for the pure LSCF electrode. The activation energies are 146 kJ/mol and 120 kJ/mol for the LSCF/GDC and for the pure LSCF electrode respectively, corresponding to a variation of about 22% for LSCF/GDC compared to the pure LSCF electrode. These results are consistent with a picture where the mechanism of the oxygen surface exchange is somehow similar in the LSCF/GDC and in the pure LSCF electrode. This suggests that, in the LSCF/GDC electrode, the electrochemical reaction occurs at the contact between LSCF and GDC fibers, or along the LSCF fibers with a subsequent transfer of the oxygen ions to the GDC fibers. In contrast, the Y_G parameter, related to oxygen mass transport along the fibers via bulk or surface diffusion mechanisms, as well as structural parameters, displays very different values for the LSCF/GDC and for the pure LSCF electrode. The activation energies are 34 kJ/mol and 66 kJ/mol for the LSCF/GDC and for the pure LSCF electrode respectively, corresponding to a variation of about 48% for LSCF/GDC compared to the pure LSCF electrode. Interestingly, it is reported in the literature that the activation energy of oxygen

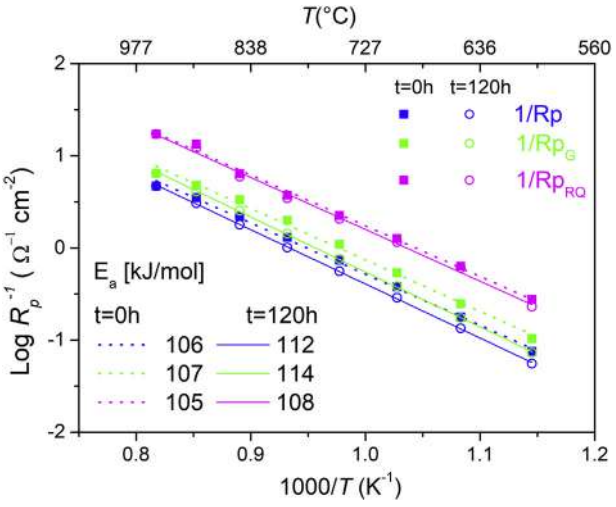

Fig. 10 – Arrhenius plot of $1/R_p$ of the LSCF/GDC nanofiber electrode at the beginning and at the end of the electrochemical test. Solid symbols represent the beginning of the experimentation, open symbols represent end of test results. Arrhenius line fittings are also shown.

vacancy transport is 70 kJ/mol for GDC [49], and 186 kJ/mol [51] for LSCF. These data compare well with the results reported above for the activation energies of Y_G, and are consistent with a picture of the LSCF/GDC electrode where the oxygen ions flow on the GDC fibers, whereas in the pure LSCF fiber electrode, oxygen ion conduction occurs along the LSCF fibers.

Aging

Fig. 10 shows the Arrhenius plot of $1/R_p$ of the LSCF/GDC nanofiber electrode, at the beginning of the experiment (t = 0 h) and at the end of test (t = 120 h). As far as the RQ element is concerned, no significant performance decay is observed, confirming analogous results to those previously obtained from single LSCF nanofiber electrodes [16]. Even though the nature of the interface represented by the RQ element is different, nevertheless slow degradation is found in both cases. Instead, Fig. 10 shows that the $1/R_{p,G}$ of the G element degrades over time. This degradation of performance of the G element was already observed with single LSCF nanofiber electrodes [16], but with one remarkable difference. The decay, in the latter case, was mainly associated with a decrease of activation energy, whereas here, with a LSCF/GDC nanofiber electrode, it is mainly associated with a downward shift of the Arrhenius plot of $1/R_{p,G}$, with a slight

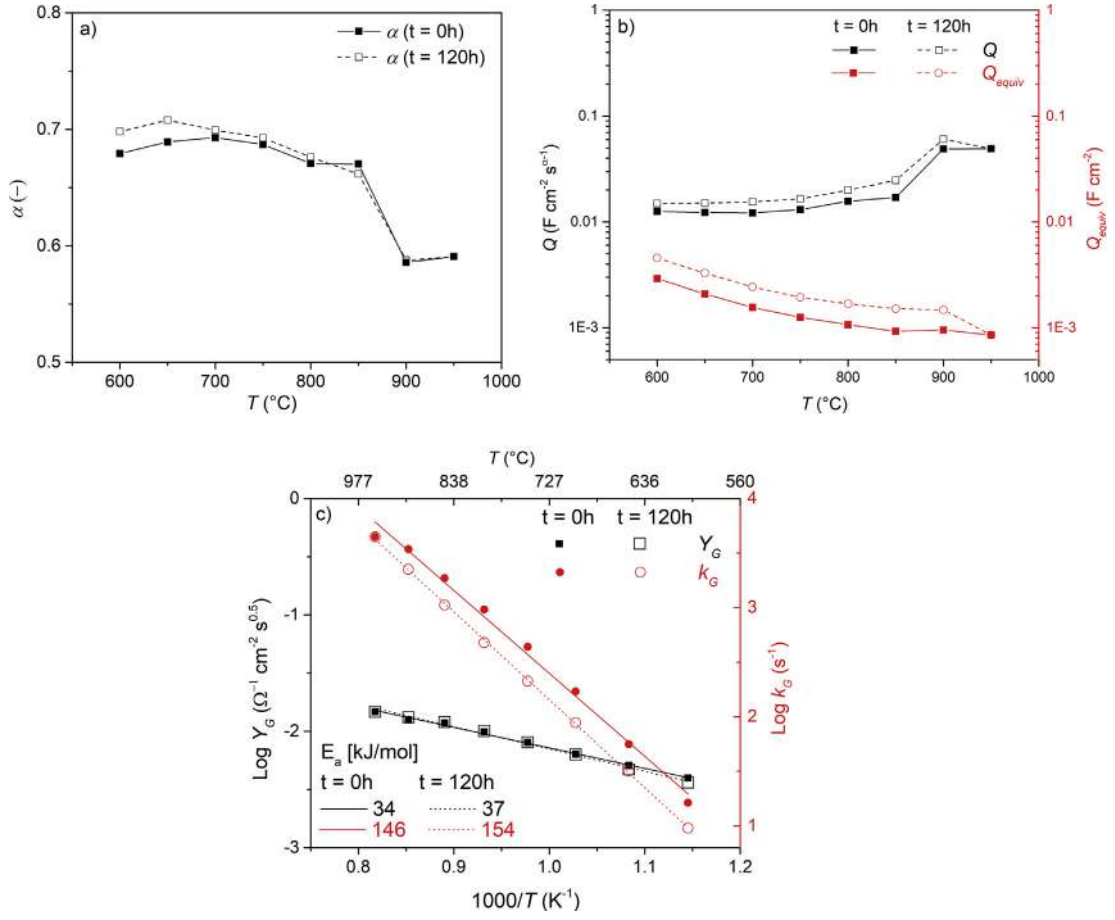

Fig. 11 – Fitting parameters of the equivalent circuit model used to fit the EIS experimental data obtained from the LSCF/GDC nanofiber electrode. Results at the beginning and at the end of the electrochemical test: a) α, b) Q and Q_{equiv}); and c) Y_G and k_G, with Arrhenius line fittings.

increase of the activation energy from 106.8 kJ/mol to 114.1 kJ/mol.

For a more detailed investigation, the fitting parameters of the equivalent circuit model are reported in Fig. 11. Fig. 11a and b) demonstrate that all the RQ parameters α, Q and Q_{equiv} do not vary remarkably over time, which is in agreement with $1/R_{p,RQ}$ being substantially unchanged during the 120 h of investigation. Fig. 11 c) shows that the parameter Y_G does not vary during time, suggesting that the features of the oxygen mass transport along the fibers via bulk or surface diffusion mechanisms, as well as structural parameters, do not vary appreciably during the testing time. The same result was found previously with pure LSCF electrodes [16]. Regarding the oxygen surface exchange coefficient k_G, Fig. 11 c) shows a downward shift associated with a slight increase in activation energy. This is consistent with the behavior of $1/R_{p,G}$ reported in Fig. 10, and suggests that, over time, the main phenomenon is a decrease in the number of active reaction sites, which may be the result of a reduction of the number of contact points between LSCF and GDC fibers in the electrode. Instead, in the electrode formed by pure LSCF fibers, the main phenomenon observed was a change in slope of the Arrhenius plot of $1/R_{p,G}$, indicating a deterioration the electrochemical kinetics along the fibers over time [16].

Conclusions

In this work, a composite LSCF/GDC electrospun nanofiber cathode is investigated experimentally through EIS. The EIS experimental data are fitted through an *Rs-RQ-G-FLW* equivalent circuit model, demonstrating very low fitting error (0.1% at 800 °C and 0.05% at 950 °C). The high values obtained for the serial ohmic resistance *Rs* are explained in terms of a lack of percolation through the LSCF fibers throughout the electrode. This is attributed to the fact that the LSCF and GDC nanofibers do not have the same dimensions, with LSCF nanofibers being larger than those of GDC. As a consequence, only the GDC nanofibers percolate through the electrode, whereas percolation is hindered for the LSCF nanofibers, which exhibit larger size. This lack of percolation for the LSCF nanofibers results in a lack of electronic conduction through the electrode, which forces the electrochemical reaction to take place in the outer part of the electrode, at the interface with the current collector. The oxygen ions resulting from the electrochemical reaction are then transferred to the electrolyte through the percolating high-resistance ionic conduction path. This picture of the electrode functioning explains the high value obtained for *Rs*, and also the high value obtained for R_p. At 650 °C, R_p = 5.6 Ω cm^2, which means that 5–6 times higher electrode resistances are obtained for composite LSCF/GDC fibers, compared to electrospun pure LSCF fibers experimented in a previous work. The LSCF/GDC nanofiber cathode shows reasonable stability during the electrochemical tests, with a 22% increase of the polarization resistance during 120 h of experimentation. A detailed analysis of the parameters of the *Rs-RQ-G-FLW* equivalent circuit model suggests that the source of degradation could be associated with a reduction in the number of contact points between LSCF and GDC fibers in the electrode over time.

To conclude, percolation issues affect not only state-of-the-art bimodal granular electrodes, but also bimodal nanofiber electrodes. Percolation is expected to be very different with fibers laying in plane or randomly distributed in 3-D (for example, nanorods).

Declaration of competing interest

The authors declare that they have no known competing financial interests or personal relationships that could have appeared to influence the work reported in this paper.

Acknowledgments

C.S. gratefully acknowledges the group at DTU for kind hospitality and supervision during Erasmus+.

Appendix A. Supplementary data

Supplementary data to this article can be found online at https://doi.org/10.1016/j.ijhydene.2020.11.216.

REFERENCES

[1] Riess I. Mixed ionic-electronic conductors - material properties and applications. Solid State Ionics 2003;157:1–17. https://doi.org/10.1016/S0167-2738(02)00182-0.

[2] Jiang SP. Development of lanthanum strontium cobalt ferrite perovskite electrodes of solid oxide fuel cells – a review. Int J Hydrogen Energy 2019;44:7448–93. https://doi.org/10.1016/j.ijhydene.2019.01.212.

[3] Zhang W. Electrospinning for solid oxide fuel cells. Electrospinning adv. Energy environ. Appl.. 2015. p. 61–76. https://doi.org/10.1201/b18838.

[4] Huang D, Xu Q, Zhang F, Chen W, Liu H, Zhou J. Structure and mixed electronic-ionic conducting properties of $La_{0.6}Sr_{0.4}Co_{1-y}$ Fe_yO_3(y=0-1.0) ceramics made by a citrate method. J Wuhan Univ Technol -Mater Sci Ed 2008;23:80–4. https://doi.org/10.1007/s11595-006-1080-3.

[5] Greiner A, Wendorff JH. Electrospinning: a fascinating method for the preparation of ultrathin fibers. Angew Chem Int Ed 2007;46:5670–703. https://doi.org/10.1002/anie.200604646.

[6] Rauf M, Wang JW, Zhang P, Iqbal W, Qu J, Li Y. Non-precious nanostructured materials by electrospinning and their applications for oxygen reduction in polymer electrolyte membrane fuel cells. J Power Sources 2018;408:17–27. https://doi.org/10.1016/j.jpowsour.2018.10.074.

[7] Aruchamy K, Mahto A, Nataraj SK. Electrospun nanofibers, nanocomposites and characterization of art: insight on establishing fibers as product. Nano-Structures and Nano-Objects 2018;16:45–58. https://doi.org/10.1016/j.nanoso.2018.03.013.

[8] Frenot A, Chronakis IS. Polymer nanofibers assembled by electrospinning. Curr Opin Colloid Interface Sci 2003;8:64–75. https://doi.org/10.1016/S1359-0294.

[9] Parbey J, Wang Q, Lei J, Espinoza-Andaluz M, Hao F, Xiang Y, et al. High-performance solid oxide fuel cells with fiber-based cathodes for low-temperature operation. Int J Hydrogen Energy 2020;45:6949–57. https://doi.org/10.1016/j.ijhydene.2019.12.125.

[10] Fan L, Liu L, Wang Y, Huo H, Xiong Y. One-dimensional $Sr_{0.7}Y_{0.3}CoO_{2.65-\delta}$ nanofibers as cathode material for IT-SOFCs. Int J Hydrogen Energy 2014;39:14428–33. https://doi.org/10.1016/j.ijhydene.2014.02.030.

[11] Enrico A, Aliakbarian B, Lagazzo A, Donazzi A, Botter R, Perego P, et al. Parameter optimization for the electrospinning of $La_{1-x}Sr_xCo_{1-y}Fe_yO_{3-\delta}$ fibers for IT-SOFC electrodes. Fuel Cell 2017;17:415–22. https://doi.org/10.1002/fuce.201600190.

[12] Teo WE, Ramakrishna S. A review on electrospinning design and nanofibre assemblies. Nanotechnology 2006;17. https://doi.org/10.1088/0957-4484/17/14/R01.

[13] Bhardwaj N, Kundu SC. Electrospinning: a fascinating fiber fabrication technique. Biotechnol Adv 2010;28:325–47. https://doi.org/10.1016/j.biotechadv.2010.01.004.

[14] Thenmozhi S, Dharmaraj N, Kadirvelu K, Kim HY. Electrospun nanofibers: New generation materials for advanced applications. Mater Sci Eng B Solid-State Mater Adv Technol 2017;217:36–48. https://doi.org/10.1016/j.mseb.2017.01.001.

[15] Enrico A, Zhang W, Lund Traulsen M, Sala EM, Costamagna P, Holtappels P. $La_{0.6}Sr_{0.4}Co_{0.2}Fe_{0.8}O_{3-\delta}$ nanofiber cathode for intermediate-temperature solid oxide fuel cells by water-based sol-gel electrospinning: synthesis and electrochemical behaviour. J Eur Ceram Soc 2018;38:2677–86. https://doi.org/10.1016/j.jeurceramsoc.2018.01.034.

[16] Costamagna P, Sala EM, Zhang W, Lund Traulsen M, Holtappels P. Electrochemical impedance spectroscopy of $La_{0.6}Sr_{0.4}Co_{0.2}Fe_{0.8}O_{3-\delta}$ nanofiber cathodes for intermediate temperature-solid oxide fuel cell applications: a case study for the 'depressed' or 'fractal' Gerischer element. Electrochim Acta 2019;319:657–71. https://doi.org/10.1016/j.electacta.2019.06.068.

[17] Shri Prakash B, Senthil Kumar S, Aruna ST. Properties and development of Ni/YSZ as an anode material in solid oxide fuel cell: a review. Renew Sustain Energy Rev 2014;36:149–79. https://doi.org/10.1016/j.rser.2014.04.043.

[18] Dees D, Claar T, Easler T. Conductivity of porous Ni/ZrO_2-Y_2O_3 cermets. J Electrochem Soc 1987;134:5–10.

[19] Yu JH, Park GW, Lee S, Woo SK. Microstructural effects on the electrical and mechanical properties of Ni-YSZ cermet for SOFC anode. J Power Sources 2007;163:926–32. https://doi.org/10.1016/j.jpowsour.2006.10.017.

[20] Fukui T, Ohara S, Naito M, Nogi K. Performance and stability of SOFC anode fabricated from NiO-YSZ composite particles. J Power Sources 2002;110:91–5. https://doi.org/10.1016/S0378-7753(02)00218-5.

[21] Kim JD, Kim GD, Moon JW, Park Y il, Lee WH, Kobayashi K, et al. Characterization of LSM-YSZ composite electrode by ac impedance spectroscopy. Solid State Ionics 2001;143:379–89. https://doi.org/10.1016/S0167-2738(01)00877-3.

[22] Østergård MJL, Clausen C, Bagger C, Mogensen M. Manganite-zirconia composite cathodes for SOFC: influence of structure and composition. Electrochim Acta 1995;40:1971–81. https://doi.org/10.1016/0013-4686(94)00332-U.

[23] Wang S, Jiang Y, Zhang Y, Yan J, Li W. Promoting effect of YSZ on the electrochemical performance of YSZ + LSM composite electrodes. Solid State Ionics 1998;113–115:291–303. https://doi.org/10.1016/s0167-2738(98)00379-8.

[24] Murray EP, Tsai T, Barnett SA. Oxygen transfer processes in (La,Sr)MnO_3/Y_2O_3-stabilized ZrO_2 cathodes: an impedance spectroscopy study. Solid State Ionics 1998;110:235–43. https://doi.org/10.1016/s0167-2738(98)00142-8.

[25] Sunde S. Monte Carlo simulations of polarization resistance of composite electrodes for solid oxide fuel cells. J Electrochem Soc 1996;143:1930. https://doi.org/10.1149/1.1836927.

[26] Costamagna P, Costa P, Antonucci V. Micro-modelling of solid oxide fuel cell electrodes. Electrochim Acta 1998;43:375–94. https://doi.org/10.1016/S0013-4686(97)00063-7.

[27] Costamagna P, Costa P, Arato E. Some more considerations on the optimization of cermet solid oxide fuel celle electrodes. Electrochim Acta 1998;43:967–72.

[28] Costamagna P, Panizza M, Cerisola G, Barbucci A. Effect of composition on the performance of cermet electrodes. Exp Theoretic Approach 2002;47:1079–89.

[29] Bertei A, Ruiz-Trejo E, Tariq F, Yufit V, Atkinson A, Brandon NP. Validation of a physically-based solid oxide fuel cell anode model combining 3D tomography and impedance spectroscopy. Int J Hydrogen Energy 2016;41:22381–93. https://doi.org/10.1016/j.ijhydene.2016.09.100.

[30] Enrico A, Cannarozzo M, Costamagna P. Modeling analysis of Bi-layer Ni-$(ZrO_2)_x(Y_2O_3)_{1-x}$ anodes for anode-supported intermediate temperature-solid oxide fuel cells. Energies 2014;7:5647–74. https://doi.org/10.3390/en7095647.

[31] Santos-gómez L, Martín F, Losilla ER, Marrero-lópez D. Short communication A novel multilaminated composite cathode for solid oxide fuel cells. Ceram Int 2019;45:18124–7. https://doi.org/10.1016/j.ceramint.2019.05.296.

[32] Zhao E, Jia Z, Zhao L, Xiong Y, Sun C, Brito ME. One dimensional $La_{0.8}Sr_{0.2}Co_{0.2}Fe_{0.8}O_{3-\delta}$/$Ce_{0.8}Gd_{0.2}O_{1.9}$ nanocomposite cathodes for intermediate temperature solid oxide fuel cells. J Power Sources 2012;219:133–9. https://doi.org/10.1016/j.jpowsour.2012.07.013.

[33] Zhao E, Ma C, Yang W, Xiong Y, Li J, Sun C. Electrospinning $La_{0.8}Sr_{0.2}Co_{0.2}Fe_{0.8}O_{3-\delta}$ tubes impregnated with $Ce_{0.8}Gd_{0.2}O_{1.9}$ nanoparticles for an intermediate temperature solid oxide fuel cell cathode. Int J Hydrogen Energy 2013;38:6821–9. https://doi.org/10.1016/j.ijhydene.2013.03.111.

[34] Enrico A, Costamagna P. Model of infiltrated $La_{1-x}Sr_xCo_{1-y}Fe_yO_{3-\delta}$ cathodes for intermediate temperature solid oxide fuel cells. J Power Sources 2014;272:1106–21. https://doi.org/10.1016/j.jpowsour.2014.08.022.

[35] Costamagna P, Sanna C, Campodonico A, Sala EM, Sažinas R, Holtappels P. Electrochemical impedance spectroscopy of electrospun $La_{0.6}Sr_{0.4}Co_{0.2}Fe_{0.8}O_{3-\delta}$ nanorod cathodes for intermediate temperature – solid oxide fuel cells. Fuel Cell 2019;19:472–83. https://doi.org/10.1002/fuce.201800205.

[36] www.gamry.com. [Accessed 17 December 2020].

[37] Napporn Teko W, Yaovi Holade, Boniface Kokoh, Shigenori Mitsushima, Kurt Mayer, Eichberger Bernd HV. Electrochemical measurement methods and characterization ON the cell level. Fuel Cells Hydrog. 2018:175–214. https://doi.org/10.1016/B978-0-12-811459-9.00009-8.

[38] Hirschorn B, Orazem ME, Tribollet B, Vivier V, Frateur I, Musiani M. Determination of effective capacitance and film thickness from constant-phase-element parameters. Electrochim Acta 2010;55:6218–27. https://doi.org/10.1016/j.electacta.2009.10.065.

[39] Yousefi V, Mohebbi-kalhori D, Samimi A. Equivalent electrical circuit modeling of ceramic-based microbial fuel cells using the electrochemical impedance spectroscopy (EIS) analysis. J Renew Energy Environ 2019;6:21–8.

[40] Nielsen J, Jacobsen T, Wandel M. Impedance of porous IT-SOFC LSCF:CGO composite cathodes. Electrochim Acta

2011;56:7963–74. https://doi.org/10.1016/j.electacta.2011.05.042.
[41] Jacobsen T, Hendriksen PV, Koch S. Diffusion and conversion impedance in solid oxide fuel cells. Electrochim Acta 2008;53:7500–8. https://doi.org/10.1016/j.electacta.2008.02.019.
[42] Koch S. Manual for elchemea analytical. DTU Energy; 2020.
[43] Ferrari T, Bertei A, Nicolella C. Estimation of 3D effective properties from 2D cross sections in porous electrodes. Electrochem Soc 2015;68:2991–3001. https://doi.org/10.1149/06801.2991ecst.
[44] Bertei A, Arcolini G, Ouweltjes JP, Wuillemin Z, Piccardo P, Nicolella C. Physically-based deconvolution of impedance spectra: interpretation, fitting and validation of a numerical model for lanthanum strontium cobalt ferrite-based solid oxide fuel cells. Electrochim Acta 2016;208:129–41. https://doi.org/10.1016/j.electacta.2016.04.181.
[45] Pham QP, Sharma U, Mikos AG. Electrospinning of polymeric nanofibers for tissue engineering applications: a review 2006;12.
[46] Dabirian F, Hosseini Ravandi SA, Pishevar AR. The effects of operating parameters on the fabrication of polyacrylonitrile nanofibers in electro-centrifuge spinning. Fibers Polym 2013;14:1497–504. https://doi.org/10.1007/s12221-013-1497-1.
[47] Deitzel JM, Kleinmeyer J, Harris D, Beck Tan NC. The effect of processing variables on the morphology of electrospun. Polymer 2001;42:261–72 (Guildf).
[48] Sanna C, Lagazzo A, Sala EM, Botter R, Costamagna P. IT-SOFC based on a disaggregated electrospun LSCF nanofiber electrode deposited onto a GDC electrolyte disc: preparation technique and morphological characterization. Bulg Chem Commun 2018;50:48–54.
[49] Jud E, Gauckler LJ. The effect of cobalt oxide addition on the conductivity of $Ce_{0.9}Gd_{0.1}O_{1.95}$. J Electroceram 2005;15:159–66. https://doi.org/10.1007/s10832-005-2193-3.
[50] Cannarozzo M, Del Borghi A, Costamagna P. Simulation of mass transport in SOFC composite electrodes. J Appl Electrochem 2008;38:1011–8. https://doi.org/10.1007/s10800-008-9527-1.
[51] Steele BCH, Bae J-M. Properties of $La_{0.6}Sr_{0.4}Co_{0.2}Fe_{0.8}O_{3-x}$ (LSCF) double layer cathodes on gadolinium-doped cerium oxide (CGO) electrolytes II. Role of oxygen exchange and diffusion. Solid State Ionics 1998;106:255–61.

ANNEX #2

“E. Squizzato, C. Sanna, A. Glisenti, P. Costamagna, Structural and Catalytic Characterization of La0.6Sr0.4MnO3 Nanofibers for Application in Direct Methane Intermediate Temperature Solid Oxide Fuel Cell Anodes, Energies. 14 (2021) 3602. https:// doi.org/10.3390/en14123602. “

energies

MDPI

Article

Structural and Catalytic Characterization of $La_{0.6}Sr_{0.4}MnO_3$ Nanofibers for Application in Direct Methane Intermediate Temperature Solid Oxide Fuel Cell Anodes

Enrico Squizzato [1], Caterina Sanna [2], Antonella Glisenti [1] and Paola Costamagna [2,*]

[1] Department of Chemical Sciences, University of Padova, Via F. Marzolo 1, 35131 Padova, Italy; enrico.squizzato.1@phd.unipd.it (E.S.); antonella.glisenti@unipd.it (A.G.)
[2] Department of Chemistry and Industrial Chemistry, University of Genoa, Via Dodecaneso 31, 16146 Genoa, Italy; caterina.sanna@edu.unige.it
* Correspondence: paola.costamagna@unige.it; Tel.: +39-(0)10-3532922; Fax: +39-(0)10-3538733

Abstract: In the present work, structural and catalytic characterization was performed on $La_{0.6}Sr_{0.4}MnO_3$ (LSM) nanofibers. The LSM nanofibers were obtained using the electrospinning technique. For comparison, LSM powders with identical composition were characterized as well. The LSM powders were prepared through a self-combustion citrate-based procedure. SEM, EDX, XRD, and BET investigations were carried out on both LSM nanofibers and powders, pointing out the different structural features. The LSM nanofibers showed a higher surface area than the LSM powders and a lower presence of strontium oxide on the surface. Results of the H_2-Temperature Programmed Reduction (TPR) tests showed evidence of a higher reactivity of the nanofibers compared to the powders. The catalytic characterization was performed utilizing a methane oxidation activity test, revealing a better catalytic performance of the LSM nanofibers: at 800 °C. The methane conversion achieved with the LSM nanofibers was 73%, which compared well with the 50% obtained with powders at 900 °C.

Keywords: electrospinning; nanofibers; fuel anode; H2-Temperature Programmed Reduction (TPR); Intermediate Temperature-Solid Oxide Fuel Cell (IT-SOFC)

Citation: Squizzato, E.; Sanna, C.; Glisenti, A.; Costamagna, P. Structural and Catalytic Characterization of $La_{0.6}Sr_{0.4}MnO_3$ Nanofibers for Application in Direct Methane Intermediate Temperature Solid Oxide Fuel Cell Anodes. *Energies* **2021**, *14*, 3602. https://doi.org/10.3390/en14123602

Academic Editor: Vladislav A. Sadykov

Received: 27 May 2021
Accepted: 10 June 2021
Published: 17 June 2021

1. Introduction

Fuel cells are electrochemical devices that directly convert the chemical energy of the fuel into electrical energy, avoiding the Carnot cycle and allowing high efficiencies to be achieved [1,2]. For this reason—and due to the constant increase in energy demand and consequently in greenhouse gas emissions—fuel cells have drawn great attention over the last few decades. Among all fuel cell configurations, intermediate temperature solid oxide fuel cells (IT-SOFCs) have solid-state components. These offer wide fuel flexibility, since they can operate with both hydrogen and light hydrocarbons [3,4]. The latter is an interesting feature, since natural gas and methane are cheap and abundant fuels, whereas pure hydrogen is mostly produced through the hydrocarbon reforming process [5–7]. In the SOFC anode, methane can either be electro-oxidized directly or undergo an internal reforming process in which methane is converted into hydrogen. Both options have been investigated in recent years [8,9]. The internal methane reforming process is generally carried out employing nickel-based electrodes. The main challenges of this process are controlling temperature gradients across the SOFC stacks and avoiding coke deposition over the nickel catalyst, with consequent catalyst deactivation. The previous issue is due to the strong endothermicity of the methane steam reforming reaction, resulting in uneven temperature distribution over the cell, with the possible formation of cold spots [6]. The latter issue is behind the need to operate the cell with a steam-to-carbon (S/C) ratio larger than three, which makes it difficult to achieve complete methane conversion [9]. Due to these problems, IT-SOFCs running internal steam methane reforming processes require

high costs and complex balance-of-plant (BoP) components. The direct electro-oxidation of methane represents an interesting alternative. The direct utilization of methane provides high open-circuit voltage, with high efficiency and simple BoP [8,10,11]. Nevertheless, the direct electrochemical oxidation of methane cannot be carried out employing standard nickel-based electrodes. Indeed, at an operating temperature above 800 °C, severe coke deposition takes place. At temperatures below 800 °C, the nickel-based anode provides low power densities [12]. Nevertheless, it is possible to use innovative anode materials. Interesting improvements have been made employing anode materials containing Cu, which does not catalyze the formation of graphite [9,10]. Another option is perovskite materials, which have been widely investigated in SOFC applications as both anode and cathode. The ideal perovskite, represented with the ABO_3 general formula, is a versatile metal oxide. It can be doped in both the A and B sites, affecting the oxygen stoichiometry and improving the oxygen ion—as well as the electron conductivity [13–18]. One state-of-the-art perovskite for SOFC cathode application is the Sr-doped $LaMnO_3$. Lanthanum substitution with strontium in the A-site results in an increase of electronic conductivity from 83 S cm^{-1} for $LaMnO_3$ to 320 S cm^{-1} for $La_{0.6}Sr_{0.4}MnO_3$ (LSM), at the same operating temperature of 800 °C [19]. The same type of material ($La_{0.8}Sr_{0.2}Mn_{0.98}O_3$) has also been studied for oxidative coupling of methane in solid oxide membrane reactors [20]. Conductive perovskites—such as $(La,Sr)(Cr,Mn)O_3/(Ce,Gd)_{2-\delta}$—have been tested in fuel cells with a direct methane configuration, reporting a polarization resistance of 0.496 Ωcm^2 at 850 °C [21].

In addition to new materials, innovative electrode architectures have been investigated as well. One-dimensional (1D) nanomaterials, like nanofibers and nanorods, have been widely studied as promising electrode structures [22–28]. Nanofiber electrodes feature a high void degree and active surface. The nanofiber manufacture process is carried out by applying a high voltage between a metal precursor solution, injected through a syringe equipped with a metal needle, and a metal collector. In order to achieve proper nanofiber formation, several equipment and solution parameters must be optimized. In particular, the solution flow rate, the applied voltage, the collector rotation speed, and the environment-relative humidity may affect the final nanofiber structure. On the other hand, once the process parameters are optimized, the results are reproducible [29–32]. Overall, nanofiber-based electrodes are expected to show better electrochemical performance than common powder ones. The two different architectures were investigated through the electrochemical impedance spectroscopy test (EIS), and the nanofiber-based electrode reported lower polarization resistance [33]. Nevertheless, the structural and microstructural origin of this behavior has, to date, received little attention.

In this work, our aim was to understand how the structure and morphology of the material affects its capability in activating and oxidating methane. The specific surface area is not the only aspect that can deeply differ from powder to fibers; the surface composition can be severely modified by the synthesis procedure, and can play a relevant role. Methane oxidation was selected as a model reaction because it is not easily promoted by perovskites or Ni-free catalysts. Moreover, this is a reaction of high technological impact; its application in direct methane IT-SOFCs is just one example. LSM electrospun nanofibers and powders were synthesized, and particular attention was paid to the optimization of the fiber procedure. The obtained materials were investigated using X-Ray Diffraction (XRD), Scanning Electron Microscopy (SEM), Energy Dispersive X-Ray Spectroscopy (EDX), and N2-Physisorption. Particular care was devoted to the study of the surface using X-Ray Photoelectron Spectroscopy (XPS). The H_2-Temperature Programmed Reduction (TPR) and methane oxidation activity tests were carried out to investigate stability and catalytic activity.

2. Experimental

2.1. $La_{0.6}Sr_{0.4}MnO_3$ Nanofibers Preparation

$Sr(NO_3)_2$ (Sigma-Aldrich, St. Louis, Missouri, USA, ACS 99+%), $La(NO_3)_3{\cdot}6H_2O$ (AlfaAesar, Haverhill, Massachusetts, USA, 99.9%), $(CH_3COO)_2Mn{\cdot}4H_2O$ (Sigma-Aldrich, 99.99%) were used as metal precursors for the starting solution for electrospinning. Each precursor was carefully weighted to achieve a molar ratio 0.6:0.4 for La:Sr, and 1:1 for (La + Sr):Mn. Before mixing, the metal precursors were dissolved in a solution of 60%/40% water/ethanol. Polyvinylpyrrolidone (PVP, Mw = 1.3×10^6 g/mol) was then added to the solution, achieving a weight ratio of 1:1.3 between the polymer and the metal salts. The PVP represented the 10% wt/wt of the whole solution. Dissolution was obtained using a magnetic stirrer for one night. The solution was then fed to the electrospinning device, equipped with a temperature and relative humidity (RH) regulator and a flat collector (Doxa Microfluidics, Malaga, Spain). The flow rate was 1 mL/h, the applied voltage was 1.7 kV/cm, RH was 40%, and the temperature was 25 °C. Next, the raw electrospun nanofiber tissue underwent heat treatment. The nanofibers were heated from room temperature to 800 °C at a constant heating rate of 0.5 °C/m. The cooling occurred without thermal control.

2.2. $La_{0.6}Sr_{0.4}MnO_3$ Powders Preparation

$La_{0.6}Sr_{0.4}MnO_3$ powders were synthesized by the citrate route [34]. Stoichiometric quantities of lanthanum nitrate ($La(NO_3)_3{\cdot}6H_2O$, Sigma-Aldrich 99.99%, powder), strontium nitrate ($Sr(NO_3)_2$, Sigma-Aldrich 99%, powder) and manganese acetate ($(CH_3COO)_2Mn{\cdot}4H_2O$ (Sigma-Aldrich, 99.99%) were dissolved in deionized water and nitric acid (HNO_3). Citric acid ($C_6H_8O_7$, Sigma-Aldrich $\geq$ 99.0%) was added as a complexing agent (with a molar ratio of 1.9:1 with respect to the total amount of cations) under stirring and then the solution was led to neutral pH by dropwise addition of ammonium hydroxide. At pH 7, the stirring was stopped and the solution was heated overnight to eliminate water and to allow the formation of a gel. The gel was burnt by heating at 400 °C. The formed powders were calcined at 800 °C for 6 h using a heating and cooling ramp of 6 °C/min.

2.3. Morphological and Structural Characterization

The morphological characterization of both the LSM nanofibers and LSM powders was carried out by acquiring images through the scanning electron microscope (SEM). The SEM and energy dispersive X-ray (EDX) spectroscopy measurements were carried out with a Zeiss SUPRA 40VP using a voltage of 20 kV. A dense bulk state of the samples was set on a sample-holder by an electroconductive adhesive tape and introduced in the measurement chamber. ImageJ software (NIH, Rockville, MD, USA) was used to identify the average diameter of both LSM powder particles and LSM nanofibers, starting from the SEM images. For the LSM powder particles, only the average diameter measurement was carried out. On the contrary, for the LSM nanofibers, a tool within ImageJ called DiameterJ was used to estimate the frequency distribution of the diameter of the nanofibers. This was accomplished through a two-step process. At first, the software performed the SEM image segmentation, producing a set of black/white pictures (Figures S1 and S2 in Supplementary Materials). Then, based on the black/white images, the software computed the frequency related to each nanofiber diameter. DiameterJ was specifically used for the estimation of nanofibers' diameter distribution, and could not be used to evaluate powder particle size distribution.

X-ray photoelectron spectroscopy (XPS) measurements were carried out employing a Perkin Elmer Φ 5600 ci Multi Technique System. The calibration of the spectrometer was calculated by assuming that the binding energy (BE) of the Au $4f_{7/2}$ line was 84.0 eV with respect to the Fermi level. Both extended spectra (survey-187.85 eV pass energy, 0.5 eV/step, 0.05 s/step) and detailed spectra (La 3d, Mn 2p, Sr 3d, O 1s and C 1s −23.5 eV pass energy, 0.1 eV/step, 0.1 s/step) were collected with a standard Al Kα source. The

atomic percentage was evaluated using PHI sensitivity factors [35] after Shirley-type background subtraction [36]. The charging effects on the peak positions were deleted by evaluating the BE differences with the C 1s peak set at 285.0 eV [37]. The samples were set in the chamber on a sample holder, on which was stuck an electroconductive adhesive tape. Bregg–Brentano geometry X-ray diffraction (XRD) analyses were performed, employing the Bruker D8 Advance diffractometer with a Cu Kα radiation (40 kV, 40 mA, λ = 0.154 nm). Temperature Programmed Reduction (H_2-TPR) measurements were performed with the Autochem II 2920 Micromeritics equipped with a thermal conductivity detector (TCD). H_2-TPR measurements were carried out in a quartz reactor using 50 mg of the sample, heating from room temperature to 900 °C at 8 °C/min with a constant flow of 5% vol. H_2/Ar (50 mL/min).

2.4. Catalytic Characterization

The methane oxidation catalytic activity tests were carried out at atmospheric pressure in a quartz reactor (6 mm ID) equipped with a packed bed of the LSM powders or nanofibers under study. Temperature was increased until 800 °C with a ramp of 2 °C min^{-1}. Temperature was monitored by a thermocouple right upstream of the bed. A gas mixture of methane and air (with a stoichiometric ratio of 1:2 between methane and oxygen) was used. Flows were dosed by a Vögtlin Red-y system. The total flow of 100 mL min^{-1} was kept constant, balancing it with He. After the reactor, water was eliminated by a cold trap. The composition of the gas mixture (before and after reaction) was measured by GC (Agilent 7890A), with a TCD detector and 13X (60/80 mesh, 1.8 m) and Porapak Q (1.8 m) columns.

3. Results and Discussion

3.1. Morphological Characterization

SEM images of LSM nanofibers and LSM powders are reported in Figure 1. Figure 1a,b shows the LSM powder particles after the sintering process. The images clearly show the presence of particles of different dimensions and shapes. Besides well-defined polyhedral crystals of more than one micron, small particles were evident. The average particle diameter, evaluated through the ImageJ software (NIH, Rockville, MD, USA), was 0.7 µm.

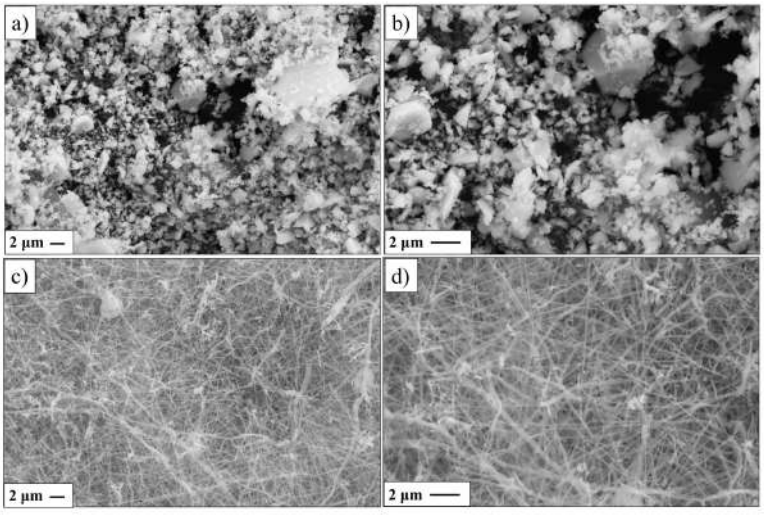

Figure 1. SEM images: (**a**,**b**) LSM powders; (**c**,**d**) LSM nanofibers.

Figure 1c,d shows the LSM nanofibers after the thermal treatment. There were thin nanofibers with no detachment, which ensured a compact network. It was possible to obtain these features after optimization of the many solution and process parameters. Indeed, as seen in Figure 1, the nanofibers showed a preferential cylindrical shape, which is the result of correct solvent evaporation during the electrospinning process. The proper evaporation of the solution was achieved by controlling three main parameters: the type of solvent,

the humidity in the electrospinning chamber, and the distance between the needle tip and the metal collector. Furthermore, the nanofibers appeared thin, but intact. This result was achieved by adding a suitable amount of polymer to the precursor solution and by optimizing the solution flow rate during the electrospinning process; essentially, the lower the amount of polymer—and the higher the flow rate—the thinner the produced fibers. Additionally, insufficient polymer quantities were shown to affect the nanofibers' ejection, provoking detachments. On the other hand, overly high flow rates require a high voltage, which would break the drop on the top of the needle, hindering the correct elongation.

The DiameterJ analysis was carried out on the SEM images of the LSM nanofibers in Figure 1c,d. Figure 2 shows, for each diameter range, the corresponding frequency, as evaluated by the software. The highest frequency was found for the diameter range 0.08–0.1 µm. Figures S1 and S2 in Supplementary Materials report the details of the DiameterJ analysis.

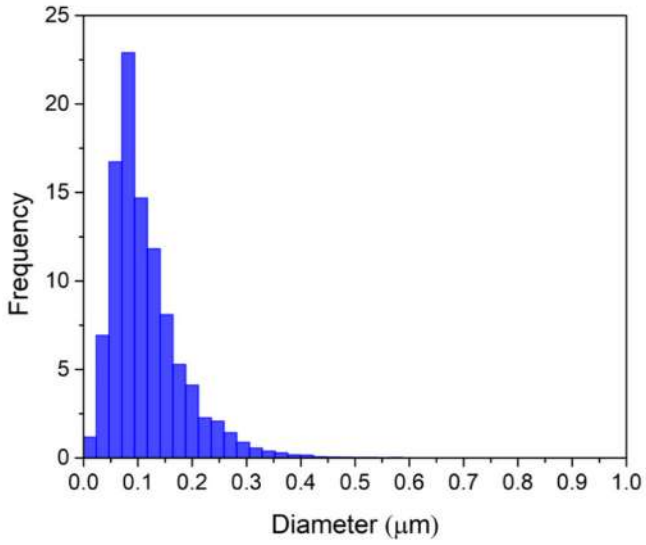

Figure 2. DiameterJ analysis of SEM images of LSM nanofibers after thermal treatment (Figure 1c,d).

XRD measurement was carried out on the heat-treated LSM nanofibers and citrate route powders to verify the achievement of the desired crystal phase. In Figure 3, the experimental patterns were reported together with the reference pattern. The experimental patterns contained all the peaks related to the reference, without any additional peaks. It confirmed that the thermal treatment permitted us to achieve crystallinity.

3.2. Chemical Characterization

Extended spectra (survey) were collected in the range of 0–1250 eV as reported in Figure 4. In the XPS survey spectra, no signals of elements other than the expected ones were detected. The atomic composition of the surface of the fibers, obtained from the XPS data, revealed a good correspondence with the nominal one (determined from the weighted amounts), as reported in Table 1.

The main difference between fibers and powders concerns the Sr/La atomic ratio. Following the nominal composition, Sr/La atomic should be 0.7. A value of 1.7 was observed in powders, whereas a value of 0.4 was detected in fibers. This suggests a marked strontium surface segregation in powders, which was not detected in fibers. Strontium segregation—with consequent formation of strontium oxide—is an undesired phenomenon that is already well-known in the literature for Sr-containing perovskites. The B-site transition metal of perovskites plays a critical role in catalytic activity, and therefore it is necessary to preserve the structure and the composition on the surface [38–40]. Furthermore, SrO is traceable to lower electronic conductivity. For all these reasons, avoiding Sr-enriched layers on LSM surface yields a substantial difference between the two syntheses and is an

important preliminary goal reached by electrospinning. Surface segregation properties of ionic solids are strongly related to their point defects. Assuming that, the presence or lack of Sr segregation on the two samples can be seen as evidence of a different presence of point defects in the two morphologies [41,42]. Further work will be spent to confirm this hypothesis.

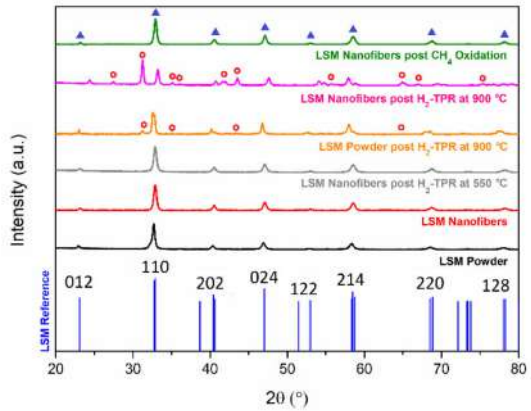

Figure 3. XRD results. The LSM reference pattern is shown in blue. Other experimental LSM patterns are as follows: powders after thermal treatment in black; electrospun nanofibers after thermal treatment in red; nanofibers after H_2-TPR performed up to 550 °C in grey and 900 °C in pink; powders after reduction in H_2 up to 900 °C in orange; and nanofibers after CH_4 oxidation up to 800 °C in green. Blue triangles refer to LSM peaks, while red circles denote MnO phase. All patterns are normalized with respect to their maximum values.

Table 1. XPS and EDX quantitative results of the atomic composition of LSM fibers and nanofibers. For better comprehension, nominal values are reported as well.

Theoretical %		XPS Experimental %		EDX Experimental %	
Element	**Nominal %**	**Fibers**	**Powders**	**Fibers**	**Powders**
O	60	58	74	62	58
La	12	15	4	12	12
Sr	8	6	7	7	7
Mn	20	21	15	19	22
Mn/(La + Sr)	1	1	1.4	1	1.2
Sr/La	0.7	0.4	1.7	0.6	0.6

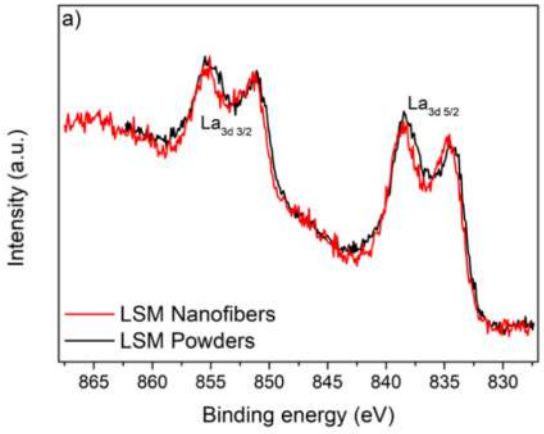

Figure 4. *Cont.*

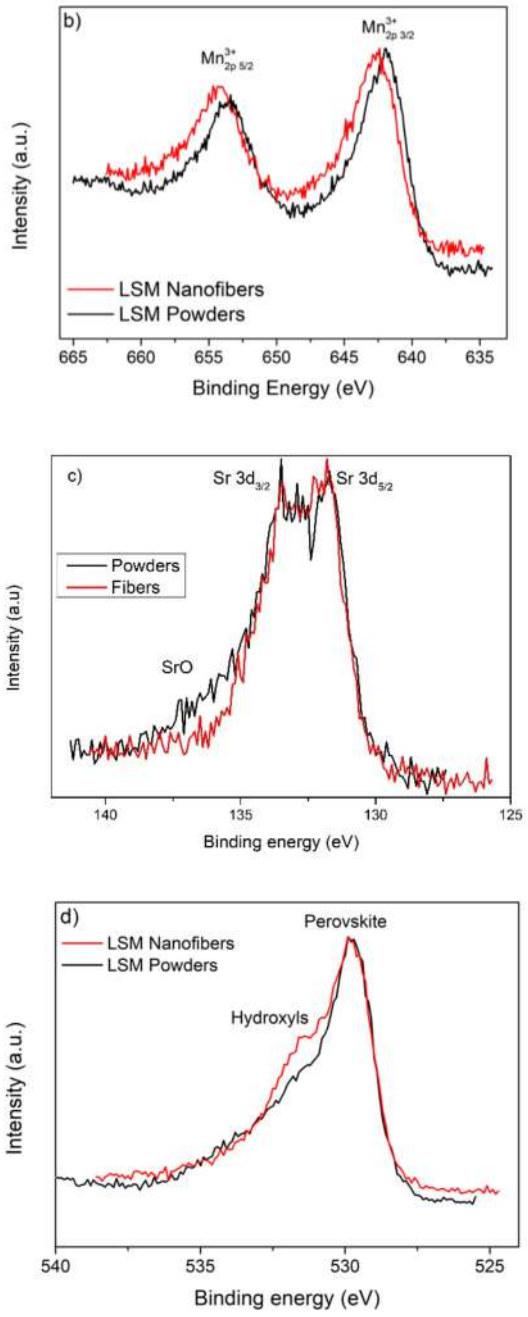

Figure 4. XP spectra of LSM samples prepared, respectively, by citrate gel method (black line) and electrospinning (red line) (the spectra are normalized with respect to their maximum value): (**a**) La 3d; (**b**) Mn 2p; (**c**) Sr 3d; (**d**) O 1s.

La 3d peak positions (834.6 and 851.0 eV for La $3d_{5/2}$ and La $3d_{3/2}$, respectively) were consistent with those expected for this element in a perovskite powder. [43,44] The La 3d level was characterized by a double peak for each spin-orbit component, attributed either to energy loss phenomena (induced by intense O 2p → La 4f charge transfer events) or strong final state mixing of electronic configurations [45]. The presence of the double signals was characteristic of La (III), as reported in Figure 4a. The Mn $2p_{3/2}$ spectral lines were centered in 642.4 eV, a typical position of Mn in oxides and manganites [46]. The Mn $2p_{3/2}$ peak asymmetry was due to the presence of a shake-up phenomenon for the Mn-emitted photoelectrons. This was observed, with a similar intensity, for both samples. The interpretation of the Mn 2p spectrum was complicated because of the multiple splitting

of the Mn 2p spectra of Mn^{4+}, Mn^{3+}, and Mn^{2+} ions. The exact oxidation state of Mn ions was difficult to evaluate but, according to the references [47], the observed binding energy of Mn $2p_{3/2}$, suggested that the oxidation state of Mn ions was (III) and (IV) for both LSM nanofibers and powders. Overall, the higher binding energy for LSM nanofibers compared to powders (See also Table S1 in Supplementary Materials) suggested a higher presence of Mn (IV). The higher presence of the redox couple $Mn^{4+/3+}$ in the nanofiber perovskite, as reported in Figure 4b, confirmed the Sr doping effectiveness and was in agreement with the absence of surface segregation. The stable insertion of Sr inside the perovskite cell presented a promising indication for an improvement of the material electronic conductivity. Sr 3d spectrum of LSM was fitted by the two components $3d_{5/2}$ and $3d_{3/2}$. Their BE was in accordance with the typical values of Sr-O in perovskite (131.8–134.3 eV) [46]. A small but significant difference was observed in the spectral region Sr3d is observed. In the spectrum which referred to the powders, it was possible to observe a tail around 135–137 eV which confirmed the more relevant presence of SrO Figure 4c. The fitting results underlined that Sr from perovskite was more evident in the fibers and the contribution due to the SrO in the powders (Table S1 in Supplementary Materials). The O 1s spectra showed the presence of two contributions centered around 530 and 531.6 eV; the contribution at lower BE was attributed to the lattice oxygen, whereas the one at higher BE was attributed to surface oxygen species. This contribution was more evident in the fibers' surface, as shown in Figure 4d. The presence of hydroxyl groups on the surface of the two samples was due to the exposition of the two samples in moist air. Nevertheless, the presence of these chemical species on the surface was not relevant to this study, since they were easily removed by heating the material during the catalytic analysis.

An EDX analysis was carried out to better understand the chemical composition in the inner region of the nanofibers. Table 1 shows the comparison between the nominal and the experimentally detected percentages of the two samples. No marked differences were present between fibers and powders with the nominal values, confirming that the two syntheses were successfully realized, and the Sr segregation was limited to a few surface monolayers. It is possible to assert, thus, that the two samples differed in morphology and in the chemical composition of their surfaces.

3.3. Temperature Programmed Reduction (H_2-TPR) and N_2-Adsorption-Desorption

The TPR profiles obtained for the fibers and the powders, as compared in Figure 5, showed two peaks, one at 430 °C and the other at 700 °C. Both were related to manganese cation reduction, since manganese is the only species that can be reduced in the analyzed temperature range. The lower temperature peak corresponded to the reduction of Mn^{4+}, while the second was due to the reduction from Mn^{3+} to Mn^{2+}. This hypothesis, suggested in the literature [48], was also confirmed by the XRD measurements performed after H_2-TPR. In the XRD patterns obtained after TPR, MnO was observed, but the main part of the sample maintained the perovskite structure. In Figure 3, the XRD pattern obtained for the fibers' sample reduced up to 550 °C (hypothetically, when the first reduction was finished, but the second one had still to start) underlined the absence of the MnO phase. This result confirmed that the peak at the higher temperature was due to the reduction to Mn^{2+}.

The experimental hydrogen consumption of a mole of fibers is about 9×10^{-5} mol, which is lower than the theoretical one (16.7×10^{-5} mol/mol). This was calculated assuming that all the Sr inserted in the sample promoted the manganese to Mn^{4+}, and all manganese was reduced to Mn^{2+}. This assumption was disproved, however, as the XRD after TPR showed LSM phase presence. Indeed, a simple calculation showed that about 50% of the Mn in the sample was reduced to Mn^{2+}. In addition, in order to understand whether the different morphology modified the stability, the same reducing treatment (5% H_2 in Ar at 900°) was performed on the powders. Significant differences were noted in the TPR profiles. The peak referring to $Mn^{4+/3+}$ reduction started at 305 °C for powders, or 35 °C higher than for nanofibers. Furthermore, the $Mn^{3+/2+}$ peak was much higher for nanofibers than for powders. These two results indicated that nanofibers featured a higher

reactivity. The post-reduction XRD was also significantly different. From Figure 3, it is possible to note how the powder diffractogram showed the same reflexes after reduction of MnO observed in the fibers, but with a lower intensity. The different behaviors observed between powders and fibers suggested lower reducibility of the powders. This could be explained by considering two aspects: first, the high presence of SrO on the powder's surface, which behaved like a coating for the perovskitic structure, protecting it from reduction; and second, the higher surface area observed for the fibers.

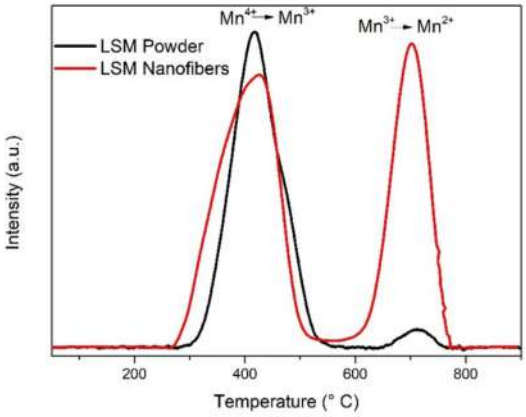

Figure 5. TPR profile of LSM nanofibers and powders. The patterns are normalized with respect to their maximum values.

Figure 6 shows the N_2-adsorption-desorption isotherms carried out on LSM nanofibers and powders. The BET plots of the two samples were both tracible to type IV isotherms, since they showed a hysteresis cycle between the adsorption and desorption processes. Therefore, at the same partial pressure, during the desorption, more nitrogen was desorbed than gas adsorbed in the adsorption process. The hysteresis served as a signal of a mesoporous material, but the small region between adsorption and desorption curves indicated that there was little dispersion of the average width of the pores [49]. The BET isotherms made it possible to determine the BET surface area. The surface area calculated for the LSM nanofibers was 16.7 m^2/g. A good correspondence with other studies in the literature could be observed in this material [50]. This value more than doubled the surface area calculated for the LSM powders (5.8 m^2/g). The latter was in line with the typical values for LSM perovskite powders synthesized by the citrate route and treated at the same calcination temperature (800 °C). The high BET surface area obtained for the LSM nanofibers, together with the absence of Sr-segregation, could explain the low hydrogen stability found at high temperatures in the TPR measurements.

3.4. Methane Oxidation Catalytic Activity Test

The catalytic results obtained with LSM nanofibers and powders are reported in Figure 7. A GC analysis of the reaction products, carried out after water condensation, showed that the molar ratio between the produced CO_2 and the consumed CH_4 was 1:1. No other reaction products were detected by the instrument. Therefore, since there was a full correspondence between methane consumption and CO_2 production, the complete oxidation of methane was confirmed. For the nanofibers, the onset temperature for methane oxidation was about 500 °C; for powders, it was 100 °C higher. The temperature of 50% methane conversion was lower for nanofibers (700 °C) than powders (900 °C). For the nanofibers, the maximum conversion was about 75% at 800 °C. Considering that the typical temperature range for SOFCs application was between 600 °C and 800 °C, it could be argued that this catalytic activity of nanofibers could be exploited in relationship with their application in these devices. Taking into account the catalytic results and the previous material characterizations, the higher activity of nanofibers could have two different

explanations. The first is the higher surface area of nanofibers (compared to powders) and, consequently, the higher number of active sites for the reaction. In addition, the higher performance of nanofibers could be explained by the previous XPS results. Indeed, SrO in the LSM powders surface was inactive to methane oxidation and covered the underneath of the perovskite structure. On the contrary, electrospinning synthesis made it possible to maintain the active perovskite phase up until the last atomic layers. Figure 3 compares the XRD patterns obtained for the nanofiber samples as-synthesized and after the reaction. No differences were detectable considering either the position of the peaks or their FWHM. Thus, no modification regarding the phase structure or crystallinity was attributable to the performed catalytic test.

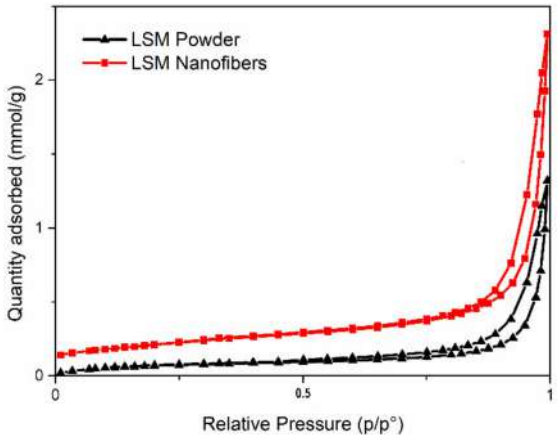

Figure 6. N_2-adsorption and desorption isotherms for LSM powders (black) and nanofibers (red).

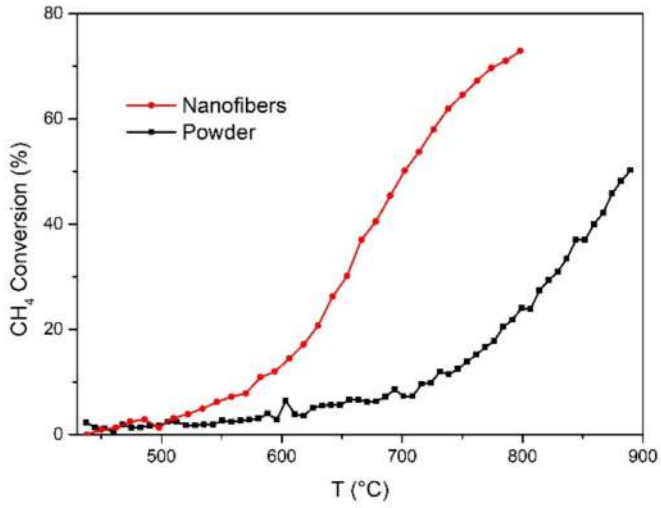

Figure 7. Catalytic activity in methane oxidation measured for LSM powders (black) and nanofibers (red).

4. Conclusions

$La_{0.6}Sr_{0.4}MnO_3$ (LSM), the SOFC cathode state-of-the-art material, was prepared in the form of nanofibers and powders. Proper synthesis and crystallinity were confirmed for both samples by XRD. The X-ray photoelectron spectroscopy (XPS) measurements showed that the two different synthesis routes heavily influenced the surface properties, since LSM powders displayed strontium oxide segregation, which was not detected in nanofibers. The catalytic activity toward direct methane oxidation was investigated for the two samples, showing that the onset temperature for methane oxidation was 500 °C with nanofibers, and 600 °C with powders. Methane conversion at 800 °C was 73% with nanofibers and 50%

at 900 °C with powders. Two explanations were proposed for the superior performance of nanofibers; first, the absence of strontium oxide segregation on the surface, which exhibited perovskitic active sites up until the last atomic layers; and second, the higher surface area (as revealed by BET analysis). Since the typical working temperature range for IT-SOFCs is 600–800 °C, the structural and catalytic characterizations performed in this work support the possibility of using LSM nanofibers on the anode side. This is particularly relevant, since it paves the way for the development of symmetric IT-SOFCs.

Supplementary Materials: The following are available online at https://www.mdpi.com/article/10.3390/en14123602/s1, Figure S1: Example of ImageJ segmentation process. In the left top corner, the original SEM picture is reported. The other images are the black/white segmented images. Figure S2: Example of ImageJ diameter location process. The red lines represent the central axes of the nanofibers in one of the segmented images. Figure S3: Fitting curves for the different element lines studied in this work. From top to bottom: O1s, La3d, Sr3d, Mn2p. On the left there are the powders spectra, while on the right those for fibers. Table S1: Fitting parameters of the different studied orbitals.

Author Contributions: Materials preparation, E.S. and C.S.; investigation, E.S. and C.S.; resources, A.G. and P.C.; data curation, E.S. and C.S.; writing—original draft preparation, E.S. and C.S.; writing—review, A.G. and P.C.; supervision, A.G. and P.C.; funding acquisition, A.G. and P.C. All authors have read and agreed to the published version of the manuscript.

Funding: The part of this research carried out at the University of Genoa (Italy) received financial support from the San Paolo Project 'COELUS-Production of renewable fuel by CO-ELectrolysis and reUSe of carbon dioxide' (ID ROL 32604).

Acknowledgments: C.S. and P.C. at the University of Genoa (Italy) acknowledge financial support from the San Paolo Project 'COELUS-Production of renewable fuel by CO-ELectrolysis and reUSe of carbon dioxide' (ID ROL 32604).

Conflicts of Interest: The authors declare no conflict of interest.

References

1. da Silva, F.S.; de Souza, T.M. Novel materials for solid oxide fuel cell technologies: A literature review. *Int. J. Hydrogen Energy* **2017**, *42*, 26020–26036. [CrossRef]
2. Huang, K.; Goodenough, J.B. *Solid Oxide Fuel Cell Technology*; Woodhead Publishing Limited: Cambridge, UK, 2009.
3. Mehmeti, A.; McPhail, S.J.; Pumiglia, D.; Carlini, M. Life cycle sustainability of solid oxide fuel cells: From methodological aspects to system implications. *J. Power Sources* **2016**, *325*, 772–785. [CrossRef]
4. Stambouli, A.; Traversa, E. Solid oxide fuel cells (SOFCs): A review of an environmentally clean and efficient source of energy. *Renew. Sustain. Energy Rev.* **2002**, *6*, 433–455. [CrossRef]
5. Kaur, P.; Singh, K. Review of perovskite-structure related cathode materials for solid oxide fuel cells. *Ceram. Int.* **2020**, *46*, 5521–5535. [CrossRef]
6. Panthi, D.; Choi, B.; Tsutsumi, A. Direct methane operation of a micro-tubular solid oxide fuel cell with a porous zirconia support. *J. Solid State Electrochem.* **2017**, *21*, 255–262. [CrossRef]
7. Costamagna, P.; Costa, P.; Antonucci, V. Micro-modelling of solid oxide fuel cell electrodes. *Electrochim. Acta* **1998**, *43*, 375–394. [CrossRef]
8. Tu, B.; Yin, Y.; Zhang, F.; Su, X.; Lyu, X.; Cheng, M. High performance of direct methane-fuelled solid oxide fuel cell with sa-marium modified nickel-based anode. *Int. J. Hydrogen Energy* **2020**, *45*, 27587–27596. [CrossRef]
9. Park, S.; Craciun, R.; Vohs, J.M.; Gorte, R.J. Direct oxidation of sulfur-containing fuels in a solid oxide fuel cell. *J. Electrochem. Soc.* **1999**, *146*, 3603–3605. [CrossRef]
10. Liu, J.; Madsen, B.D.; Ji, Z.; Barnett, S.A. A Fuel-Flexible Ceramic-Based Anode for Solid Oxide Fuel Cells. *Electrochem. Solid-State Lett.* **2002**, *5*, A122–A124. [CrossRef]
11. Grgicak, C.M.; Green, R.G.; Giorgi, J.B. SOFC anodes for direct oxidation of hydrogen and methane fuels containing H2S. *J. Power Sources* **2008**, *179*, 317–328. [CrossRef]
12. Perry Murray, E.; Tsai, T.; Barnett, S.A. A direct-methane fuel cell with a ceria-based anode. *Nature* **1999**, *400*, 649–651. [CrossRef]
13. Yang, G.; Jung, W.; Ahn, S.-J.; Lee, D. Controlling the Oxygen Electrocatalysis on Perovskite and Layered Oxide Thin Films for Solid Oxide Fuel Cell Cathodes. *Appl. Sci.* **2019**, *9*, 1030. [CrossRef]
14. Jiang, S.P. Development of lanthanum strontium cobalt ferrite perovskite electrodes of solid oxide fuel cells—A review. *Int. J. Hydrogen Energy* **2019**, *44*, 7448–7493. [CrossRef]

15. Richter, J.; Holtappels, P.; Graule, T.; Nakamura, T.; Gauckler, L.J. Materials design for perovskite SOFC cathodes. *Monatshefte Chem. Chem. Mon.* **2009**, *140*, 985–999. [CrossRef]
16. Jun, A.; Kim, J.; Shin, J.; Kim, G. Perovskite as a Cathode Material: A Review of its Role in Solid-Oxide Fuel Cell Tech-nology. *ChemElectroChem* **2016**, *3*, 511–530. [CrossRef]
17. Escudero, M.; Irvine, J.; Daza, L. Development of anode material based on La-substituted $SrTiO_3$ perovskites doped with manganese and/or gallium for SOFC. *J. Power Sources* **2009**, *192*, 43–50. [CrossRef]
18. Mailadil, T.S. ABO_3 type perovskites. In *Dielectric Materials for Wireless Communication*; Elsevier Science: Amsterdam, The Netherlands, 2008.
19. Jiang, S.P. Development of lanthanum strontium manganite perovskite cathode materials of solid oxide fuel cells: A review. *J. Mater. Sci.* **2008**, *43*, 6799–6833. [CrossRef]
20. Farrell, B.L.; Linic, S. Oxidative coupling of methane over mixed oxide catalysts designed for solid oxide membrane reactors. *Catal. Sci. Technol.* **2016**, *6*, 4370–4376. [CrossRef]
21. Chen, X.J.; Liu, Q.L.; Khor, K.A.; Chan, S.H. High-performance (La,Sr)(Cr,Mn)O_3/(Gd,Ce)$O_{2-\delta}$ composite anode for direct ox-idation of methane. *J. Power Sources* **2007**, *165*, 34–40. [CrossRef]
22. Costamagna, P.; Sanna, C.; Campodonico, A.; Sala, E.M.; Sažinas, R.; Holtappels, P. Electrochemical Impedance Spectroscopy of Electrospun $La_{0.6}Sr_{0.4}Co_{0.2}Fe_{0.8}O_{3-\Delta}$ Nanorod Cathodes for Intermediate Temperature–Solid Oxide Fuel Cells. *Fuel Cells* **2019**, *19*, 472–483.
23. Enrico, A.; Zhang, W.; Traulsen, M.L.; Sala, E.M.; Costamagna, P.; Holtappels, P. $La_{0.6}Sr_{0.4}Co_{0.2}Fe_{0.8}O_{3-\delta}$ nanofiber cathode for intermediate-temperature solid oxide fuel cells by water-based sol-gel electrospinning: Synthesis and electrochemical behaviour. *J. Eur. Ceram. Soc.* **2018**, *38*, 2677–2686. [CrossRef]
24. Sanna, C.; Zhang, W.; Costamagna, P.; Holtappels, P. Synthesis and electrochemical characterization of electrospun nanofiber cathodes for intermediate-temperature solid oxide fuel cells. *Int. J. Hydrogen Energy* **2020**, *46*, 13818–13831. [CrossRef]
25. Zhao, E.; Liu, X.; Liu, L.; Huo, H.; Xiong, Y. Effect of $La_{0.8}Sr_{0.2}Co_{0.2}Fe_{0.8}O_{3-\delta}$ morphology on the performance of composite cathodes. *Prog. Nat. Sci. Mater. Int.* **2014**, *24*, 24–30. [CrossRef]
26. Jeon, Y.; Myung, J.H.; Hyun, S.H.; Shul, Y.G.; Irvine, J.T. Corn-cob like nanofibres as cathode catalysts for an effective microstruc-ture design in solid oxide fuel cells. *J. Mater. Chem. A* **2017**, *5*, 3966–3973. [CrossRef]
27. Koo, J.Y.; Lim, Y.; Kim, Y.B.; Byun, D.; Lee, W. Electrospun yttria-stabilized zirconia nanofibers for low-temperature solid oxide fuel cells. *Int. J. Hydrogen Energy* **2017**, *42*, 15903–15907. [CrossRef]
28. Fan, L.; Xiong, Y.; Liu, L.; Wang, Y.; Kishimoto, H.; Yamaji, K.; Horita, T. Performance of $Gd_{0.2}Ce_{0.8}O_{1.9}$ infiltrated $La_{0.2}Sr_{0.8}TiO_3$ nanofiber scaffolds as anodes for solid oxide fuel cells. *J. Power Sources* **2014**, *265*, 125–131. [CrossRef]
29. Zhang, W. Electrospinning for Solid Oxide Fuel Cells. In *Electrospinning for Advanced Energy and Environmental Applications*; CRC Press; Taylor & Francis Group: Boca Raton, FL, USA, 2016.
30. Teo, W.E.; Ramakrishna, S. A review on electrospinning design and nanofibre assemblies. *Nanotechnology* **2006**, *17*, R89–R106. [CrossRef]
31. Deitzel, J.; Kleinmeyer, J.; Harris, D.; Tan, N.B. The effect of processing variables on the morphology of electrospun nanofibers and textiles. *Polymer* **2001**, *42*, 261–272. [CrossRef]
32. Aruna, S.; Balaji, L.; Kumar, S.S.; Prakash, B.S. Electrospinning in solid oxide fuel cells—A review. *Renew. Sustain. Energy Rev.* **2017**, *67*, 673–682. [CrossRef]
33. Costamagna, P.; Holtappels, P.; Sanna, C. Metal Oxide Nanofiber-Based Electrodes in Solid Oxide Fuel Cells. In *Metal Oxide-Based Nanofibers Their Applications*; Elsevier: Amsterdam, The Netherlands, in press.
34. Marcilly, C.; Courty, P.; Delmon, B. Preparation of highly dispersed mixed oxides and oxide solid solutions. *J. Am. Ceram. Soc.* **1970**, *53*, 56. [CrossRef]
35. Moulder, J.F.; Stickle, W.F.; Sobol, P.E.; Bomben, K.D. *Handbook of X-ray Photoelectron Spectroscopy*; Perkin-Elmer Corporation: Waltham, MA, USA, 1992.
36. Mills, K.A.; Davis, R.F.; Kevan, S.D.; Thornton, G.; Shirley, D.A. Angle-resolved photoemission determination of Λ-line valence bands in Pt and Au using synchrotron radiation. *Phys. Rev. B* **1980**, *22*, 581–592. [CrossRef]
37. Wagner, C.D.; Riggs, W.M.; Davis, L.E.; Moulder, J.F.; Muilenberg, G.E. *Handbook of X-ray Photoelectron Spectroscopy*; Perkin-Elmer Corp., Physical Electronics Division: Eden Prairie, MN, USA, 1979.
38. Wu, Q.H.; Liu, M.; Jaegermann, W. X-ray photoelectron spectroscopy of $LaSrMnO_3$. *Mater. Lett.* **2005**, *59*, 1980–1983. [CrossRef]
39. Caillol, N.; Pijolat, M.; Siebert, E. Investigation of chemisorbed oxygen, surface segregation and effect of post-treatments on La0.8Sr0.2MnO3 powder and screen-printed layers for solid oxide fuel cell cathodes. *Appl. Surf. Sci.* **2007**, *253*, 4641–4648. [CrossRef]
40. Jiang, S.P.; Love, J.G.; Zhang, J.P.; Hoang, M.; Ramprakash, Y.; Hughes, A.E.; Badwal, S.P.S. The electrochemical performance of LSM/zirconia-yttria interface as a function of a-site non-stoichiometry and cathodic current treatment. *Solid State Ion.* **1999**, *121*, 1–10. [CrossRef]
41. Horvath, G.; Gerblinger, J.; Meixner, H.; Giber, J. Segregation driving forces in perovskite titanates. *Sens. Actuators B Chem.* **1996**, *32*, 93–99. [CrossRef]
42. Nowotny, J. Interface defect chemistry of oxide ceramic materials. *Solid State Ion.* **1991**, *49*, 119–128. [CrossRef]
43. Glisenti, A.; Galenda, A.; Natile, M.M. $LaMnO_3$: Influence of the Addition of Ba and Sr. *Surf. Sci. Spectra* **2009**, *16*, 83. [CrossRef]

44. Natile, M.M.; Ugel, E.; Maccato, C.; Glisenti, A. $LaCoO_3$: Effect of synthesis conditions on properties and reactivity. *Appl. Catal. B Environ.* **2007**, *72*, 351–362. [CrossRef]
45. Vasquez, R.P. X-ray photoemission measurements of $La_{1-x}Ca_xCoO_3$ (x = 0, 0.5). *Phys. Rev. B* **1996**, *54*, 14938–14941. [CrossRef] [PubMed]
46. Berger, D.; Matei, C.; Papa, F.; Macovei, D.; Fruth, V.; Deloume, J.P. Pure and doped lanthanum manganites obtained by com-bustion method. *J. Eur. Ceram. Soc.* **2007**, *27*, 4395–4398. [CrossRef]
47. Murray, J.W.; Dillard, J.G.; Giovanoli, R.; Moers, H.; Stumm, W. Oxidation of Mn(II): Initial mineralogy, oxidation state and ageing. *Geochim. Cosmochim. Acta* **1985**, *49*, 463–470. [CrossRef]
48. Florea, M.; Somacescu, S.; Postole, G.; Urda, A.; Neatu, F.; Neatu, S.; Massin, L.; Gelin, P. $La_{0.75}Sr_{0.25}XO_3$ (X = Fe, Mn or Cr) with coking tolerance for CH_4/H_2O reaction: Effect of H_2S on catalytic performance. *Catal. Sci. Technol.* **2019**, *9*, 2351–2366. [CrossRef]
49. Dollimore, D.; Spooner, P.; Turner, A.D. The bet method of analysis of gas adsorption data and its relevance to the calculation of surface areas. *Surf. Technol.* **1976**, *4*, 121–160. [CrossRef]
50. Chen, Y.; Bu, Y.; Zhang, Y.X.; Yan, R.; Ding, D.; Zhao, B.; Yoo, S.; Dang, D.; Hu, R.; Yang, C.; et al. A Highly Efficient and Robust Nanofiber Cathode for Solid Oxide Fuel Cells. *Adv. Energy Mater.* **2017**, *7*, 1601890. [CrossRef]

ANNEX #3

"C. Sanna, E. Squizzato, P. Costamagna, P. Holtappels, A. Glisenti, Electrochemical study of symmetrical intermediate temperature - solid oxide fuel cells based on La0.6Sr0.4MnO3 / Ce0.9Gd0.1O1.95 for operation in direct methane/air, Electrochim. Acta. 409 (2022) 139939. https://doi.org/10.1016/j.electacta.2022.139939. "

Electrochimica Acta 409 (2022) 139939

Contents lists available at ScienceDirect

Electrochimica Acta

journal homepage: www.elsevier.com/locate/electacta

Electrochemical study of symmetrical intermediate temperature - solid oxide fuel cells based on $La_{0.6}Sr_{0.4}MnO_3$ / $Ce_{0.9}Gd_{0.1}O_{1.95}$ for operation in direct methane / air

Caterina Sanna [a], Enrico Squizzato [b], Paola Costamagna [a,*], Peter Holtappels [c], Antonella Glisenti [b]

[a] Department of Chemistry and Industrial Chemistry, University of Genoa, Via Dodecaneso 31, Genoa 16146, Italy
[b] Department of Chemical Sciences, University of Padova and ICMATE, Via F. Marzolo 1, Padova 35131, Italy
[c] Department of Energy Conversion and Storage, Technical University of Denmark, Elektrovej, 375, 234, 2800 Kgs. Lyngby, Denmark

ARTICLE INFO

Article history:
Received 29 October 2021
Revised 3 January 2022
Accepted 16 January 2022
Available online 20 January 2022

Keywords:
Direct methane fuel cell (DMFC)
Electrochemical impedance spectroscopy (EIS)
Equivalent circuit modeling (ECM)
Gerischer
Intermediate temperature - solid oxide fuel cell (IT-SOFC)
$La_{0.6}Sr_{0.4}MnO_3$ (LSM), Mixed Ionic-electronic conductor (MIEC)

ABSTRACT

$La_{0.6}Sr_{0.4}MnO_3$ (LSM), which is considered a state-of-the-art solid oxide fuel cell (SOFC) cathode, is investigated for application as an anode in direct methane intermediate temperature - solid oxide fuel cells (IT-SOFCs). $Ce_{0.9}Gd_{0.1}O_{1.95}$ (CGO) is used as the electrolyte. The characterized electrode is a composite LSM/CGO, prepared in two different configurations: LSM crushed electrospun nanofibers / GDC powders, and LSM powders / GDC powders. The electrodes are tested in both air and direct methane conditions. At 815 °C, the polarization resistance R_p = 1.6 Ωcm^2 in air, and R_p = 0.15 Ωcm^2 in methane. Since perovskite-type manganites may show poor stability in reducing atmosphere, electrode stability is investigated. It is found that LSM shows a reversible modification of the crystal structure, assuming a Ruddlesden-Popper (RP) structure when exposed to methane. The RP structure is expected to be more stable compared to the LSM single perovskite. Furthermore, the composite electrode is expected to benefit from the presence of CGO, which is stable in reducing conditions.

1. Introduction

The possibility of feeding the anode side of a fuel cell directly with methane is attracting wide interest. This would be the first step towards a direct utilization of the natural gas capillary distributed by the gas grid, without the intermediate steam methane reforming (SMR) reactor, which is present in all the fuel cell systems currently under study [1]. The overall system would benefit in terms of reduction in complexity and cost. Furthermore, the SMR reactor is particularly prone to faults related to carbon deposition, due to the capability of the traditional Ni catalyst to catalyze also the methane cracking reaction, which produces coke which is then deposited on the catalyst, hindering its activity. It has been demonstrated that these SMR faults are particularly dangerous for the integrity of the downstream fuel cell and the whole system [2].

Direct utilization of methane is possible only in high-temperature fuel cells (molten carbonate fuel cells, MCFCs, and solid oxide fuel cells, SOFCs) and has been widely investigated for SOFCs. In SOFCs, internal methane utilization can proceed through two different pathways. The first relies on the direct electrochemical oxidation of methane by the oxygen ions coming from the electrolyte. The second pathway is based on the internal steam reforming process, which produces hydrogen and carbon monoxide, which are then oxidized electrochemically. The two pathways can take place simultaneously [3].

Ni, which is the typical electrocatalyst used at the SOFC anode for the electrochemical hydrogen oxidation reaction (HOR), is also the traditional catalyst for the SMR reaction, which seems an ideal conjuncture to implement internal SMR. Nevertheless, from an engineering point of view, this is not a practically viable option with traditional high-temperature SOFCs, because, at their typical temperatures of about 1000 °C, the internal SMR reaction is very fast. Since the SMR reaction is strongly endothermal, this causes a dramatic temperature decrease at the cell inlet, associated with severe mechanical tensile stresses in the solid structure, which easily cause fractures and ultimately break down of the cell. On the other hand, it has been demonstrated on theoretical ground, through SOFC simulation models, that the milder temperature of Intermediate Temperature-Solid Oxide Fuel Cells (IT-SOFCs),

* Corresponding author.
E-mail address: paola.costamagna@unige.it (P. Costamagna).

https://doi.org/10.1016/j.electacta.2022.139939
0013-4686/

i.e. 600–850 °C, provides ideal conditions for the internal SMR reaction to develop uniformly, with no steep temperature gradients associated [4]. Nevertheless, an unresolved issue remains, i.e. the tendency of methane to undergo cracking on the Ni catalysts. This implies that carbon deposition can occur also inside the SOFC anode, and this is widely confirmed by the experimental practice. To avoid this problem, a quantity of steam largely superior to the stoichiometric value is added to methane. Steam-to-carbon (S/C) is the parameter used to describe the level of added steam, and values as high as S/C = 3 are used in the experimental practice to ensure coke-free operation. Unluckily, steam dilution lowers the operating voltage of the fuel cell, and thus the electrical power produced. This is further exasperated by the product water generated by the electrochemical reaction occurring in the cell.

To overcome the coke deposition problems, intensive research is being devoted to innovative coke-free catalytic materials. In this respect, research follows two distinct pathways for IT-SOFCs and industrial reactors. For industrial SMR reactors, incorporation of CeO_2 into Ni-based catalysts is known to offer a kinetic resistance to carbon deposition for many hydrocarbon oxidation reactions because of its facilitated redox activity [5]. It has been demonstrated that intimate contact between Ni and CeO_2 is essential in reducing the extent of carbon deposition during the reforming reaction [5]. The beneficial role of ceria in inhibiting coke deposition has been demonstrated also with methane dry reforming [6]. For IT-SOFCs, perovskitic-type structures decorated with exsolved Ni particles are reported in the recent literature as stable, coke-free, and high-electrochemical performance anode materials for internal SMR in low S/C operating conditions. $La_{1.5}Sr_{1.5}Mn_{1.5}Ni_{0.5}O_{7\pm\delta}$ Ruddlesden-Popper (RP) structures have been investigate [7–9]. Ru substituted $La_{0.6}Sr_{0.2}Cr_{0.85}Ni_{0.15}O_3$ perovskites have been investigated as well [3]. In both cases, the exsoluted particles of Ni and Ru respectively, are demonstrated to play a key role in triggering the SMR process.

In this work, $La_{0.6}Sr_{0.4}MnO_3$ (LSM), a well-known electronic conducting perovskite that is the state-of-the-art SOFC cathode, is investigated for application at the anode side, as a direct methane electrode. $Ce_{0.9}Gd_{0.1}O_{1.95}$ (GDC) is used as the electrolyte. The electrode is a classical composite LSM/GDC, tested in both air and direct methane conditions. Since different manufacturing processes are supposed to affect the material crystal structure, the LSM/GDC electrodes are manufactured using both the citrate route method to prepare the LSM powders, and the electrospinning technique to prepare the LSM nanofibers. Electrospinning is an innovative manufacturing method that makes it possible to produce 1-D materials like nanotubes, nanowires, nanorods, and nanofibers. These 1-D structures own interesting features such as high surface area, which results in better electrochemical performance compared to conventional powders electrodes [10–16]. In particular, the electrospinning procedure is expected to produce nanofibers with a higher amount of LSM perovskite structure on the surface, compared to the powders prepared with the citrate route method [15]. The stability of the electrode in anode conditions is investigated as well, since perovskite-type manganites may show poor stability in reducing atmosphere [17]. Nevertheless, LSM with RP structure tested in reducing conditions has demonstrated superior stability than its parent perovskites [17].

The results pave the way for the development of symmetrical LSM/GDC IT-SOFCs, with important advantages such as the reduction of manufacturing costs and thermomechanical issues [17–19]. Furthermore, the electrospinning technique is cost-effective, simple, and reproducible. Recently, interesting improvements in nanofiber mass production through electrospinning have been reported [20–23]. The intensive study carried out on needleless and centrifugal electrospinning methods allowed an increase in the nanofibers production: indeed, the typical 0.1–1 g/h production rate is extended to 13.5 g/h in the case of PAN solutions [20] and even 450 g/h in pharmaceutical industries [23].

2. Materials and methods

2.1. $La_{0.6}Sr_{0.4}MnO_3$ nanofibers preparation

The sol-gel solution used for the electrospinning process is based on $Sr(NO_3)_2$ (Sigma-Aldrich, ACS 99+%), $La(NO_3)_3 \cdot 6H_2O$ (AlfaAesar, 99.9%), and $(CH_3COO)_2Mn \cdot 4H_2O$ (Sigma-Aldrich, 99.99%) as metal precursors. The metal salts are weighted to reach the following molar ratios: 0.6:0.4 for La:Sr, and 1:1 for (La+Sr):Mn. Then, they are dissolved in a mixture of 60%/40% water/ethanol using a magnetic stirrer. Then, polyvinylpyrrolidone (PVP, Mw = 1.3 106 g/mol) is added to the solution maintaining a weight ratio between polymer and precursors salts of 1:1.3. Furthermore, the amount of PVP is added up to 10% wt/wt of solution. After one night of mixing, complete dissolution is achieved.

The solution obtained is then fed to the electrospinning equipment (Doxa Microfluidics). The device is equipped with a 10 cm diameter cylinder metal collector and a relative humidity (RH) regulator. The solution is fed at a flow rate of 1 ml/h, using an applied voltage gradient of 2.2 kV/cm, and a rotational speed of 200 rpm. The chamber atmosphere is maintained at an RH of 40%.

Lastly, the raw electrospun nanofibers are heat-treated. They are brought to 800 °C, with a ramp of 0.5 °C/min. After reaching 800 °C, cooling to room temperature takes place without thermal control. During heat treatment, polymer burns, and the desired crystal structure is obtained. The effect of heat-treatment on the nanofibers was analyzed in previous works [14,24,25].

2.2. $La_{0.6}Sr_{0.4}MnO_3$ powders preparation

LSM powders are synthesized through the citrate route [26]. Stoichiometric quantities of lanthanum nitrate ($La(NO_3)_3{\cdot}6H_2O$, Sigma-Aldrich 99.99%, powder), strontium nitrate ($Sr(NO_3)_2$, Sigma-Aldrich 99%, powder) and manganese acetate ($(CH_3COO)_2Mn{\cdot}4H_2O$ (Sigma-Aldrich, 99.99%) are dissolved in deionized water and nitric acid (HNO_3). The complexing agent is citric acid ($C_6H_8O_7$, Sigma-Aldrich $\geq$ 99.0%). It is added under stirring, with a molar ratio of 1.9:1 to the total amount of cations. After that, the solution is led to neutral pH by dropwise addition of ammonium hydroxide. At pH 7, stirring is stopped, and the solution is heated overnight to eliminate water and allow the formation of a gel. The gel is burned, heating at 400 °C. The formed powders are calcined at 800 °C for 6 h using a heating and cooling ramp of 6 °C/min.

2.3. Chemical and physical characterization

X-ray spectroscopy (XPS) measurements are carried out with a Perkin Elmer Φ 5600ci Multi Technique System. The spectrometer is calibrated by assuming the binding energy (BE) of the Au $4f_{7/2}$ line to be 84.0 eV with respect to the Fermi level. Both extended spectra (survey-187.85 eV pass energy, 0.8 eV/step, 0.05 s/step) and detailed spectra (La 3d, Mn 2p, Sr 3d, O 1 s and C 1 s - 23.5 eV pass energy, 0.1 eV/step, 0.1 s/step) are collected with a standard Al Kα source. The atomic percentage is evaluated using the PHI sensitivity factors after Shirley-type background subtraction. The peak positions are corrected for the charging effects by considering the C 1 s peak at 285.0 eV and evaluating the BE differences [27]. X-ray diffraction (XRD) analyses are performed with a Bruker D8 Advance diffractometer with Bragg-Brentano geometry using a Cu Kα radiation (40 kV, 40 mA, λ = 0.154 nm). Field emission scanning electron microscopy and energy-dispersive X-ray spectroscopy

(EDX) measurements are carried out on a Zeiss SUPRA 40VP at acceleration voltages of 20 kV. X-ray diffraction (XRD) analyses are performed employing the Bruker D8 Advance diffractometer with Bragg-Brentano geometry using a Cu Kα radiation (40 kV, 40 mA, $\lambda = 0.154$ nm).

ImageJ software [28,29] is used to identify the average diameter of the LSM nanofibers, starting from the SEM images. In particular, DiameterJ, a tool of ImageJ, is used to estimate the frequency distribution of the diameter of the nanofibers.

2.4. Electrochemical impedance spectroscopy

The electrochemical measurements are performed using symmetrical cells (LSM-GDC (50:50)/GDC/LSM-GDC (50:50)) made of dense gadolinium doped ceria ceramics (theoretical density > 96%) as electrolyte. Both LSM powders and nanofibers are ground with commercial GDC powders (Fuelcellmaterials) until a uniform color is obtained. After that, the electrode inks are realized adding the α-terpineol solvent to the powders which act as a vehicle liquid, but it also confers the proper viscosity. The electrolyte is prepared by pressing GDC powders in round shape, 20 mm of diameter and 1 mm of thickness, and then calcined at 1500 °C for 5 h (3 °C/min heating ramp). The electrodes are prepared by depositing the ink onto the GDC electrolyte through the tape casting process, and then they are heat-treated at 1050 °C for 2 h (3 °C/min heating ramp). After thermal treatment, three symmetrical cells are prepared. The first is assembled with the nanofiber-based electrodes with 30 μm of thickness, while the second one is assembled with the powder-based electrodes with 70 μm of thickness. Furthermore, another powder-based symmetrical cell is prepared with an electrode thickness of 40 μm. Electrochemical Impedance Spectroscopy (EIS) measurements are carried out using an Autolab Frequency Response Analyser. The frequencies scanned are from 0.003 Hz to 1 MHz and set to amplitude 0.02 V. The tests are carried out at 865 °C, 815 °C, 765 °C, 715 °C, and 665 °C. The raw experimental data are corrected by subtracting the inductance contribution of the device wires, which is one of the major sources of error is given by the stray components of the device [30].

2.5. Equivalent circuit-based modeling

The EIS experimental data obtained in air and methane atmosphere are fitted through different equivalent circuit models. The equivalent circuits adopted in this work consist of serial resistance Rs, placed in series with RQ elements. In some cases, also the Gerischer and the FLW elements are used. These ECs were previously proposed in [30,31] where Rs in series with RQ elements were used to fit EIS data obtained with composite LSM/GDC or LSM/YSZ electrodes.

The Rs element represents all the ohmic contributions: the electrolyte and electrodes ohmic resistances, and the contact resistances between the electrodes and the current collectors:

$$R_S = R_{electrolyte} + 2(R_{contact} + R_{electrode}) \quad (1)$$

The RQ element consists of a resistor and a constant phase element (CPE) placed in parallel. It is generally used to simulate electrochemical phenomena which take place at the electrode/electrolyte interface [32]. Indeed, the resistor simulates the charge transfer process, i.e. the oxygen reduction reaction (ORR), whereas the capacity Q of the CPE is associated with the electrode/electrolyte double layer. The RQ impedance equation is:

$$Z_{RQ}(\omega) = \frac{1}{R_{RQ}^{-1} + Q(j\omega)^{\alpha}} \quad (2)$$

Where α is a CPE parameter, which is independent of frequency. When $\alpha = 1$, the electrode/electrolyte interface is simulated as a CPE which is become an ideal capacitor, with capacity Q and units (F) and the Nyquist plot of the RQ impedance is a semi-circle. Otherwise, when α is lower than 1, the deviations from the ideality are considered in the RQ impedance. For example, the heterogeneity which takes place at the electrode/electrolyte interface, or to continuously distributed time constants for the charge-transfer reactions is reflected in the α value [33]. In this condition, the RQ impedance representation in the Nyquist plot is a depressed semi-circle. The Q unit becomes (F $s^{\alpha-1}$), so an equivalent capacitance Q_{equiv} is calculated with units (F), and the formula is below:

$$Q_{equiv} = \frac{(QR)^{1/\alpha}}{R} \quad (3)$$

The Gerischer element is used to simulate both charge transport and charge transfer reaction in the bulk of the electrode [34]. The representing equation is:

$$Z_G(\omega) = \frac{1}{Y_G(k + j\omega)^{0.5}} \quad (4)$$

The k parameter is the oxygen surface exchange coefficient, whereas Y_G incorporates the parameters related to oxygen mass transport, as well as structural parameters [35].

When the EIS tests are carried out at high temperatures, generally an additional arc appears at low frequencies due to the gas diffusion limitations [36,37]. This additional arc is well fit with the Finite-Length-Warburg (FLW):

$$Z_{FLW}(\omega) = \frac{\tanh\left((Bj\omega)^{0.5}\right)}{(Y_{FLW}\, j\omega)^{0.5}} \quad (5)$$

B and Y_{FLW} are phenomenological coefficients.

The EC used to fit the experimental data obtained in air, changes with temperature: between 665 and 765 °C the Rs-RQ-RQ-RQ is used, whereas at a higher temperature the EC is modified to Rs-RQ-RQ-FLW.

The EIS experimental data obtained in methane are analyzed with two ECs, which are represented in Fig. 1. The first model (Mod1) is Rs-G. Since the electrolyte used in this work is a pellet made with GDC, which tends to become an electronic conductor when exposed to a reducing atmosphere i.e. methane, a second equivalent is proposed. The second model (Mod2) consists of an Rs-G circuit with the Rs resistance (which is identified as R_2 in Fig. 1b) placed in parallel to the G element, simulating the effect of possible electrolyte short-circuiting.

3. Results

3.1. SEM

Fig. 2 shows the SEM image of the LSM nanofibers (a) and the LSM powders (b) before the mixing procedure with the GDC powders. Both the LSM nanofibers and powders are reported after the thermal treatment. The LSM nanofibers appear intact and well entangled, providing a good network. The Diameter-J analysis carried out on the Fig. 2(a) calculates the frequency of the nanofiber's diameter, identifying the highest frequency in the range between 80 and 100 nm. In Fig. 2(b) it is possible to see the LSM powders microstructure. The LSM powders show particles with different dimensions and shapes: some particles are well-defined polyhedral with diameter sizes in the micron range, but at the same time it is also possible to identify nanosized particles. Furthermore, in the previous work [15], the BET surface area analysis was carried out on both the LSM nanofibers and the LSM powders. The BET pointed out an active surface area of 16.7 m^2/g for the LSM nanofibers, a value which is around two times the typical values for LSM powders prepared by the citrate route.

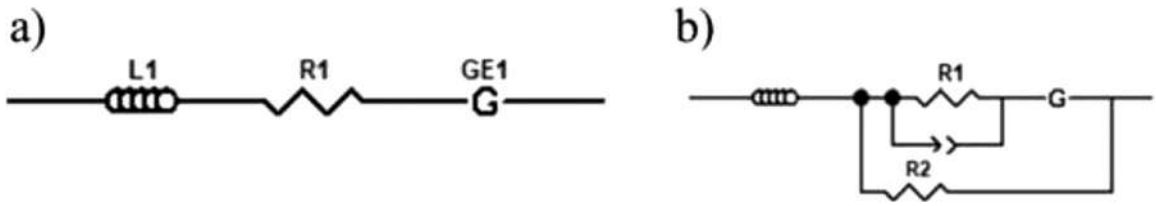

Fig. 1. Schematic representation of the two models used to fit the experimental data obtained in methane. (a) Rs-G model (Mod1); (b) RQ-G with a parallel Rs model (Mod2).

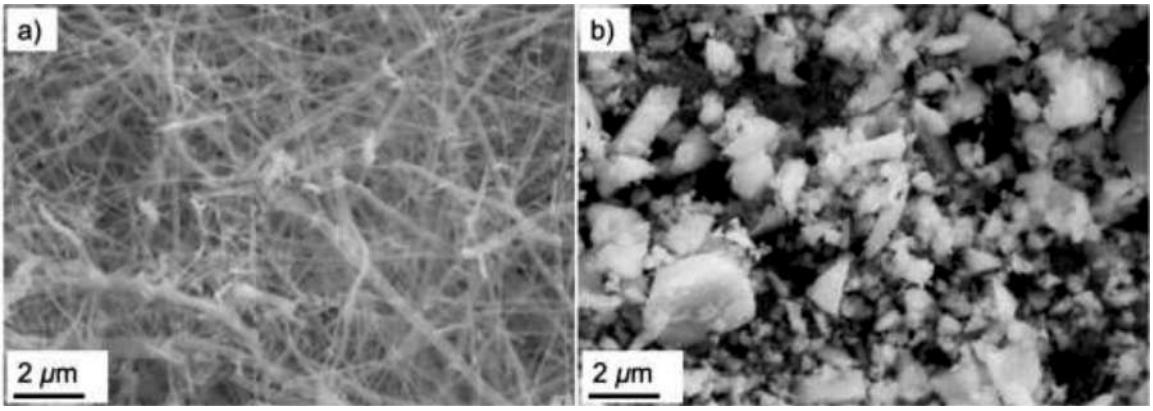

Fig. 2. (a) SEM image of LSM nanofibers after heat treatment. (b) LSM powders after thermal treatment.

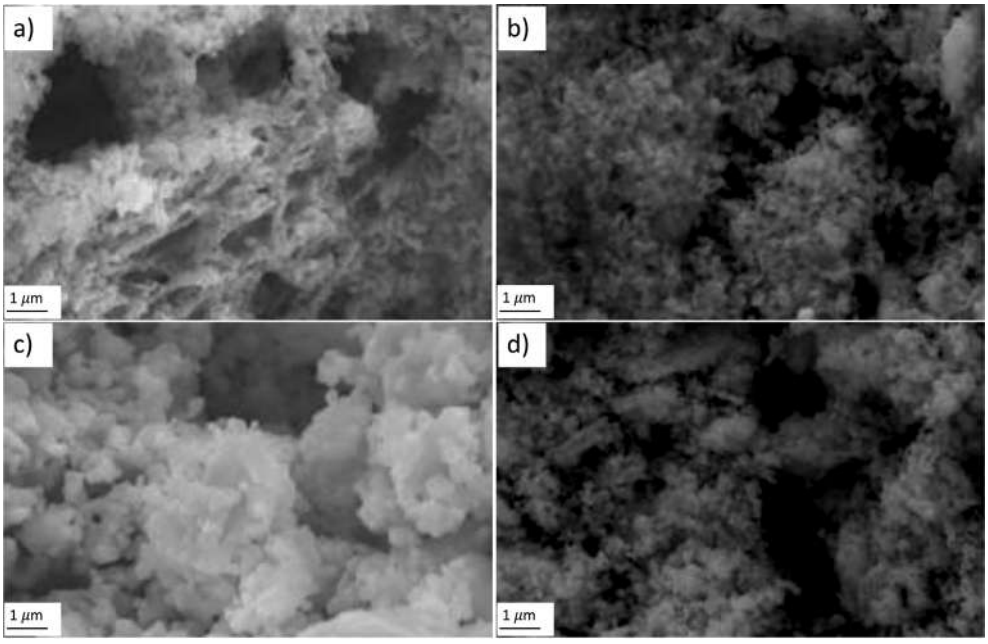

Fig. 3. SEM images of LSM/GDC nanofiber-based electrode (a–c) and LSM/GDC powder-based electrode (b–d). Electrode internal morphology: (a,b) pre-electrochemical test, (c,d) post-electrochemical test.

As reported previously, both the LSM powders and the LSM nanofibers are crushed with the GDC powder to prepare the precursor electrode ink. Fig. 3 shows the SEM images of the LSM/GDC nanofiber (a-c) and powder (b-d) based electrodes. The characterization is carried out before (a-b) and after (c-d) the EIS tests. It is possible to see that in every image of Fig. 3 the electrode appears homogeneous, with a good void degree and no agglomeration. After the crushing procedure, the microstructures of the LSM/GDC nanofibers electrode and the LSM/GDC powders electrode, reported in Fig. 3, do not show as many differences as in Fig. 2. Indeed, the grinding process used to mix the GDC with the LSM leads to the loss of the original nanofiber structure, which is naturally well elongated and arranged in a continuous network. Furthermore, as shown in Fig. 3 there is no difference in particle size between the GDC powder and the LSM one, instead, the size distribution appears homogenous. Lastly, Fig. 3 (c, d) demonstrates no relevant changes in porosity and morphology despite the high temperatures reached during the electrochemical tests.

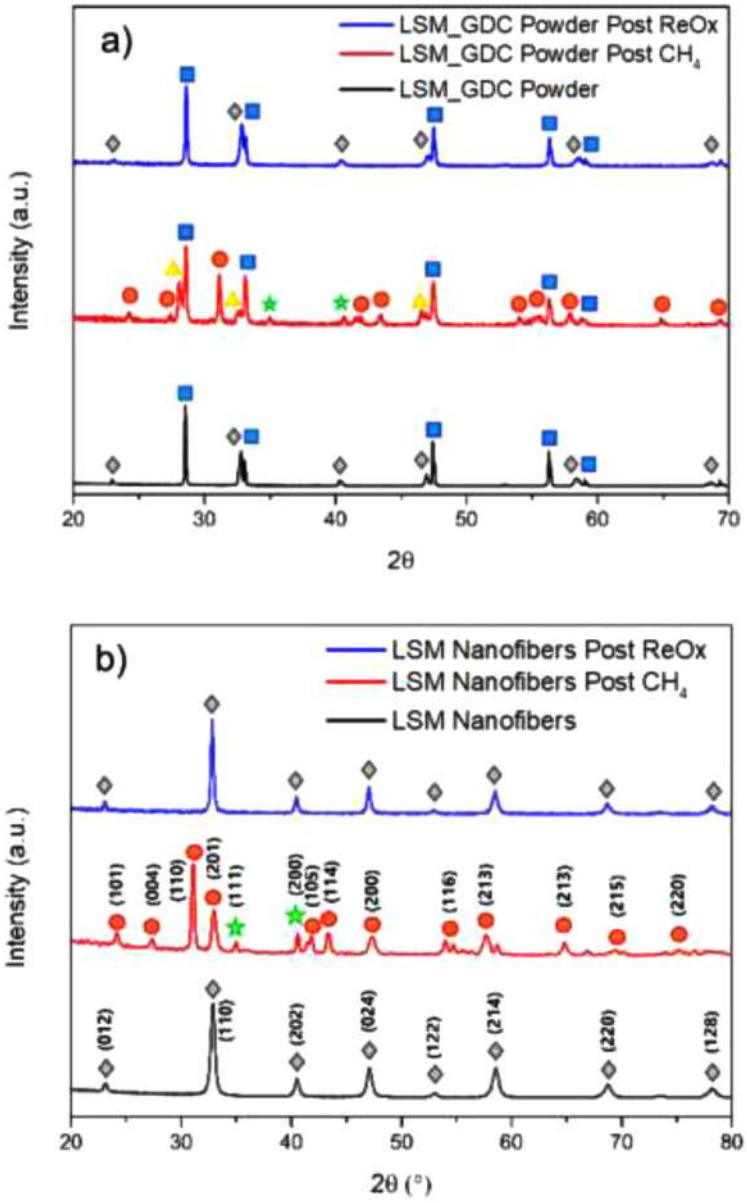

Fig. 4. (a) LSM_GDC composite electrode and (b) LSM nanofibers stability test results. Peak identification: Blue square: $Ce_{0.9}Gd_{0.1}O_2$; grey rhombus: $La_{0.6}Sr_{0.4}MnO_3$; Orange circles: $La_{1.2}Sr_{0.8}MnO_{3.84}$; Yellow triangle: $Ce_{11}O_{20}$; Green star: MnO.

3.2. XRD and stability tests

As reported above, perovskites are versatile materials widely employed in SOFC operation at intermediate temperatures. However, one perovskite drawback is the material stability during the test operation, in particular in reducing atmosphere. For this reason, the stability of the LSM/GDC electrodes is investigated in the methane atmosphere. Firstly, the LSM/GDC powder-based electrode undergoes an XRD analysis before being employed in the electrochemical test. The experimental pattern shows only signals related to the GDC and LSM crystal structures as reported in Fig. 4(a). Then, the LSM/GDC electrode is placed in a powder rector, where a constant flow of pure methane is fluxed, and the temperature is raised to 900 °C and then cooled down. The XRD measurement is carried out on electrode after the thermal treatment in methane and the result is reported in Fig. 4(a) as well. In this case, some additional peaks are individuated: the LSM stoichiometry is modified, and the experimental pattern shows that the LSM achieves the Ruddlesden-Popper configuration (RP, $A_{n+1}B_nO_{3n+1}$). The RP structures are more stable in reducing atmospheres and are widely used as electrode materials for SOFC [38–40]. Furthermore, in literature, many works report the possibility to use $La_xSr_{2-x}MnO_4$ based materials for anodes fueled directly by methane [8,41]. However, from Fig. 4(a) it is possible to see that during the thermal treatment in methane, the formation of MnO takes place as well, which is expected taking into account the H_2-TPR analysis performed in our previous work [15]. In particular, the performed H_2-Temperature Programmed Reduction (TPR) analysis highlighted the reduction of the Mn^{3+} in the perovskite structure to Mn^{2+} at an operating temperature around 700 °C. Finally, the experimental pattern reported in Fig. 4(a) shows another additional phase which is given by the reduction of GDC in an oxygen-deficient phase ($Ce_{11}O_{20}$). However, these new phases, which are obtained by exposing the electrodes material to a reductive atmosphere, are not irreversible. Indeed, the same sample analyzed after the methane thermal treatment undergoes an oxidative thermal treatment up

to 900 °C in air, and the XRD carried out after the re-oxidation demonstrate the absence of the additional phases (Fig. 4(a)). Furthermore, the experimental pattern shows that the LSM modifies its crystal structure from the RP configuration to the former single perovskite. In Fig. 4(b) it is possible to observe the results achieved performing the same analysis on LSM nanofibers, which follows the same behavior of the powder-based one. In this case, the analyzed nanofibers are not ground with GDC, to ensure that the reversible transition is intrinsic of the LSM and not due to the interaction with GDC.

3.3. Electrochemical impedance spectroscopy in air

As discussed above, LSM is considered the state-of-the-art material for SOFC cathodes, and composite LSM/GDC electrodes have been widely investigated in the last decades. Therefore, this section aims at comparing the EIS results obtained in the air from the LSM/GDC nanofibers-based and powder-based electrodes with the available literature, to have a firm starting point for the subsequent discussions. The electrochemical characterization is carried out on the 30 μm thick nanofiber-based electrode and the 70 μm thick powder-based electrode

Fig. 5 shows the Nyquist and Bode plots of the EIS experimental data obtained in air between 665 and 865 °C with the nanofiber-based LSM/GDC electrode. The contributions of the fitting elements used in the equivalent circuit model are reported as well. Between 665 and 765 °C, the equivalent circuit used to fit the data is the Rs-RQ-RQ-RQ. At each temperature, the experimental data display two main arcs in the Nyquist plot: the first one is a little semicircle placed at high frequencies, while the second one is the main curve which covers the middle and low range of frequencies. The small high-frequency arc is well fitted with two RQ elements, and it is identified as RQ1. When the temperature rises, the shape of the main arc changes. Indeed, the two RQ elements modify their relative contributions to the overall polarization resistance, until 815 °C where only one RQ fits the main curve. Thus, between 815 and 865 °C, the equivalent circuit used to fit the experimental data becomes Rs-RQ-RQ-FLW. The FLW element is used to simulate the small arc which appears at low frequencies, due to the shrinkage of the main impedance arcs in the Nyquist plot. This additional contribution, fitted with the FLW element coherently with the previous works [25,35,42], is associated with the gas diffusion resistance [43]. Despite the electrode containing both LSM and GDC, which are respectively pure electronic and ionic conductors, the Nyquist plot is not associated with the Gerischer behavior, which is normally related to mixed electronic-ionic conductors. Indeed, the Nyquist shape is the sum of several semicircles in series. However, this behavior is quite common for composite electrodes investigated as cathodes, and several examples are reported in the literature. Murray et al. performed EIS tests on a symmetrical cell made with an LSM/YSZ composite electrode. Despite the YSZ being considered the state-of-the-art material for HT-SOFC, the experimental data reported in the Nyquist plot do not show the common Gerischer shape, otherwise, the spectra represent the sum of several semicircle arcs, which are fitted with an Rs-RQ-RQ equivalent circuit [44]. Other composite electrodes made with LSM and YSZ have been tested, achieving the same behavior [45–47]. Furthermore, Costamagna et al. characterized symmetrical cells made with YSZ nanofibers infiltrated with LSM solution. The change in the electrode microstructure results in lower polarization resistance [48], but also in this case the experimental point in the Nyquist plot shows a sum of several semicircle arcs as seen in the previous cases [12]. The behavior reported for the LSM/YSZ composite electrode is also found for substituting the ionic conductor material. Indeed, Luo et al. performed an EIS test on LSM/GDC symmetrical cells and no Gerischer behavior is reported in the Nyquist plot, but the experimental data show the already discussed sum of several arcs [49]. Other LSM/GDC composite electrodes have been tested obtaining the same behavior [50,51]. On the contrary, several mixed ionic and electronic conductors, which have generally high electronic conductivity but low ionic conductivity, report a Gerischer behavior in the Nyquist plot after EIS characterization. One of the most studied MIEC materials is the LSCF perovskite, which is considered the state-of-the-art material for IT-SOFC. Costamagna et al. carried out the investigation on LSCF nanofiber electrodes, achieving the typical Gerischer shape in the Nyquist plot [35]. Furthermore, some LSCF/GDC composite electrodes have been investigated as well, reporting the same Gerischer behavior [25,52]. Sunde et al. performed some simulations on several composite electrodes. They found out that when the electrode and the electrolyte material are randomly mixed to form a composite electrode, it is possible that one phase is not connected to its bulk phase, causing a lack of percolation of one phase [53,54]. The problem detected by Sunde et al. and Costamagna et al. may be the reason why the Nyquist plots shown in Fig. 5 do not show the Gerischer behavior. If one phase does not percolate in the electrode thickness, it is possible that the electronic and ionic pathways are not properly connected limiting the conduction of ionic or electrons, and so the reaction. On the contrary, a mixed conductor has both the pathways in the same material and the reaction can take place wherever in the electrode thickness. According to the literature [55], when LSM/YSZ composite electrodes are tested in an air atmosphere it is possible to identify five main processes, and each of them is associated with an RQ arc. Fig. 5 shows the presence of three well-defined processes at 665 °C, while at high temperature only two of them are reported at 815 °C. In the range of temperature between these two limits the EC contributions appear shifted and overlapped, which implies a difficult interpretation of the processes related to them. For this reason, it is not possible to assign an accurate process that takes place in the cell to the EC element used to fit the data. The only contribution which is present at each investigated temperature is the little semicircle at high frequencies. This contribution is also detected in the LSM/YSZ composite electrode characterized by Murray et al., who attributed this high-frequency contribution to the grain boundary resistance made by the YSZ particles inside the electrode [44]. Lastly, at 800 °C a small additional arc in Fig. 5 appears at low frequencies. Costamagna et al. investigated this process as well, identifying this additional arc at low frequencies and high temperatures and associating this contribution to the gas diffusion resistance [25,35,42].

Fig. 6 shows the Nyquist plots of the EIS experimental data obtained between 665 and 865 °C in air with the 70 μm thick powder-based LSM/GDC electrode. The shape is slightly different from that reported in Fig. 5. Indeed, the RQ1 contribution is only identified at 665 °C and over 765 °C the unique contribution to the overall polarization resistance is given by only one RQ element. Thus, at 665 °C the experimental data are fitted with the Rs-RQ-RQ-RQ equivalent circuit, at 715 °C the EC becomes Rs-RQ-RQ and between 765 and 865 °C, the EC becomes Rs-RQ. However, the correlation between the fitting elements and the electrochemical phenomena is in accordance with the discussion reported above for the LSM/GDC nanofiber electrodes. Furthermore, there is a good correlation between the electrochemical performances obtained with the nanofiber-based electrode and the powder one. The polarization resistance obtained with the nanofiber-based LSM/GDC electrode at 815 °C is 1.6 Ωcm^2, a value quite similar to the 1.08 Ωcm^2 obtained with the powder-based LSM/GDC electrode at the same operating temperature. Furthermore, the obtained results are consistent with the literature data found for composite electrodes based on LSM. Indeed, LSM/YSZ composite electrode shows a polarization resistance of 1.5 Ωcm^2

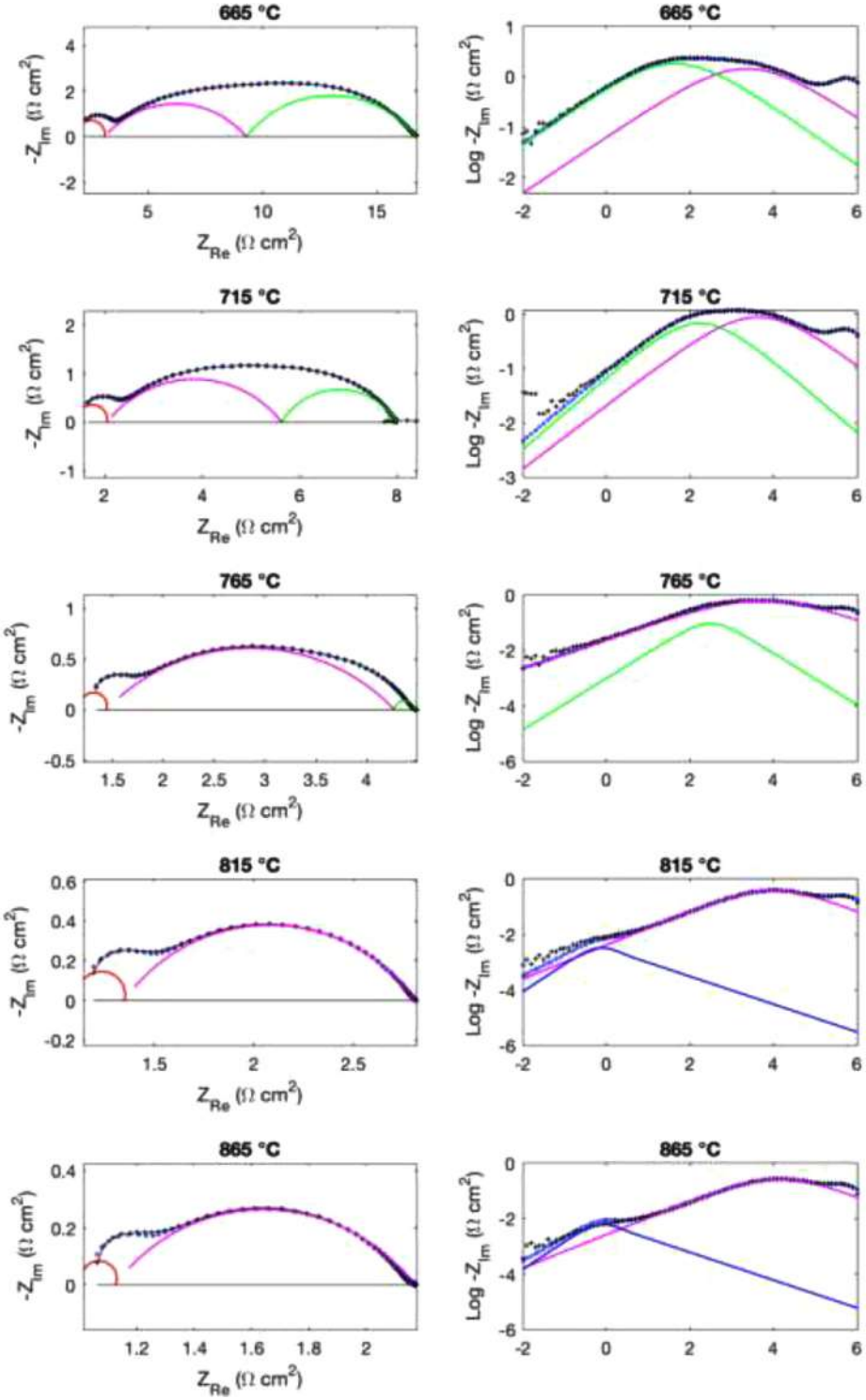

Fig. 5. Nyquist (left) and Bode (right) plots of the EIS results obtained with the nanofiber-based LSM/GDC electrode at operating temperatures from 665 to 865 °C, in air atmosphere: · experimental data; -□- fitting through the Rs-RQ-RQ equivalent circuit model; – RQ1 contribution; – RQ2 contribution; – RQ3 contribution and – FLW contribution.

at 800 °C, while LSM/GDC electrodes reports 0.5 Ωcm^2 at 750 °C [12,56].

In Fig. 7 the reverse of the polarization resistance (R_p^{-1}) of the LSM/GDC nanofiber-based electrode and 70 μm thick powder-based electrode are reported in an Arrhenius plot. The activation energies are respectively 115 kJ/mol and 153 kJ/mol. In particular, the value found for the nanofiber-based cathode is consistent with the activation energy reported in the literature for pure LSM electrode, which is 121 kJ/mol [11,57,58]. This may suggest that in the investigated LSM/GDC composite electrodes when used as cathodes in air atmosphere, only the LSM is electrochemically active, rather than the GDC.

In Fig. 8 the 1/Rp vs 1000/T of the RQ1 polarization resistance and the overall polarization resistance of the LSM/GDC nanofiber

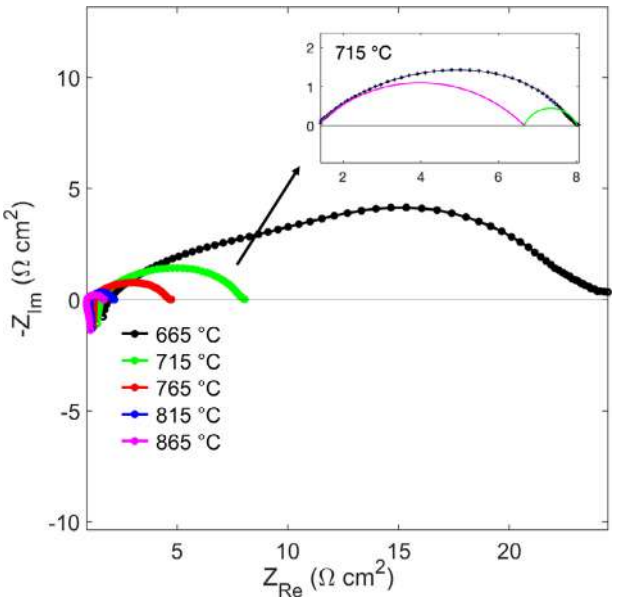

Fig. 6. Nyquist plot of EIS results obtained with the 70 μm thick powder-based LSM/GDC electrode at operating temperatures from 665 to 865 °C, in air atmosphere. Inset: Nyquist at 715 °C, · experimental data; -□- fitting through the Rs-RQ-RQ equivalent circuit model; – RQ2 contribution; – RQ3 contribution.

electrode are reported. In particular, polarization resistance of the RQ1 shows an Arrhenius behavior as compared to the temperature; furthermore, the activation energy is 90 kJ/mol, which is very similar to the 96 kJ/mol found by Murray et al. in [44].

3.4. Electrochemical impedance spectroscopy in methane

In this section, the EIS experimental data obtained in a 97% of methane and 3% of water atmosphere with the LSM/GDC 30 μm thick nanofibers-based and the 70 μm thick LSM/GDC powder-based electrodes are discussed. Figs. 9 and 10 show the Nyquist plots of the EIS experimental data obtained between 715 and 865 °C with the nanofiber-based LSM/GDC electrode. Furthermore, the Rs-G fitting result at 715 °C is reported as well. The shape of the raw experimental data is different compared to the data reported in Fig. 5. Indeed, the data acquired in the reducing atmosphere report a typical Gerischer behavior, instead of a sum of semicircles as reported for the data obtained in air. In both Figs. 9 and 10 serial and polarization resistance decrease, while the shape remains similar. At 715 °C it is possible to see that the Gerischer arc individuated at low frequencies, doesn't close its trajectory, but it remains open. At 765 °C the overall polarization resistance decreases its magnitude and from this temperature, the curve follows its trajectory to form a closed shape. From a quantitative point of view, the polarization resistances obtained with both the electrode configurations are extremely lower compared to the values achieved using the air atmosphere. As seen before, the nanofiber-based LSM/GDC electrode at 815 °C in the air is 1.4 Ωcm^2, while it is 1.08 Ωcm^2 with the powder-based LSM/GDC electrode. At the same operative temperature, the polarization resistance obtained in methane with both the powder and nanofiber-based electrode is 0.15 Ωcm^2, so ten times lower compared to the air results. At 865 °C the result is even better since with both the electrode architectures the polarization resistance is 0.04 Ωcm^2, which is a value around twenty times lower compared to the air results of the same electrode. The same behavior is reported by Sandoval et al., where the $La_{0.5}Sr_{1.5}MnO_4$ symmetrical cell has been tested both in air and wet hydrogen, obtaining respectively a polarization resistance of 1.2 Ωcm^2 and

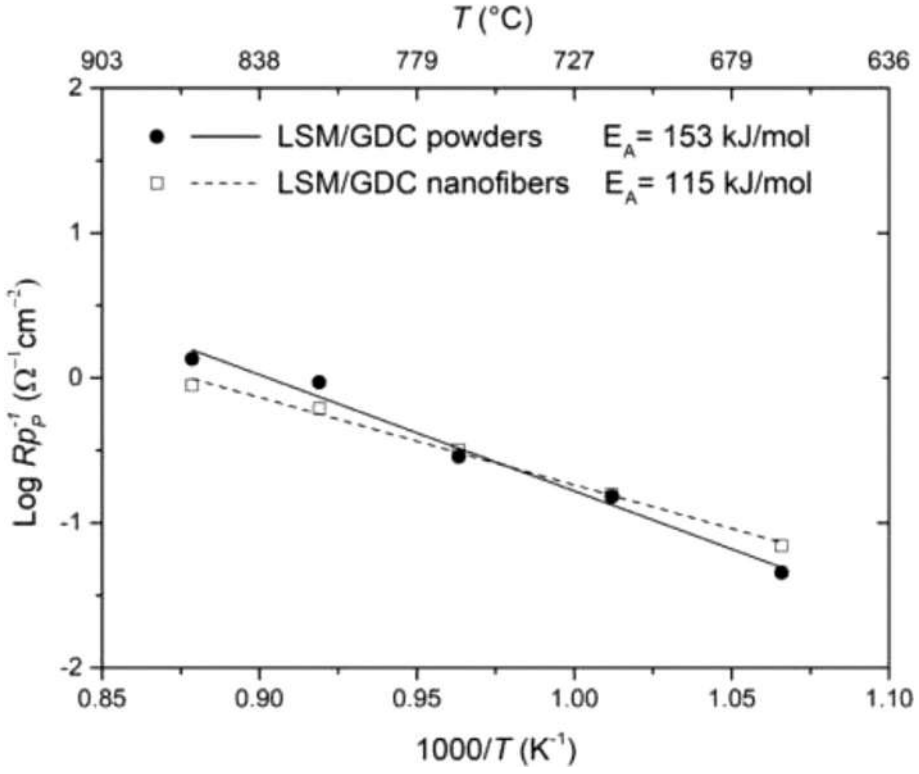

Fig. 7. 1/Rp vs 1000/T of -□- LSM/GDC nanofiber-based and -·- LSM/GDC powder-based electrode, tested in air.

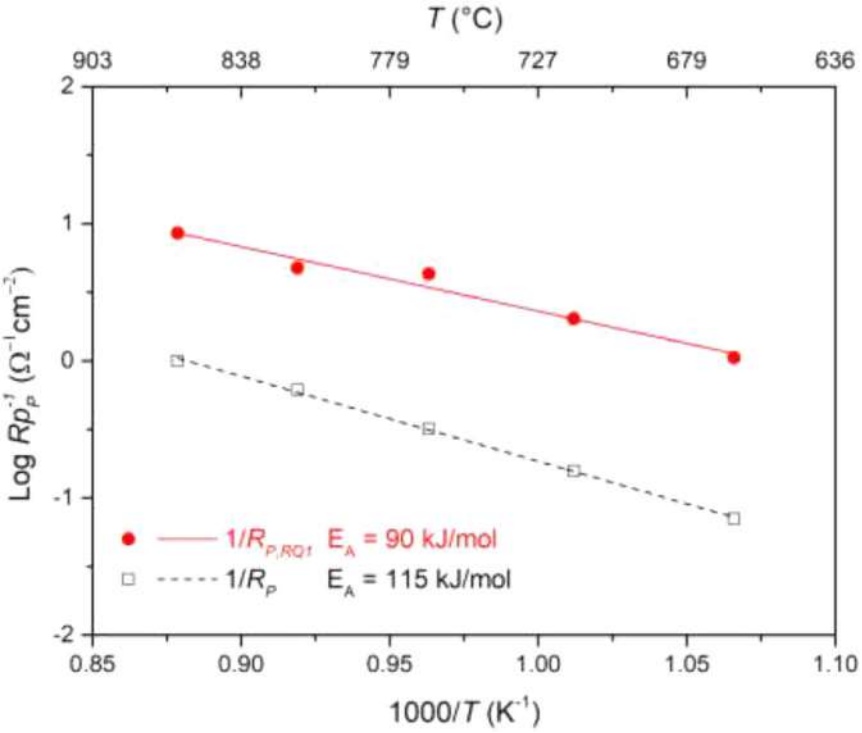

Fig. 8. Arrhenius plot of the ECs elements used to fit the LSM/GDC nanofiber-based electrode. Rp evaluated in air atmosphere. -□- overall R_P; -·- $R_{P,RQ1}$.

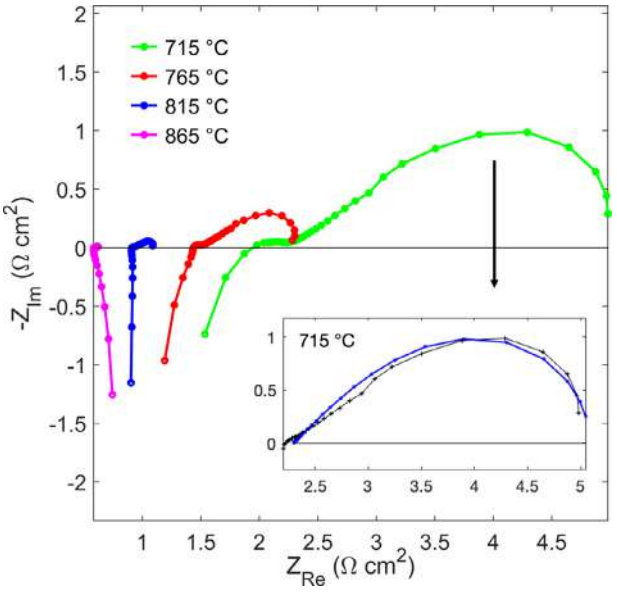

Fig. 9. Nyquist plots of the EIS results obtained with the 30 μm thick nanofiber-based LSM/GDC electrode in methane atmosphere at operating temperatures from 715 to 865 °C. Inset: Nyquist at 715 °C, -·- experimental data; -□- fitting through the Rs-G equivalent circuit model.

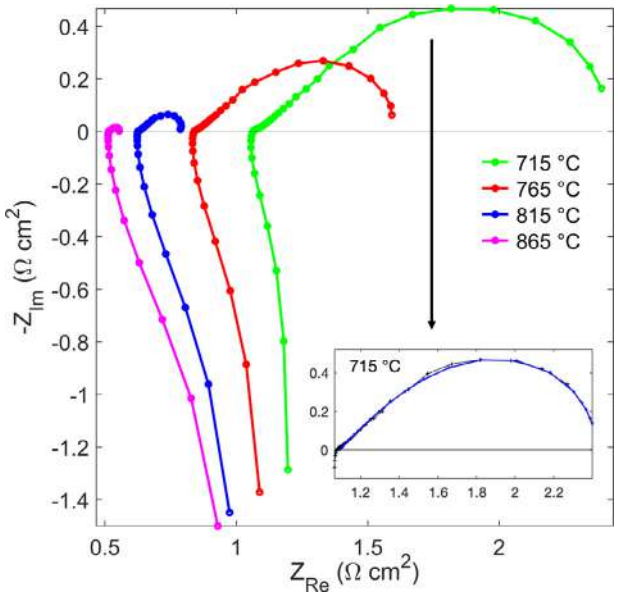

Fig. 10. Nyquist plots of the EIS results obtained with the 70 μm thick powder-based LSM/GDC electrode in methane atmosphere at operating temperatures from 715 to 865 °C. Inset: Nyquist at 715 °C, -·- experimental data; -□- fitting through the Rs-G equivalent circuit model.

0.57 Ωcm^2 [17]. Furthermore, the polarization resistances reported in Figs. 9 and 10 are better also compared to literature values concerning the CH_4 as feedstock. Wang et al. investigated a composite anode made with GDC and Nickel, which is considered as the state of the art metal for anode application, achieving a polarization resistances of 3.05 Ωcm^2 at 800 °C in a 97% of methane and 3% of water [59]. Analyzing the spectra from a qualitative point of view, the shapes of EIS experimental data reported in the Nyquist plot in Figs. 9 and 10, remind the typical Gerisher element. This behavior is quite common for GDC-based electrodes, as confirmed by several examples reported in the literature. Cho et al. performed an EIS test on $SrTiO_{3-\delta}$-GDC in a hydrogen atmosphere and the Nyquist shape reflects a Gerischer behavior [60]. Nenning et al. tested a Ni/GDC composite anode in a hydrogen atmosphere achieving the Gerischer arc as well [61]. The possible explanation may be found in the conductive properties of the GDC. Indeed, when the GDC is exposed to the air atmosphere, its fluorite structure allows the conduction of oxygen ions at operating temperatures even lower

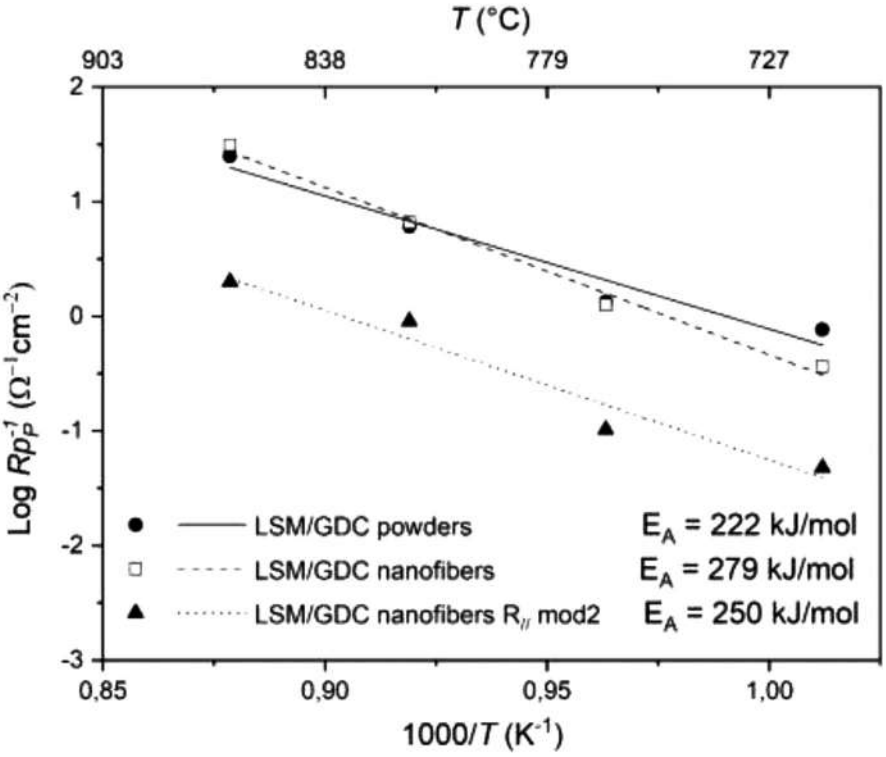

Fig. 11. Arrhenius plot of polarization resistance of -□- LSM/GDC nanofiber-based electrode, tested in methane; -•- LSM/GDC powder-based electrode, tested in methane; ••▲•• LSM/GDC nanofiber $R_{//}$ calculated through Mod2.

compared to ones generally used for the YSZ. Otherwise, when the GDC is exposed to a reducing atmosphere, poor electronic conduction is activated and it becomes an MIEC [62]. Furthermore, as reported in Fig. 4 the LSM modified its structure arrangement from the ABO_3 single perovskite structure, achieved after the preparation process, the Ruddlesden-Popper double perovskite after the exposition to methane atmosphere. The RP crystal structure provides a higher open framework compared to the single perovskite and due to this feature, it allows the accommodation of hyper stoichiometric oxide ions, which may permit poor ionic conduction. Thus, the LSM when exposed to a reducing atmosphere behaves like mixed ionic and electronic conductors as well [9,63,64]. The explanation just reported may explain the Nyquist shape reported in Figs. 5, 6, 9, 10. The LSM/GDC electrodes tested as cathodes may behave as, respectively pure electronic and pure ionic conductors, which are not able to extend the electrochemical reaction in the whole electrode thickness; on the contrary when the LSM/GDC electrodes are tested as anodes in methane atmosphere, both the materials achieve MIEC properties allowing the reaction process in the whole electrode volume. The different behaviors just described are reflected also in the widely lower polarization resistances achieved in anode configuration compared to cathode one.

In Fig. 11 the reverse of the polarization resistances of the LSM/GDC 30 μm thick nanofiber and 70 μm thick powder-based electrode are reported in an Arrhenius plot, within the activation energies which are respectively 297 kJ/mol and 222 kJ/mol. It is possible to see that the major differences between the two architectures are detected at 715 °C, while at higher temperatures the results are almost overlapped which underlines the good repeatability of the results. Furthermore, compared to the results acquired in the air atmosphere, the activation energies are quite higher, while the polarization resistances are widely lower.

In Fig. 10 the reverse of the polarization resistance ($R_{p//}{}^{-1}$) related to the $R_{//}$ (which is referred to the R_2 of Fig. 1b) given by the Mod2 used to fit the nanofiber LSM/GDC electrode is reported as well. As reported above, the GDC acts as a mixed ionic and electronic conductor once exposed to a reducing atmosphere, so both the electrode and electrolyte start to conduct electrons.

Table 1.
Resistance values of the elements that appear in Mod2 and the calculated total polarization resistance. All values are normalized to the surface area. The experimental data derives from the nanofiber composite electrode measurements.

Element	715 °C	765 °C	815 °C	865 °C
R_1 (Ωcm^2)	2.4	2.2	3.8	7.0
R_G (Ωcm^2)	3.6	1.1	6.0	482.0
$R_{//}$ (Ωcm^2)	20.9	9.7	1.1	0.5
R_p (Ωcm^2)	4.7	2.5	1.0	0.6

In Table 1 the resistances of the different EC elements as well as the total polarization resistance are reported for each investigated temperature.

In Fig. 1 as well as Fig. 10 and Table 1 it is possible to identify the two parallel pathways for electrons and ions which are available in the investigated cells and which are schematized by the EC Mod2. The first pathway is the electrochemical process, which is represented by the RQ-G elements, while the second one is the short-circuited electrolyte, described by $R_{//}$. As matter of fact, when an electric circuit is provided by different components placed in parallel, the electrical current is more favorable to flow in the pathway which offers a lower resistance. In the Mod2 EC, the relative currents through the electrochemical and short-circuited pathway are related to the value of R_1 and $R_{//}$. At lower temperatures, the resistance of R_1 is widely lower compared to $R_{//}$, and the electrochemical pathway results to be the more favorable. Furthermore, at these temperatures the GDC electronic conductivity has higher activation energy compared to the GDC ionic conductivity, thus the reduction of GDC is not sufficiently performed to generate a short-circuit. On the contrary, at the higher temperatures, the GDC reduction is at an advanced stage, and the value of

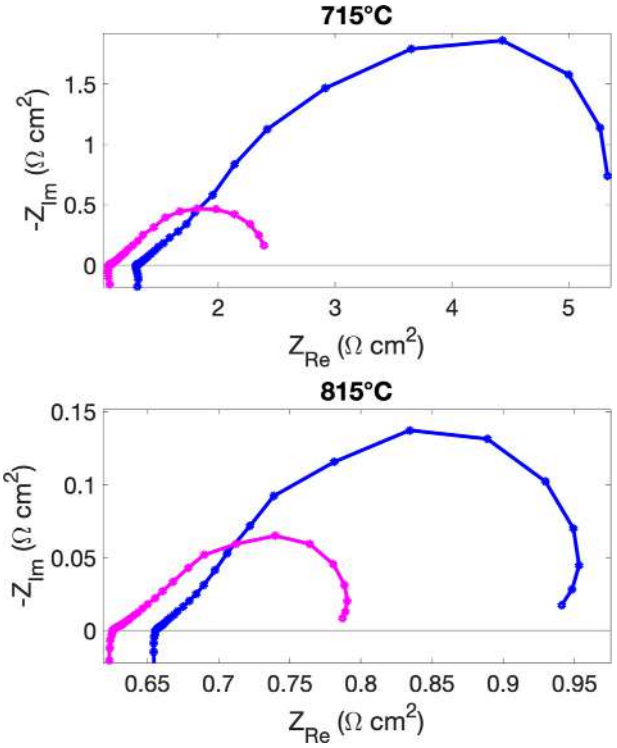

Fig. 12. Nyquist plots obtained at 715 °C and 815 °C in methane atmosphere employing LSM/GDC powder-based electrodes prepared with different thicknesses. -·- 70 μm thick LSM/GDC powder electrode (already reported in Fig. 10); -·- 30 μm thick LSM/GDC powder electrode.

R_1 is widely higher compared to $R_{//}$, so the short-circuited pathway becomes more favorable. For this reason, since the electrical current is not directed exclusively to the electrochemical activity of the electrode, the electrochemical performance cannot be considered intrinsic of the material. Furthermore, the measured activation energy is 250 kJ/mol for the electronic conductivity, which is in agreement with the literature value of 248 kJ/mol [65].

The very low polarization resistances measured from the impedance test are affected by the parallel pathway, so they do not reflect the pure electrochemical activity. However, assuming that the electronic pathway has no complex contribution to the imaginary part, it is expected that the Nyquist shape, e.g. the Gerischer element, is not affected by the short-circuit so reflects the electrode processes involved in the EC pathway. However, the results indicate the importance to employ a pure ionic conductor as an electrolyte, for example, a multilayer electrolyte based on zirconia coated with GDC on both sides.

3.5. Effect of the electrode thickness

Fig. 12 shows the Nyquist plots acquired between 715 and 815 °C with the 70 μm thick powder-based LSM/GDC electrode (already reported in Fig. 10) and the 40 μm thick powder-based LSM/GDC electrode. The experimental data are acquired in the methane atmosphere. In both cases, the shape reported in the Nyquist plots recalls the typical Gerischer behavior, as seen in Figs. 9 and 10, but it is possible to underline some differences between the two architectures. Indeed, the Gerischer arc obtained with the 70 μm thick powder electrode has a shape that is more stable with the temperature, as already reported in Fig. 10. From 715 to 865 °C the polarization resistance decreases but the shape does not shrink and remains well defined. On the other hand, the 30 μm thick powder electrode reflects the Gerischer behavior as well, but looking more deeply in the experimental data, the shape obtained is more similar to a Finite-Length-Gerischer (FLG) element. The FLG feature is individuated in electrodes which show mixed ionic and electronic properties, and so they allow the electrochemical reaction process in the whole volume of the electrode, but the electrode thickness results too thin. Therefore, the thickness of the electrode is smaller than that required by the electrochemical process and this limitation is reflected in the impedance spectra, which appear as a hybrid between the Gerischer and the Finite-Length-Warburg element [36,66]. For this reason, in the 30 μm thick powder-based electrode some thickness limitations take place, reflecting this hybrid shape.

3.6. Carbon deposition

Electrodes employed at the anode side in a methane atmosphere suffer carbon coke deposition. This is an undesired and quick phenomenon. According to the literature, carbon coking can be detected after less than 10 operating hour [67,68]. To evaluate this phenomenon, the electrodes are characterized through XPS. This characterization is performed after the EIS test in methane as well as in air, for comparison. To have significant results, tests in methane are run for 24 h.

The first, qualitative, result is that the cells tested in methane and those tested in air do not show any color difference: the gold paste used as the current collector does not show any black spots, which are clear symptoms of carbon formation. XPS measurements have been carried out onto the LSM/GDC electrode after using it as a cathode, and as an anode directly fueled with methane (The electrode in cathode configuration is not expected to show any carbon coke formation and represents a good term of comparison). The second XPS measurement is carried out onto the LSM/GDC electrode which is constantly fueled by methane until the room temperature (i.e. even after the conclusion of the electrochemical tests). In Fig. 13 the C1s XPS spectra of the two analyzed LSM/GDC electrodes are represented. The two peaks are very similar and no significant differences are observed. A quantitative analysis is carried out as well, focusing on the carbon quantities over the electrode. The quantities of carbon detected in each sample are very similar: the electrode analyzed after the air application shows 44% of C1s while the electrode employed in methane atmosphere reports 50% of C1s. These percentages are referred to the total surface composition. Other elements detected are gold, used as a current collector, and oxygen chemisorbed on the surface. During the air configuration, after the electrochemical test, the sample is let to decrease in air (from 865 °C to room one), and no carbon is expected. The similarity between the two XPS spectra suggests that no relevant amount of carbon coke is produced during the electrochemical activity in the methane atmosphere by LSM/GDC composite electrode. A further suggestion regarding the good stability of the LSM/GDC anode toward carbon deposition, is given by the comparison with the XPS atomic composition obtained, under the same operating conditions, on a different GDC-based composite materials: indeed, it was observed, in some cases that, after an electrochemical test in methane, about 65–70% at. C was present.

4. Conclusions

In this work, symmetrical cells made with nanofiber-based LSM/GDC electrodes and powder-based LSM/GDC electrodes are investigated. The LSM/GDC nanofiber-based electrode does not show significant structural and electrochemical differences with the LSM/GDC powder-based electrode, due to the grinding process used assembly the symmetrical cells. This phenomenon suggests that the improvement of the electrochemical performances is mostly related to the differences of the surface between nanofiber and powder morphology. The LSM/GDC electrodes show good

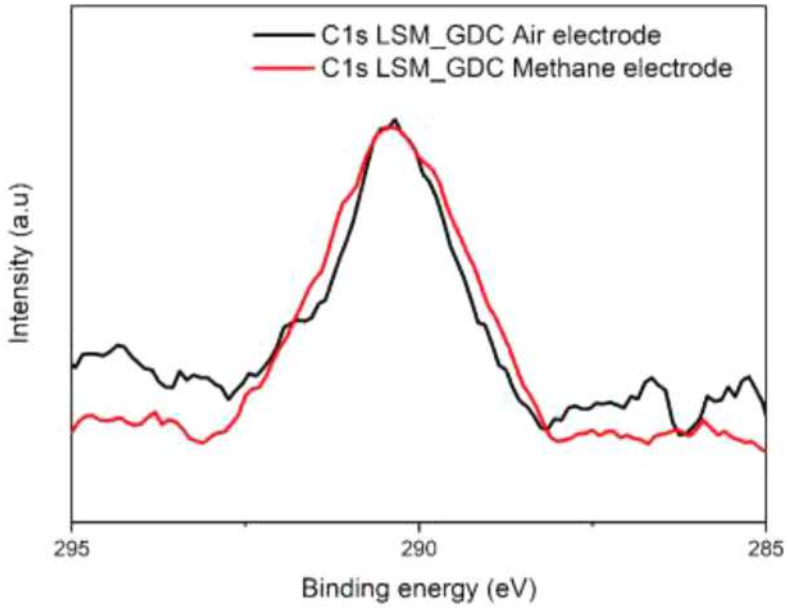

Fig. 13. C1s XPS pattern of LSM/GDC electrode after EIS tests. Black: spectrum recorded in air. Red: spectrum recorded after exposure to methane.

structural stability in the oxidizing and reduction atmosphere. The XRD measurements identify a change of the LSM crystal structure from the single perovskite obtained after the preparation process to the RP structure achieved after the exposition to the methane atmosphere. However, this transition is reversible after a re-oxidation. The LSM/GDC electrodes show a good electrochemical performance in air, consistent with literature data, reporting a polarization resistance of 1.6 Ωcm^2 at 815 °C. Furthermore, the LSM/GDC electrodes show an even better electrochemical performance once tested as an anode, in the methane atmosphere. The polarization resistance achieved at 815 °C is 0.15 Ωcm^2, ten times lower compared to the cathode application. These very low values obtained in the methane atmosphere may find an explanation by considering the possibility of a reduction of GDC. This can lead to the presence of a parallel electron conductive pathway that may not affect the shape and the description of the electrochemical impedance phenomena, but it may influence the measured R_p. Further investigation will be performed to better understand better this eventuality. In other cases, in fact, a contribution to the decrease of polarization resistance was attributed to the presence of C-nanoparticles whose formation was consequent to the use of methane. In this case XPS allowed to verify the absence of relevant deposition of carbon (no significant differences between surface composition, particularly C at.%, are observed after the use of the electrode in the air or methane).

Beside resistance against C-deposition, a significant advantage of the LSM/GDC electrodes is the possibility to use them both under oxidizing and reducing atmosphere. This could pave the way to the use of these electrodes in reversible and symmetric Solid Oxide Cells.

Declaration of Competing Interest

The authors declare that they have no known competing financial interests or personal relationships that could have appeared to influence the work reported in this paper.

Declaration of Competing Interest

The authors declare no conflict of interest.

Credit authorship contribution statement

Caterina Sanna: Investigation, Writing – original draft. **Enrico Squizzato:** Data curation, Visualization. **Paola Costamagna:** Resources, Writing – review & editing. **Peter Holtappels:** Formal analysis, Methodology. **Antonella Glisenti:** Conceptualization, Supervision.

Acknowledgments

C.S. and P.C. at the University of Genoa (Italy) acknowledge financial support from the San Paolo Project 'COELUS - Production of renewable fuel by CO-ELectrolysis and reUSe of carbon dioxide' (ID ROL 32604).

References

[1] K. Ahmed, K. Föger, Perspectives in solid oxide fuel cell-based microcombined heat and power systems, J. Electrochem. Energy Convers. Storage 14 (2017) 1–12, doi:10.1115/1.4036762.
[2] A. Greco, A. Sorce, R. Littwin, P. Costamagna, L. Magistri, Reformer faults in SOFC systems: experimental and modeling analysis, and simulated fault maps, Int. J. Hydrog. Energy 39 (2014) 21700–21713, doi:10.1016/j.ijhydene.2014.09.063.
[3] T. Wei, P. Qiu, J. Yang, L. Jia, B. Chi, J. Pu, J. Li, High-performance direct carbon dioxide-methane solid oxide fuel cell with a structure-engineered double-layer anode, J. Power Sources 484 (2021) 229199, doi:10.1016/j.jpowsour.2020.229199.
[4] P. Aguiar, C.S. Adjiman, N.P. Brandon, Anode-supported intermediate temperature direct internal reforming solid oxide fuel cell. I: model-based steady-state performance, J. Power Sources 138 (2004) 120–136, doi:10.1016/j.jpowsour.2004.06.040.
[5] J. Xu, C.M.Y. Yeung, J. Ni, F. Meunier, N. Acerbi, M. Fowles, S.C. Tsang, Methane steam reforming for hydrogen production using low water-ratios without carbon formation over ceria coated Ni catalysts, Appl. Catal. A Gen. 345 (2008) 119–127, doi:10.1016/j.apcata.2008.02.044.
[6] L.P. Teh, H.D. Setiabudi, S.N. Timmiati, M.A.A. Aziz, N.H.R. Annuar, N.N. Ruslan, Recent progress in ceria-based catalysts for the dry reforming of methane: a review, Chem. Eng. Sci. 242 (2021) 116606, doi:10.1016/j.ces.2021.116606.
[7] S. Vecino-Mantilla, P. Gauthier-Maradei, M. Huvé, J.M. Serra, P. Roussel, G.H. Gauthier, Nickel exsolution-driven phase transformation from an n=2 to an n=1 ruddlesden-popper manganite for methane steam reforming reaction in SOFC conditions, ChemCatChem 11 (2019) 4631–4641, doi:10.1002/cctc.201901002.
[8] S. Vecino-Mantilla, E. Quintero, C. Fonseca, G.H. Gauthier, P. Gauthier-Maradei, Catalytic steam reforming of natural gas over a new Ni exsolved Ruddlesden-Popper manganite in SOFC anode conditions, ChemCatChem 12 (2020) 1453–1466, doi:10.1002/cctc.201902306.

[9] S. Vecino-Mantilla, P. Simon, M. Huvé, G. Gauthier, P. Gauthier-Maradei, Methane steam reforming in water-deficient conditions on a new Ni-exsolved Ruddlesden-Popper manganite: coke formation and H2S poisoning, Int. J. Hydrog. Energy 45 (2020) 27145–27159, doi:10.1016/j.ijhydene.2020.07.065.

[10] E. Zhao, X. Liu, L. Liu, H. Huo, Y. Xiong, Effect of $La_{0.8}Sr_{0.2}Co_{0.2}Fe_{0.8}O_{3-\delta}$ morphology on the performance of composite cathodes, Prog. Nat. Sci. Mater. Int. 24 (2014) 24–30, doi:10.1016/j.pnsc.2014.01.008.

[11] J. Parbey, Q. Wang, J. Lei, M. Espinoza-Andaluz, F. Hao, Y. Xiang, T. Li, M. Andersson, High-performance solid oxide fuel cells with fiber-based cathodes for low-temperature operation, Int. J. Hydrog. Energy 45 (2020) 6949–6957, doi:10.1016/j.ijhydene.2019.12.125.

[12] M. Zhi, N. Mariani, R. Gemmen, K. Gerdes, N. Wu, Nanofiber scaffold for cathode of solid oxide fuel cell, Energy Environ. Sci. 4 (2011) 417–420, doi:10.1039/c0ee00358a.

[13] Y. Chen, Y. Bu, Y. Zhang, R. Yan, D. Ding, B. Zhao, M. Liu, A highly efficient and robust nanofiber cathode for solid oxide fuel cells, Adv. Energy Mater. 7 (6) (2017) 1–7, doi:10.1002/aenm.201601890.

[14] A. Enrico, W. Zhang, M. Lund Traulsen, E.M. Sala, P. Costamagna, P. Holtappels, $La_{0.6}Sr_{0.4}Co_{0.2}Fe_{0.8}O_{3-\delta}$ nanofiber cathode for intermediate-temperature solid oxide fuel cells by water-based sol-gel electrospinning: synthesis and electrochemical behaviour, J. Eur. Ceram. Soc. 38 (2018) 2677–2686, doi:10.1016/j.jeurceramsoc.2018.01.034.

[15] E. Squizzato, C. Sanna, A. Glisenti, P. Costamagna, Structural and catalytic characterization of $La_{0.6}Sr_{0.4}MnO_3$ nanofibers for application in direct methane intermediate temperature solid oxide fuel cell anodes, Energies 14 (2021) 3602.

[16] Y. Jeon, J. ha Myung, S. hoon Hyun, Y. gun Shul, J.T.S. Irvine, Corn-cob like nanofibres as cathode catalysts for an effective microstructure design in solid oxide fuel cells, J. Mater. Chem. A 5 (2017) 3966–3973, doi:10.1039/c6ta08692f.

[17] M.V. Sandoval, C. Pirovano, E. Capoen, R. Jooris, F. Porcher, P. Roussel, G.H. Gauthier, In-depth study of the Ruddlesden-Popper LaxSr2−xMnO4±Δ family as possible electrode materials for symmetrical SOFC, Int. J. Hydrog. Energy 42 (2017) 21930–21943, doi:10.1016/j.ijhydene.2017.07.062.

[18] J.C. Ruiz-Morales, J. Canales-Vázquez, J. Peña-Martínez, D.M. López, P. Núñez, On the simultaneous use of $La_{0.75}Sr_{0.25}Cr_{0.5}Mn_{0.5}O_{3-\delta}$ as both anode and cathode material with improved microstructure in solid oxide fuel cells, Electrochim. Acta 52 (2006) 278–284, doi:10.1016/j.electacta.2006.05.006.

[19] D.M. Bastidas, S. Tao, J.T.S. Irvine, A symmetrical solid oxide fuel cell demonstrating redox stable perovskite electrodes, J. Mater. Chem. 16 (2006) 1603–1605, doi:10.1039/b600532b.

[20] J. Xiong, Y. Liu, A. Li, L. Wei, L. Wang, X. Qin, J. Yu, Mass production of high-quality nanofibers via constructing pre-Taylor cones with high curvature on needleless electrospinning, Mater. Des. 197 (2021) 109247, doi:10.1016/j.matdes.2020.109247.

[21] L. Wei, R. Sun, C. Liu, J. Xiong, X. Qin, Mass production of nanofibers from needleless electrospinning by a novel annular spinneret, Mater. Des. 179 (2019) 107885, doi:10.1016/j.matdes.2019.107885.

[22] P. Mikeš, D.A. Baker, A. Uhlin, D. Lukáš, E. Kuželová-Košťáková, A. Vidrich, J. Valtera, B. Kopřivová, N. Asatiani, L. Salmén, P. Tomani, The mass production of lignin fibres by means of needleless electrospinning, J. Polym. Environ. 29 (2021) 2164–2173, doi:10.1007/s10924-020-02029-7.

[23] S. Omer, L. Forgách, R. Zelkó, I. Sebe, Scale-up of electrospinning: market overview of products and devices for pharmaceutical and biomedical purposes, Pharmaceutics 13 (2021) 1–21, doi:10.3390/pharmaceutics13020286.

[24] A. Enrico, B. Aliakbarian, A. Lagazzo, A. Donazzi, R. Botter, P. Perego, P. Costamagna, Parameter optimization for the electrospinning of La1−xSrxCo1−yFeyO3−Δ fibers for IT-SOFC electrodes, Fuel Cells 17 (2017) 415–422, doi:10.1002/fuce.201600190.

[25] C. Sanna, W. Zhang, P. Costamagna, P. Holtappels, Synthesis and electrochemical characterization of electrospun nanofiber cathodes for intermediate- temperature solid oxide fuel cells, Int. J. Hydrog. Energy (2020) 1–14, doi:10.1016/j.ijhydene.2020.11.216.

[26] C. Marcilly, P. Courty, B. Delmon, Preparation of highly dispersed mixed oxides and oxide solid solutions, J. Am. Ceram. Soc. 53 (1970) 56, doi:10.1111/j.1151-2916.1970.tb12003.x.

[27] J.F.M. C.D. Wanger, W.M. Riggs, L.E. Davis, J.F. Moulder, G.E. Muilenberg, Handbook of X-ray Photoelectron Spectroscopy Perkin-Elmer Corporation, 1979, pp. 190–195.

[28] Image-J Software. https://imagej.net.

[29] C.T. Rueden, J. Schindelin, M.C. Hiner, B.E. DeZonia, A.E. Walter, E.T. Arena, K.W. Eliceiri, ImageJ2: imageJ for the next generation of scientific image data, BMC Bioinform. 18 (2017) 1–26, doi:10.1186/s12859-017-1934-z.

[30] E. Barsoukov, J.R. Macdonald, Impedance Spectroscopy: Theory, Experiment, and Applications, 2nd edition, Wiley, 2022. ISBN 0-471-64749-7.

[31] T. Suzuki, M. Awano, P. Jasinski, V. Petrovsky, H.U. Anderson, Composite (La, Sr)MnO3-YSZ cathode for SOFC, Solid State Ion. 177 (2006) 2071–2074, doi:10.1016/j.ssi.2005.12.016.

[32] H.V. Napporn Teko, W. Holade Yaovi, K. Boniface, M. Shigenori, M. Kurt, E. Bernd, Electrochemical measurement methods and characterization on the cell level, Fuel Cells Hydrog. (2018) 175–214, doi:10.1016/B978-0-12-811459-9.00009-8.

[33] B. Hirschorn, M.E. Orazem, B. Tribollet, V. Vivier, I. Frateur, M. Musiani, Determination of effective capacitance and film thickness from constant-phase-element parameters, Electrochim. Acta 55 (2010) 6218–6227, doi:10.1016/j.electacta.2009.10.065.

[34] V. Yousefi, D. Mohebbi-kalhori, A. Samimi, Equivalent electrical circuit modeling of ceramic-based microbial fuel cells using the electrochemical impedance spectroscopy (EIS) analysis, J. Renew. Energy Environ. 6 (2019) 21–28.

[35] P. Costamagna, E.M. Sala, W. Zhang, M. Lund Traulsen, P. Holtappels, Electrochemical impedance spectroscopy of $La_{0.6}Sr_{0.4}Co_{0.2}Fe_{0.8}O_{3-\delta}$ nanofiber cathodes for intermediate temperature-solid oxide fuel cell applications: a case study for the 'depressed' or 'fractal' Gerischer element, Electrochim. Acta 319 (2019) 657–671, doi:10.1016/j.electacta.2019.06.068.

[36] J. Nielsen, T. Jacobsen, M. Wandel, Impedance of porous IT-SOFC LSCF:CGO composite cathodes, Electrochim. Acta. 56 (2011) 7963–7974, doi:10.1016/j.electacta.2011.05.042.

[37] T. Jacobsen, P.V. Hendriksen, S. Koch, Diffusion and conversion impedance in solid oxide fuel cells, Electrochim. Acta 53 (2008) 7500–7508, doi:10.1016/j.electacta.2008.02.019.

[38] H. Li, Y. Song, M. Xu, W. Wang, R. Ran, W. Zhou, Z. Shao, Exsolved alloy nanoparticles decorated Ruddlesden – Popper perovskite as sulfur-tolerant anodes for solid oxide fuel cells, Ener Fuels 34 (9) (2020) 11449–11457, doi:10.1021/acs.energyfuels.0c02228.

[39] W.L. Miao, J. Hou, Z. Gong, Z. Jin, W. Liu, A high-performance cobalt-free Ruddlesden-Popper phase cathode La1·2Sr0·8Ni0·6Fe0·4O4+Δ for low temperature proton-conducting solid oxide fuel cells. *International Journal of Hydrogen Energy*, Int. J. Hydrog. Energy 44 (14) (2018) 7531–7537, doi:10.1016/j.ijhydene.2019.01.255.

[40] U. Boulahya, K. Muñoz-Gil, D. Gómez-Herrero, A. Azcondo, M.T. Amador, $Eu_2SrCo_{1.5}Fe_{0.5}O_7$ a new promising Ruddlesden– Popper member as a cathode component for intermediate temperature solid oxide fuel cells, J. Mater. Chem. A 7 (2019) 5601–5611, doi:10.1039/c8ta11254a.

[41] P.G.M. Sebastian Vecino-Mantilla, P. Simon, M. Huve, G. Gauthier, Methane steam reforming in water-deficient conditions on a new Ni-exsolved Ruddlesden- Popper manganite: coke formation and H_2S poisoning, Int. J. Hydrog. Energy 5 (2020) 27145–27159, doi:10.1016/j.ijhydene.2020.07.065.

[42] P. Costamagna, C. Sanna, A. Campodonico, E.M. Sala, R. Sažinas, P. Holtappels, Electrochemical impedance spectroscopy of electrospun $La_{0.6}Sr_{0.4}Co_{0.2}Fe_{0.8}O_{3-\Delta}$ nanorod cathodes for intermediate temperature – solid oxide fuel cells, Fuel Cells 19 (2019) 472–483, doi:10.1002/fuce.201800205.

[43] M. Cannarozzo, A. Del Borghi, P. Costamagna, Simulation of mass transport in SOFC composite electrodes, J. Appl. Electrochem. 38 (2008) 1011–1018, doi:10.1007/s10800-008-9527-1.

[44] E.P. Murray, T. Tsai, S.A. Barnett, Oxygen transfer processes in (La,Sr)MnO_3/Y_2O=-stabilized ZrO_2 cathodes: an impedance spectroscopy study, Solid State Ion. 110 (1998) 235–243, doi:10.1016/s0167-2738(98)00142-8.

[45] E. Siebert, A. Hammouche, M. Kleitz, Impedance spectroscopy analysis of La1 - xSritxMnO_3-yttria-stabilized zirconia electrode kinetics, Electrochim. Acta 40 (1995) 1741–1753, doi:10.1016/0013-4686(94)00361-4.

[46] M.J.L. Østergård, M. Mogensen, AC impedance study of the oxygen reduction mechanism on $La_{1-x}Sr_xMnO_3$ in solid oxide fuel cells, Electrochim. Acta 38 (1993) 2015–2020, doi:10.1016/0013-4686(93)80334-V.

[47] M. Juhl, S. Primdahl, C. Manon, M. Mogensen, Performance/structure correlation for composite SOFC cathodes, J. Power Sources 61 (1996) 173–181, doi:10.1016/S0378-7753(96)02361-0.

[48] P. Costamagna, P. Holtappels, C. Sanna, Metal oxide nanofiber-based electrodes in solid oxide fuel cells, Met. Oxide Based Nanofibers Appl. (2022) Elseviern.d.

[49] X. Luo, Y. Yang, Y. Yang, D. Tian, X. Lu, Y. Chen, Q. Huang, B. Lin, Reduced-temperature redox-stable LSM as a novel symmetrical electrode material for SOFCs, Electrochim. Acta 260 (2018) 121–128, doi:10.1016/j.electacta.2017.11.071.

[50] S.P. Jiang, W. Wang, Novel structured mixed ionic and electronic conducting cathodes of solid oxide fuel cells, Solid State Ion. 176 (2005) 1351–1357, doi:10.1016/j.ssi.2005.03.011.

[51] S. Wang, X. Lu, M. Liu, Electrocatalytic properties of $La_{0.9}Sr_{0.1}$ MnO_3-based electrodes for oxygen reduction, J. Solid State Electrochem. 6 (2002) 384–390, doi:10.1007/s10008-001-0250-7.

[52] S.P. Jiang, Development of lanthanum strontium cobalt ferrite perovskite electrodes of solid oxide fuel cells – A review, Int. J. Hydrog. Energy 44 (2019) 7448–7493, doi:10.1016/j.ijhydene.2019.01.212.

[53] S. Sunde, Monte Carlo simulations of polarization resistance of composite electrodes for solid oxide fuel cells, J. Electrochem. Soc. 143 (1996) 1930–1939, doi:10.1149/1.1836927.

[54] P. Costamagna, P. Costa, V. Antonucci, Micro-modelling of solid oxide fuel cell electrodes, Electrochim. Acta 43 (1998) 375–394, doi:10.1016/S0013-4686(97)00063-7.

[55] M.J. Jørgensen, M. Mogensen, Impedance of solid oxide fuel cell LSM/YSZ composite cathodes, J. Electrochem. Soc. 148 (2001) A433, doi:10.1149/1.1360203.

[56] S.P. Jiang, Development of lanthanum strontium manganite perovskite cathode materials of solid oxide fuel cells: a review, J. Mater. Sci. 43 (21) (2008) 6799–6833, doi:10.1007/s10853-008-2966-6.

[57] S. Wang, Y. Jiang, Y. Zhang, J. Yan, W. Li, Promoting effect of YSZ on the electrochemical performance of YSZ + LSM composite electrodes, Solid State Ion. 113–115 (1998) 291–303, doi:10.1016/s0167-2738(98)00379-8.

[58] L. Fan, Y. Xiong, L. Liu, Y. Wang, H. Kishimoto, K. Yamaji, T. Horita, Performance of $Gd_{0.2}Ce_{0.8}O_{1.9}$ infiltrated $La_{0.2}Sr_{0.8}TiO_3$ nanofiber scaffolds as anodes for solid oxide fuel cells, J. Power Sources 265 (2014) 125–131, doi:10.1016/j.jpowsour.2014.04.109.

[59] W. Wang, S.P. Jiang, A.I.Y. Tok, L. Luo, GDC-impregnated Ni anodes for direct utilization of methane in solid oxide fuel cells, J. Power Sources 159 (2006) 68–72, doi:10.1016/j.jpowsour.2006.04.051.

[60] S. Cho, D.E. Fowler, E.C. Miller, J.S. Cronin, K.R. Poeppelmeier, S.A. Barnett, Fe-substituted $SrTiO_{3-\delta}$-$Ce_{0.9}Gd_{0.1}O_2$ composite anodes for solid oxide fuel cells, Energy Environ. Sci. 6 (2013) 1850–1857, doi:10.1039/c3ee23791e.
[61] A. Nenning, C. Bischof, J. Fleig, M. Bram, A.K. Opitz, The relation of microstructure, materials properties and impedance of SOFC electrodes: a case study of Ni/GDC anodes, Energies 13 (2020) 5–9, doi:10.3390/en13040987.
[62] N. Mahato, A. Banerjee, A. Gupta, S. Omar, K. Balani, Progress in material selection for solid oxide fuel cell technology: a review, Prog. Mater. Sci. 72 (2015) 141–337, doi:10.1016/j.pmatsci.2015.01.001.
[63] G. Amow, S.J. Skinner, Recent developments in Ruddlesden-Popper nickelate systems for solid oxide fuel cell cathodes, J. Solid State Electrochem. 10 (2006) 538–546, doi:10.1007/s10008-006-0127-x.
[64] A. Manthiram, J.H. Kim, Y.N. Kim, K.T. Lee, Crystal chemistry and properties of mixed ionic-electronic conductors, J. Electroceramics. 27 (2011) 93–107, doi:10.1007/s10832-011-9635-x.
[65] C. Chatzichristodoulou, P.V. Hendriksen, Electronic conductivity of $Ce_{0.9}Gd_{0.1}O_{1.95-\delta}$ and $Ce_{0.8}Pr_{0.2}O_{2-\delta}$: Hebb-Wagner polarisation in the case of redox active dopants and interference, Phys. Chem. Chem. Phys. 13 (2011) 21558–21572, doi:10.1039/c1cp21824g.
[66] J. Nielsen, J. Hjelm, Impedance of SOFC electrodes: a review and a comprehensive case study on the impedance of LSM:YSZ cathodes, Electrochim. Acta 115 (2014) 31–45, doi:10.1016/j.electacta.2013.10.053.
[67] V. Alzate-restrepo, J.M. Hill, Effect of anodic polarization on carbon deposition on Ni/YSZ anodes exposed to methane, Appl. Catal. A Gen. 342 (2008) 49–55, doi:10.1016/j.apcata.2007.12.039.
[68] J. Koh, Y. Yoo, J. Park, H.C. Lim, Carbon deposition and cell performance of Ni-YSZ anode support SOFC with methane fuel, Solid State Ion. 149 (2002) 157–166.

Ringraziamenti

Questo dottorato è stato un lungo viaggio ricco di emozioni. Non scorderò mai l'emozione del primo foglio di fibre ottenuto, della prima cella testata e dei primi buoni risultati ottenuti. Dietro a tutto questo, c'è stata la delusione per i numerosi tentativi non riusciti e la paura di non riuscire a ottenere quanto nella mia testa era estremamente chiaro. Per questo, il mio primo ringraziamento voglio dedicarlo a me stessa, alla mia capacità di non mollare anche quando tutto sembrava impossibile.

Un grande ringraziamento va alla professoressa Costamagna, più semplicemente a Paola. Abbiamo iniziato questo lungo viaggio nel 2016 con una mia richiesta di tesi triennale. Da quel giorno ho avuto un sostegno costante che è passato attraverso una tesi magistrale fino ad arrivare alla fine del mio dottorato. Non posso che dirti grazie per tutto quello che hai fatto per me.

Un ringraziamento va a Peter Holtappels, che mi ha accolto per sei mesi nei suoi laboratori e ha elargito preziosissimi consigli durante tutto questo percorso. Thank you Peter!

Un sentito grazie anche a chi mi ha accompagnato durante questo dottorato, le professoresse Marcella Pani, Cristina Artini e Marilena Carnasciali. Grazie per aver guidato un ingegnere nel mondo della chimica fisica, permettendomi di conoscere ed apprezzare qualcosa che fino a quel momento era molto lontano da me. Grazie specialmente a Marcella per tutto quello che mi hai insegnato nella vita quotidiana di laboratorio e per avermi mostrato Basovizza.

Un ringraziamento speciale va alla mia famiglia, che ha permesso tutto questo. Senza il loro appoggio e il loro supporto non sarei quella che sono oggi. Sempre presente nei successi e ancora più presente nei miei insuccessi. Menzione speciale alla mia sorellina Margherita, che è riuscita a risollevarmi nel momento più buio di questo percorso. Anche da lontano, un grazie a mia nonna Talea per avermi rifocillato a dovere durante questi anni lontano da casa. Eternamente riconoscente.

Un grazie enorme alla mia amica e compagna di limoncini Sara Massardo. Supporto quotidiano in questo percorso. Grazie per essere stata una collega e poco dopo un'amica con cui condividere tutte le giornate in laboratorio tra polveri da macinare e crogioli a 300°C. In due il viaggio è sempre più semplice. Ora in laboratorio ci sarai solo tu, ma sicuro rimarrà la nostra produzione di liquori fatti in casa, il che sarà sempre solo un successo.

Un sentito grazie al mio collega e amico padovano Enrico Squizzato. Da quella conferenza a Napoli del 2019 abbiamo vissuto insieme gioie e dolori di questo dottorato. Un po' mi mancherà non mandare fibre in Via Marzolo 1, ma sono sicura che rimarremo compagni di spritz per molto tempo. Tante soddisfazioni condivise di cui andare fieri.

Infine, un grazie a tutti i miei amici che sono andati ed arrivati durante questo percorso. Grazie per la spensieratezza e il supporto che mi avete dato. In maniera non diretta, avete contribuito alla realizzazione di questo percorso. Mi sento di spendere un ringraziamento speciale a chi è con me da sempre, Sara, Carla, Vittoria, Elmasa e Fra. Ma anche chi come Andrea, Andrea, Mattia, Fabiana, Ottavia, Martina, Elena e Sergio sono entrati nella mia vita durante questo percorso e hanno migliorato il mio cammino.